The Combined Electrochemical and Microstructural Characterisation of the Electrochemical Reduction of Uranium Dioxide to Uranium Metal in Molten Lithium Chloride-Potassium Chloride Eutectic.

By

Leon Decordiva Brown

Thesis submitted for fulfilment of the degree of

Doctor of Philosophy

UCL

2015

Declaration

I, Leon Decordiva Brown, confirm that the work presented in this thesis is my own. Where information has been derived from other sources, I confirm that this has been indicated in the thesis.

Leon Decordiva Brown

Dedicated to Emeritus Professor Douglas Inman

Preface

Abstract

The electrochemical reduction of uranium (IV) oxide to metallic uranium has been studied in lithium chloride-potassium chloride eutectic at 450°C using electrochemical and advanced material characterisation techniques.

Electrochemical characterisation identified a single reduction peak occurring at -2.57V with respect to the $Ag|Ag^{+}$ reference electrode. Sweep voltammetry has identified that the electroreduction of uranium dioxide to metallic uranium occurs via a single, 4-electron transfer, process. The electrochemical reduction has also been observed to be dependent on the activity of O^{2-} ions: An increase in the bulk activity of the oxygen anion impeded the electroreduction process. This phenomena was thermodynamically predicted using Littlewood diagrams produced for the system.

In addition, *in situ* energy dispersive X-ray diffraction investigations were carried out on the I12 JEEP beamline at the Diamond Light Source which resulted in the direct observation of the formation of uranium metal when a uranium dioxide electrode was exposed to electroreduction potentials. No intermediate phases were observed which supports the electrochemical characterisation of this process occurring in a single step.

Moreover, microstructural characterisation has been performed on micro-bucket electrodes and metallic cavity electrodes. A coral-like structure was identified after reduction of uranium dioxide and has been attributed to the volume change associated with the reduction. Microstructural reconstructions were performed on four separate sub-volumes in the direction of propagation of the electroreduction process. The porosity was seen to decrease significantly from 16% to 4%. The pore connectivity was also observed to decrease from 93% to 18%. This drastic change in porosity and pore connectivity is reflected in the pore tortuosity which is seen to increase to infinity. This microstructural evaluation is concluded to impede the

diffusion of O^{2-} ions out of the electrode resulting in an increased probability of impediment of the electrochemical reduction process.

Acknowledgements

Firstly, I would like to acknowledge Dr. Paul Shearing and Dr. Dan Brett for their masterful supervision of my Ph.D. I have thoroughly enjoyed working under you both and the work of this thesis is testament to you both.

Secondly, I would like to thank my parents, Jenny and Junior, and my brothers, Ashley and Marcus, for their continued support throughout my academic studies. A notable mention is given to my sister-in-law, Marisa, and my nephew, Reece, for bringing joy and love to our family. A special "grazie" is dedicated to Alice for all of her continued love and understanding.

Thirdly, I would like to give a shout-out to all of my friends and colleagues in the Electrochemical Innovation Lab for their help both professionally and socially. Particular thanks go to Vidal, Rhodri, Dami, Donal, Bernhard, Erik and James - you guys are great. I would also like to expand my gratitude to Jason, Tom and Toby for their help and general laboratory support.

Lastly, I would like to say a few words to Emeritus Professor Douglas Inman who sadly passed away during this project. Unfortunately, I never had the chance to say goodbye to you and that is something that I will always regret. I have wanted to tell you, truly, how much I respected you and how fond of you I was. You were the perfect academic role model and you were an absolutely great friend. I have come to greatly miss our meetings in the Bromley South Starbucks and our Skype meetings (which often turned into football talk!). However, the thing I will miss the most is the enthusiasm you injected into me. Your love of science, of electrochemistry and of molten salts was truly something I was - and still am - in awe of. If I am able to become only a quarter of the man you were then I would be very happy with how my life had turned out. Thank you for all of your help. Rest in peace, my friend.

Contents

List of Tables

List of Figures

Nomenclature

η	Integer
λ	Wavelength of incident X-ray (m)
υ	Applied Voltage (V)
C_f	Final concentration of O_2 gas (ppm)
C_i	Initial concentration of O_2 gas (ppm)
C_p	Concentration of O_2 gas in purge gas (ppm)
Q_{CV}	Heat flux through the control volume (kW)
Q_{PORE}	Heat flux through the pore phase (kW)
t_p	Purging time (s)
ε	Porosity (-)
τ	Tortuosity (-)
ω	Frequency (Hz)
$\dot{\mathrm{Q}}$	Purge gas volumetric flow rate ($m^3 s^{-1}$)
ΔG	Gibbs free energy (J)
a^x	Activity of species x
C	Capacitance (F)
d	Spacing between planes of atomic lattice (m)
E	Cell potential (V)

E	Potential (V)
E^0	Standard cell potential (V)
F	Faraday's Constant (96485 C mol^{-1})
i	Current (A)
K(x)	Soluability product of x
L	Inductance (H)
m	Number of moles of O^{2-} (mol)
n	Number of moles of electrons (mol)
R	Universal gas constant (8.314 J mol^{-1} K^{-1})
r	Resistance (Ohms)
T	Temperature (K)
t	Time (s)
V	Vessel ullage volume (m^3)
Z	Impedance (Ohms)

List of Abbreviations

AC - Alternating Current

CT - Computed Tomography

CV - Cyclic Voltammogram

eV - Electron Volts

MCE - Metallic Cavity Electrode

MBE - Micro-bucket Electrode

DC - Direct Current

EDXD - Energy Dispersive X-ray Diffraction

EIS - Electrical Impedance Spectroscopy

FFC - Farthing Fray Chen Cambridge process

FIB - Focused Ion Beam

I.D - Internal Diameter

LKE - Lithium chloride-Potassium chloride Eutectic

LSV - Linear Sweep Voltammetry

MOX - Mixed OXide fuel

MSR - Molten Salts Reactor

O.D - Outer Diameter

Ox - Oxidated Species

ppm - Parts Per Million

PUREX - Plutonium URanium EXtraction process

RE - Reference Electrode

redox - REDuction-OXidation

Rd - Reduced Species

SEM - Scanning Electron Microscopy

TPB - Triple Phase Boundary

TPI - Three Phase Interline

X-ray CT - X-ray Computed Tomography

XRD - X-Ray Diffraction

YSZ - Yttria Stabilized Zirconia

Chapter I. Introduction

1 Introduction

This Ph.D thesis outlines the fundamental processes of the electrochemical reduction of uranium (IV) oxide to metallic uranium in the lithium chloride-potassium chloride eutectic. This work examines the system by using a range of electrochemical, chemical and structural experimentation techniques to deduce the phenomena that occurs during this process.

The motivation behind this work is to increase the fundamental understanding of the reprocessing of spent nuclear fuel using a *pyroelectrochemical* process. This work has been funded by the Engineering and Physical Sciences Research Council's REFINE Consortium. The drive behind this Ph.D thesis, as part of the REFINE Consortium, is to ascertain the fundamental process conditions in the electroreduction of UO_2 to U in the lithium chloride-potassium chloride eutectic (LKE) molten salt. However, it could be said that the motivation behind the desire to research a new, proliferation resistant, reprocessing strategy (and to take steps closer to closing the fuel cycle) is the increasing concerns of global warming at the time of writing. The world is moving into a new era of 'green fuel' with a particular emphasis on a reduction in CO_2 emissions. The UK, specifically, has set out a plan aiming to reduce its 1990 levels of CO_2 emissions by 2020, with the ultimate goal of reducing the level of emissions by 80% by 2050. To achieve these targets, the UK government's Department of Energy and Climate Change has published "The Carbon Plan" [1]. This document sets out the pathways to de-carbonise the UK whilst ensuring a sustainable energy security and minimising costs to consumers. The document highlights the fact that the power generation sector accounts for 27% of the total CO_2 emissions in the UK, which needs to be reduced to a level close to zero by 2050. The decrease in emissions from the power sector must be accounted for by an increase of renewable energy sources and from nuclear energy.

The document also highlights the fact that power generation from nuclear power stations is currently projected as "the cheapest form of low carbon energy production" and it is forecast that nuclear power will play a pivotal role in the UK reducing its CO_2 emissions. With differences in global political opinions on current and past generations of nuclear power stations, the future of nuclear power may balance on the innovation of future nuclear power stations being inherently safer and allowing "closure" of the nuclear fuel cycle with proliferation-resistant reprocessing technologies.

With this in mind, this thesis strives to scientifically uncover a host of fundamentals of the first processing stage in *pyroelectrochemical* processing; selective electrochemical reduction of actinide oxides. With a particular emphasis on uranium species, the work that outlines this study - both in terms of thermodynamics and scientific experimentation - is the elementary process conditions from the electrochemical pathway to the microstructural evolution of the electrode.

The proceeding sub-sections of this chapter aim to expose the reader to an introduction of the three main topics this thesis covers: nuclear energy in general; the reprocessing of spent fuel and the use of molten salts as electrochemical electrolytes.

1.1 Nuclear Energy

The world has benefited from nuclear power since Queen Elizabeth II opened the first full-scale nuclear power plant at Calder Hall in 1956 [2]. Ever since, the world has profited from the energy available from nuclear fission and it has been supplying approximately 6% of the world's primary energy needs [3]. The energy available from nuclear fission has significantly less CO_2 emissions compared to fossil fuels: A life cycle analysis shows that typical nuclear fission reactors can, on average, produce up to 95% less CO_2 emissions compared to the fossil fuel life cycle analysis [4]. Nuclear power generation has the ability to drastically help reduce carbon emissions.

Over time, the initial fissile material used as the fuel in nuclear reactors is dimin-

ished; some of the fuel undergoes fission, producing other fissile nuclei, whilst some is transmuted into minor actinides, transuranics and fission products [5]. Some of the fission products can alter the structure of the fuel and the gasses formed pressurise the fuel. Due to this, the fuel becomes uneconomical to further irradiate and thus it is removed from the reactor. This spent fuel is either disposed of directly (known as an open fuel cycle), is stored in interim storage facilities for future "disposal" (deferred fuel cycle) or undergoes reprocessing to extract the valuable fissile materials and to condition the minor actinide products into more suitable forms for disposal/storage (partially closed fuel cycle). This partially closed reprocessing route, which is described in more detail subsequently, removes the useful fissile material that can be burned up in thermal nuclear reactors. This allows one to re-use the recovered uranium fuel and possibly, in the form of mixed oxide (MOX) fuel, the recovered plutonium. However, in order to fully close the nuclear fuel cycle the minor actinides that are produced as a product of fission also need to be burned in an advanced fast nuclear power station.

Although no country has managed to fully close the nuclear fuel cycle to date, the reader is urged to consider how valuable reprocessing of spent nuclear fuel can be: Consider the fact that in 1993, 60 te of plutonium was produced from 430 nuclear reactors, giving rise to a possible 5000 PJ of energy available to be harnessed from recycled plutonium [6]. In comparison, some $3.5 \text{x} 10^6$ te. of coal would be required to produce the same amount of energy [7]. This astonishing comparison begs to highlight the fundamental advantages of nuclear energy compared to its high carbon alternatives. Further to this, a fully closed nuclear fuel cycle would allow these numbers to further increase as the burn up of minor actinides would also be included.

However, the reprocessing of nuclear fuel currently has a significant drawback; proliferation of nuclear material. It goes without saying that reprocessing of nuclear fuel was invested into heavily for this sole reason. Weapons grade uranium and

plutonium is achieved by nuclear fuel reprocessing, namely using the Plutonium - URanium EXraction (PUREX) process, although other liquid-liquid extraction (LLE) processes exist. Ensuring proliferation resistance of reprocessed nuclear fuel is vital in maintaining nuclear energy as a viable alternative to fossil fuel energy. Future reprocessing routes would need to ensure proliferation resistance in order to cement its potential place as a secure, long term, means of low carbon power generation.

1.2 Reprocessing

Although nuclear reprocessing does reduce the amount of high level waste for storage, it was plutonium production which was the initial driving force for the reprocessing of irradiated nuclear fuel. Weapons grade plutonium is able to be extracted in almost perfectly pure amounts using solvent extraction [8]. Traditionally, the technique which is best for nuclear reprocessing is the PUREX process which is based on liquid-liquid ion exchange extraction. There are, typically, 3 steps involved in the PUREX purification process: The first is extraction of U(VI) and Pu(IV), the second is U(VI) and Pu(IV) partitioning and the last is U(VI) stripping [9]. Tributylphosphate (TBP) in a solution of HNO_3 is used for the extraction process, whereas the second and third steps strip the TBP from the fissile material. The recovered uranium serves to re-enrich fuel and the recovered plutonium is diluted with other fertile material to produce Mixed Oxide (MOX) fuel.

A major disadvantage of the PUREX process, in terms of spent fuel reprocessing, is the increased risk of nuclear misuse. From Figure 1.1, one can see that a pure plutonium product stream is produced, increasing the risk of weapons proliferation.

Due to the fact that this reprocessing technology is well defined and understood, other LLE techniques are increasingly being researched into. As it is possible to extract uranium and plutonium it is also possible to recover minor actinides too. Other LLE processes, such as the Selective ActiNide EXtraction (SANEX) and

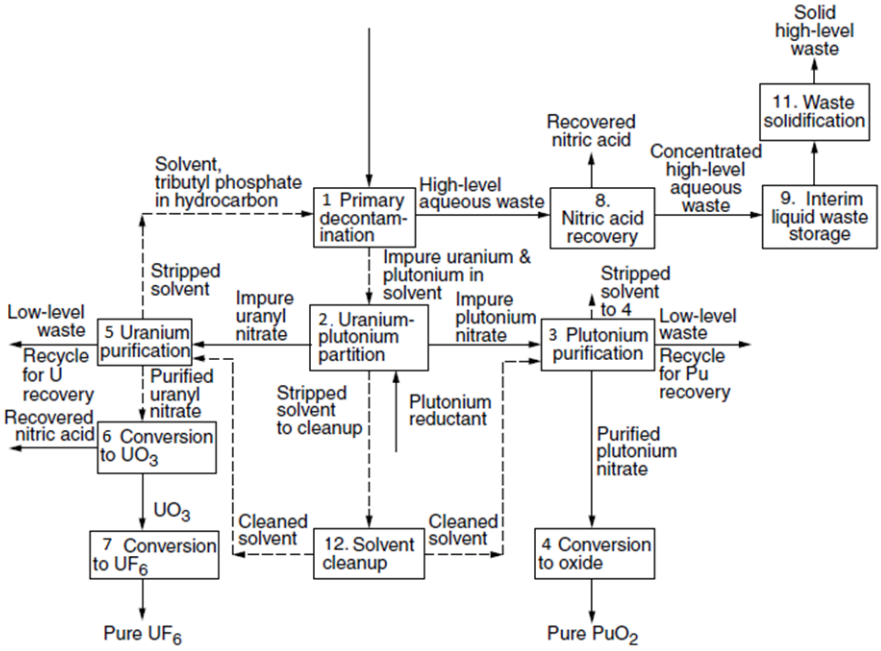

Fig. 1.1: Flow sheet of the PUREX Process. Image adapted and reprinted from Benedict *et al.*, Nuclear Chemical Engineering, 2nd edition, 1981, McGraw Hill. Reproduced with permission of McGraw-Hill Education.

the UNiversal EXtraction (UNEX) processes, which will extract different species, can be combined together in various schemes to recover all of the species required. Although, this does increase the complexity and, therefore, the cost.

More recently, nuclear reprocessing via a pyroprocessing route has been gaining more attention, particularly in parts of Asia and the USA [10-14]. Although the technology has not been established commercially, only proven on the pilot plant scale, there is a widespread understanding that this process could be more beneficial in preventing weapons proliferation as weapons grade material is not produced. Pyroprocessing operates using an electrochemical reaction scheme. A current is passed through spent fuel electrodes which are immersed in an electrolyte, usually a molten salt, in order to reduce the metal oxide to a pure metal. After which, the reduced species may be selectively plated onto electrodes immersed in the molten salt. This reaction pathway is able to produce both uranium and plutonium from

their oxides without creating separate plutonium process streams, therefore greatly reducing the risk of weapons proliferation. Moreover, this electrochemical system has an advantage of being incorporated into a type of "generation IV" reactor, providing *in-situ* reprocessing and potentially closing the nuclear fuel cycle. Although this Molten Salt Reactor (MSR) is only a generation IV concept, the benefits of using this system are great compared to today's technology.

The work presented in this thesis looks to provide knowledge of a novel re-processing route using electrochemical reduction techniques to spent nuclear fuel, as opposed to traditional solvent extraction routes. The electrochemical technique provides many advantages compared with these traditional solvent extraction processes, namely the potential to help close the nuclear fuel cycle. Future generation reactor systems will also look to provide *in-situ* re-processing of which this electrochemical route is feasible.

Nuclear power has a huge potential to drastically reduce carbon emissions. By incorporating a novel and proliferation resistant reprocessing technology, nuclear power may still ensure a future as a low carbon power production technology.

The electrochemical reduction of spent nuclear fuel is also a function of the microstructural characteristics of the fuel pellets. The reduction reactions require electrons and ions to be transported to the reaction site. The metal oxide phase is usually electrically insulating (although uranium dioxide becomes somewhat more electronically conductive above 400°C [15, 16]) and so electrons must be transported to the reaction site via a current collector. This requires good microstructural contact between the current collector and metal oxide phases. Also, for the ions to also be present at reaction sites, the sample must contain a wealth of pores that are well connected in order to provide good electrolyte penetration. The inherent microstructural characteristics of these pores will determine how efficiently the ions can diffuse to/from the reaction site. It is therefore important to characterise the process on the micro-scale. By understanding the microstructure of the electrode,

one can describe the electrochemistry on the micro-scale. This understanding can then be translated to optimise the bulk performance of the electrode.

Therefore, this investigation aims to unearth a host of phenomena associated with the electroreduction of uranium (IV) oxide to metallic uranium. By studying the electrochemical performance of the system and investigating the microstructural characteristics of the system, one targets an increased understanding of this reprocessing process. To conclude, the work described in this thesis provides an overview of a novel reprocessing route using electrochemical reduction techniques and examines the microstructural characterisation of the system.

The proceeding chapters of this thesis will explore the theory, experimentation and a selection of previous studies with respect to the electroreduction of uranium dioxide to uranium in molten salt media. Chapter II is comprised of a in-depth, high-level literature review of actinide materials in molten salt media. It also explores the microstructural characterisation of electrochemical devices. Chapters III and IV describe the scientific theory and experimental design that have provided the foundations for the hypotheses outlined within this thesis. They examine electrochemical and microstructural characterisation techniques and describe how they have been applied to experimentation. Chapters V-VIII provide theoretical and experimental results of the research question this thesis attempts to answer. A combination of experimental techniques and experimental set-ups described in Chapters III and IV are used to characterise the electroreduction process. Lastly, a conclusion of the thesis and topics of future work are discussed in Chapter IX.

Chapter II. Literature Review

2 Literature Review

Due to the nature of the investigations of this thesis, this chapter is broken down into two main topics. The first is a literature review of electrochemical processes of actinide species in molten salts. The review of these studies aim to provide the reader with a comprehensive overview of the electrochemical uses of molten salts both in and out of the nuclear industry. The second topic of this section is the tomography of electrochemical devices, not necessarily of molten salt based electrochemical cells. The aim of this subsection is to provide the reader with an overall introduction of how the microstructure of electrodes may effect the bulk performance of electrodes.

2.1 The FFC Cambridge Process

Although only lithium chloride-potassium chloride eutectic (LKE) is considered in the electrochemical studies of this thesis, a useful place to begin to consider the application of molten salts is the FFC Cambridge Process [17]. This process uses molten salt media to electrochemically produce titanium metal from titanium dioxide. The traditional (and more expensive) processes of producing titanium is known as the Kroll process. Developed by William Justin Kroll, the process involved a number of high temperature steps to convert TiO_2 to $TiCl_4$ and then reduction of $TiCl_4$ to Ti using liquid magnesium [18]. The FFC Cambridge process, however, uses an electrochemical cell to directly reduce the titanium dioxide.

During the FFC Cambridge Process, TiO_2 is made into an electrode inside an electrochemical cell. The electrolyte for this process is molten $CaCl_2$. By applying a cathodic potential, the metal is reduced to metallic titanium. The oxygen is transported to a graphite anode in the form of O^{2-} ions, where it is consumed to produce CO or CO_2. In 2000, Chen *et al.* reported that direct electrochemical re-

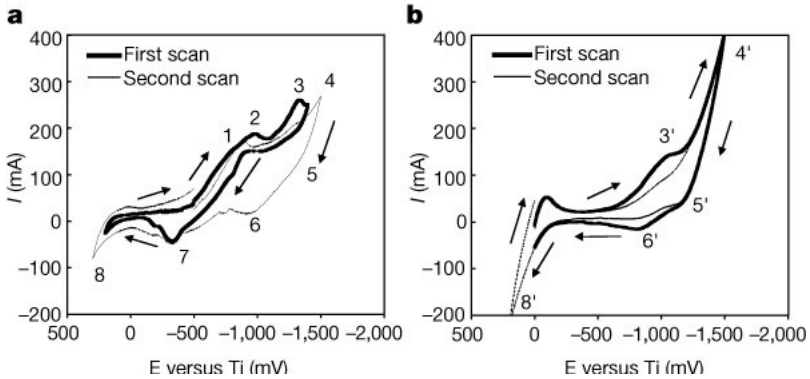

Fig. 2.1: Cyclic voltammograms of (a) titanium foils with an oxide coating and (b) the as received foil (no coating). Comparison of both shows an oxidation peak (7) and two reduction peaks (1 & 2) are absent on (b). This is indicative of a reduction (and re-oxidation) of the oxide coating. Reprinted by permission from Macmillan Publishers Ltd: Nature, Vol. 407, No. 6802, pp. 361, (2000), copyright 2000.

duction of titanium oxide to metallic titanium was possible using a molten calcium chloride salt [17]. A proposed intermediate for this reaction was that the oxygen reacts with the calcium in the $CaCl_2$ melt to form soluble CaO. However, an alternative, more favourable, mechanism was also suggested whereby titanium dioxide is reduced directly to titanium, with the oxide ionizing directly into the melt and being evolved at the anode. Thin film oxide scales were grown onto titanium foils and cyclic voltammetry (CV) was performed on these films and on pure titanium foils (for an introduction to cyclic voltammetry, the reader is referred to Section 3.1.2 of this thesis). The voltammograms clearly show peaks that can be attributed to the reduction of oxide scales as these peaks were missing on the cyclic voltammograms performed on metallic titanium foils, as shown in Figure 2.1. The results suggested that direct electroreduction was feasible as ionization of the oxygen in TiO_2 had occurred.

Micro-hardness test showed that oxygen had in fact moved from the oxide surface layer, into the neighbouring metal phase. Therefore, an electrochemical cell was set up with the oxide-scaled foils set as the cathode, a graphite rod the anode and

molten $CaCl_2$ as the electrolyte. The cell was held at temperatures between 850-960°C. The goal of this was to attempt the removal of the oxygen completely by using more negative potentials. Voltages of 2.8-3.2 V were applied and this resulted in an initial current of 1A to pass. The current gradually reduced to the background value of, approximately, 0.2 A. Analysis of the results suggested that the oxide scale had completely reduced to a porous metal layer.

Finally, 5-10mm diameter TiO_2 pellets made from pressed powder were made the cathode; via suspension on a kanthal cathodic current collector (or placed into a titanium, graphite or alumina crucible - which also acted as the current collector). Voltages of 3.0-3.2 V were applied, giving rise to a current density of approximately 10^4 A m^{-2}. This resulted in foam like titanium metal with a similar microstructure to that of titanium produced via the traditional Kroll process. This work thus proved that a simpler, electrochemical, method could be deployed to produce titanium compared to the Kroll process.

Further to this, Dring *et al.* proposed the electrochemical reduction mechanism by using voltammetry techniques on titanium dioxide films in molten calcium chloride [19]. CV was performed on these titanium dioxide films, resulting in five peaks, C0-C4, as shown in Figure 2.2. Chlorine formation from decomposition of calcium chloride melt occurred 600-700 mV positive of the reference electrode. A peak at *ca.* -1400 mV, C0, was attributed to calcium deposition from the electrolyte. The remaining peaks (C4-C1) within the potential window were attributed to the various electrochemical processes that occur during the electroreduction.

The phases formed at these peaks were characterised using SEM, X-ray energy dispersive spectroscopy and X-ray diffraction. The observed de-oxygenation of titanium dioxide, from peaks C0-C4, was:

$$TiO_2 \rightarrow Ti_3O_5 \rightarrow Ti_2O_5 \rightarrow TiO \rightarrow Ti[O] \tag{2.1}$$

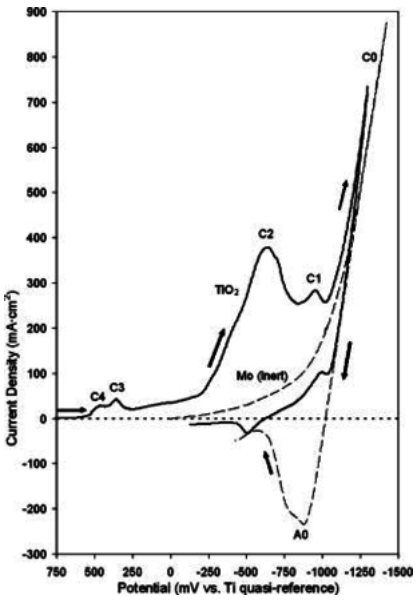

Fig. 2.2: Shows a cyclic voltammogram of a titanium dioxide film in molten calcium chloride. 5 peaks (C0-C5) can be observed. Reprinted with permission from J. Electrochem. Soc., 152, E104 (2005). Copyright 2005, The Electrochemical Society.

Where Ti[O] is solid solutions of oxygen in titanium metal. It was also observed that local increases in oxide concentrations, due to the removal of oxides, caused the formation of calcium titanates. This was due to the activities of the oxide ions, calcium ions and unreacted TiO_2 exceeding the solubility product for the titanates in calcium chloride.

This work was expanded further and, somewhat confirmed, by Schwandt via an investigation into the reduction pathway of TiO_2 to Ti by a partial reduction procedure [20]. Within this study, commercially available titanium oxide powder was sintered into cathode pellets, similar to what has been previously described [17]. The study was based on three phases of partial reduction. Firstly, a potential difference of 1.5 V was applied and maintained for a period of 8 hours. During the second phase, the potential difference was increased to 2.7 V and held for 24 hours and the last phase saw the potential difference increased further to 2.9 V. Samples were taken from the cell before each new phase was introduced and was prepared

Phase #	Reaction
1	$4TiO_2 + Ca^{2+} + 2e^- \rightarrow Ti_3O_5 + CaTiO_3$
	$3TiO_2 + Ca^{2+} + 2e^- \rightarrow Ti_2O_3 + CaTiO_3$
	$2TiO_2 + Ca^{2+} + 2e^- \rightarrow TiO + CaTiO_3$
2	$2CaTiO_3 + TiO \rightarrow CaTi_2O_4$
	$2CaTiO_3 + 2e^- \rightarrow 2TiO + Ca^{2+} + 2O^{2-}$
3	$CaTi_2O_4 + 2e^- \rightarrow 2TiO + Ca^{2+} + 2O^{2-}$

Tab. 2.1: Showing the proposed electrochemical reduction pathway in the FFC Cambridge process.

for X-ray diffraction (phase composition) and electron microscope (microstructure) characterisation. The results showed that the reduction process advances through a series of defined reaction steps. These reaction steps are tabulated in Table 2.1. After phase 3, it was understood that the TiO is reduced further to solid solutions of oxygen in titanium metal, $Ti[O]_\delta$ where δ denotes the oxygen content in the solid solution that is in equilibrium with TiO.

In 2010, Bhagat *et al.* reported *in situ* synchrotron diffraction of the electrochemical reduction pathway of TiO_2 [21]. In this study, Bhagat used synchrotron white beam X-rays to study and characterize the phases that form during the process. The advantage of producing an *in situ* diffraction pattern is that the cooling and washing required in the *ex situ* studies could result in crystallographic changes and the possible removal of water soluble species [21]. The experimental set-up was similar to the cells used by authors mentioned above. However, the reaction vessel was heated in a quartz glass vessel with slits in the furnace wall to allow the X-rays to enter and exit. The electrolyte was contained within a glassy carbon crucible which also acted as the anode. The cathode was formed of sintered TiO_2 pellets attached to a titanium current collector. The white X-ray beam (50 μm x100 μm) was incident on to the pellet with a 5° scattering angle was defined by the beam slits. This assembly was mounted on a translation stage which allowed nine locations at different heights in the pellet to be studied. The $CaCl_2$ salt was pretreated, heated and thermally equilibrated before the precursor was lowered and polarized.

The study showed that TiO_2 is immediately reduced to Ti_4O_7 and calcium titanate, $CaTiO_3$, is also produced. The formation of $CaTiO_3$ was attributed to the release of oxygen ions into the electrolyte, formed from the reduction of TiO_2. Intriguingly, Bhagat was unable to detect the formation of Ti_3O_5, conflicting with results produced from Dring, Schwandt and Alexander [19- 22]. The theory behind this is that the homogeneity range for Ti_3O_5 is too small and would require longer polarization in the specific conditions to form. A further significant point is that the $CaTiO_3$ that is formed is most likely to be sub-stoichiometric. The *in-situ* XRD analysis showed slight shifts in the main peaks of $CaTiO_3$, resulting in lower d-spacing values. This suggests that the crystal structure of $CaTiO_3$ is altered as oxygen ions are removed from the molecules.

In addition, this investigation was also able to confirm that the production of $CaTi_2O_4$ was in fact created via a comproportionation reaction as described by Alexander [22], rather than the electrochemical pathway as described by Schwandt [20]. Furthermore, during the latter stages of the reduction, CaO was detected throughout the pellet. This was correlated to the reduction of $CaTi_2O_4$ resulting in rapid evolution of oxide ions. However, the porosity of the pellet is reduced during reduction (due to the sintering of Ti and formation of titanates) and causes the pellet to become saturated with oxide ions, causing CaO to form.

The FFC Cambridge Process is an electrochemical reduction of titanium dioxide in a calcium chloride melt at 900°C. By polarizing the TiO_2 in a $CaCl_2$ electrolyte, it is possible to produce titanium metal with a similar microstructure to that produced by the Kroll process. From the reports reviewed in this section, it is clear that the reduction of titanium dioxide to titanium is not a simple 4-electron step process. The complexity of the electrochemical reduction has been studied extensively to better understand the reduction pathway. From this work, it is conceived that reduction process in molten salt media may include chemical reactions as well as electrochemical.

2.2 Review of Actinide - Molten Salt Electrochemistry

Molten salts are ionic compounds which are, generally, solid at standard temperature and pressure (25^{o}C, 1 bar). They may be used in their liquid, non-aqueous, state by elevating the temperature beyond their melting point, giving rise to a host of advantages and making them applicable to many different applications: from use as solvents to electrochemical electrolytes [23]. In terms of their use as a solvent, they may generally be classed as ionic solvents due to their differing chemical properties when compared to other aqueous or non-aqueous solvents. In addition, due to the increased temperature in which molten salt solvents operate, this usually allows reaction kinetics to be much more rapid; following the laws of chemical equilibrium. Because molten salts consist of anions and cations, they are ideally suited to be electrolytes in electrochemical processes. Alkali and alkaline earth metal salts possess very negative Gibbs free energies of formation; hence, they possess very negative cation deposition voltages and large electrochemical windows compared to aqueous systems. Moreover, molten salts have the capacity to dissolve materials to very high concentrations [24]. This high solubility results in high limiting current densities and, hence, high productivities in electrochemical processes. Another advantage of molten salts is that chemical reactions between the metal ions and the solvent are generally absent. However, due to the multiplicity of metal oxidation states, interactions between the metal ions and the solvent must be carefully monitored.

A mixture of two or more salts containing the same anion may form a eutectic system. This is a mixture of compounds that solidifies at a lower temperature than any other percentage composition made up of the same salts. A eutectic system may be easily identified using a phase diagram of the chemical mixture; the eutectic point being a well-defined point of lowest temperature of solidification of the diagram. Lithium chloride and potassium chloride form a eutectic at 59% mol. of lithium chloride. The phase diagram for the lithium chloride-potassium chloride system

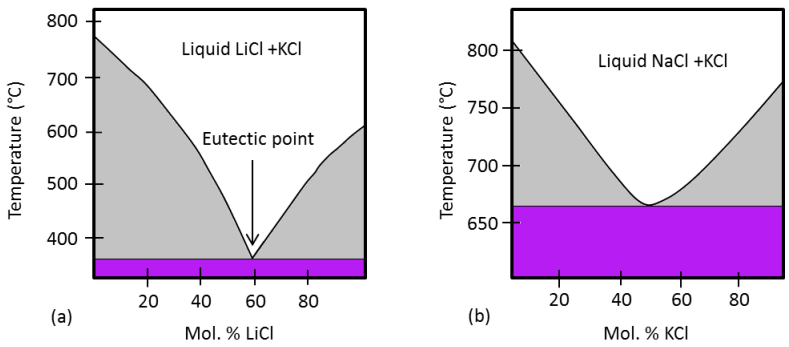

Fig. 2.3: Phase diagrams for (a) The LiCl-KCl system and (b) The NaCl-KCl system. The purple shaded areas denote the solid state of the system. The eutectic point is clearly shown in (a) - a eutectic is the point is the lowest, single, point at which the two compounds have the lowest melting point. This is compared to (b) where there is no single point of lowest melting point. Instead there are multiple values of molar ratio of NaCl and KCl in which the lowest melting point is achieved.

is shown in Figure 2.3 with comparison to that of the potassium chloride-sodium chloride system which does not form a eutectic.

Figure 2.3 shows the phase diagrams for a mixture of lithium chloride and potassium chloride (a) and for a mixture of sodium chloride and potassium chloride (b). The plots are molar percentage of one of the species *versus (vs.)* the temperature of the mixture of chlorides. The purple regions in Figure 2.3 depict the solid states of the mixture of salts. Above this purple region the salt mixture exists completely as liquid. From the phase diagram for the LiCl-KCl system, it is noted that there is a eutectic point. This is defined as the lowest possible melting point of any mixing ratio of the species involved. This is comparable to the phase diagram of NaCl-KCl which does not form a eutectic. This is because there are multiple mixing ratios of NaCl and KCl in which the lowest melting point exists, albeit the range is small. As one can see, the eutectic point for the lithium chloride-potassium chloride system is at a molar ratio of 0.59:0.41 (LiCl:KCl).

For the work presented in this thesis, the molten salt adopted for all experimentation is lithium chloride-potassium chloride eutectic (LKE). This particular

eutectic may be regarded as a "low temperature" molten salt due to its relatively low melting point of 352°C, compared to other salts (658°C and 772°C for NaCl-KCl and $CaCl_2$ respectively, for example) . LKE is an alkali chloride salt and, therefore, possesses a relatively large potential window. Lithium deposition occurs at -3.57 V versus the standard chlorine electrode - which allows for its use as an electrolyte in various, low temperature, electrochemical separation processes, including the electrochemical study of this work.

2.2.1 Actinide and Lanthanide Stabilities in Molten Salts

The next stages of this literature review aim to provide a comprehensive review of nuclear materials in molten salts. The most useful place to start is by reviewing the stabilities of elements/compounds of spent nuclear fuel in molten salt environments.

By considering molten salts as an ionic solvent, compounds may exist, or even co-exist, within a molten salt and that an element (or compound) may also exists in multiple oxidation states. Halide/nitrate/silicate based compounds, for example, would integrate into the ionic structure of the molten salt. As with any solvent, whether it be organic or ionic, many compounds are also insoluble in molten salts. Although the miscibility of different solutes are not described in detail in this thesis, this leads to a variation in a specie's ionic stability within molten salts, leading to the possibility of molten salt liquid-liquid extraction processes. Dissolution of a compound into a molten salt could be a complete dissociation into its own respective anion and cation but, and more generally, would see the metallic cation form complexes with the anions of the solvent. For example, the solvated form of zirconium (II) in a chloride salt would be $ZrCl_4^{2-}$, although it is common to drop the compound's ions that are associated with the solute, *i.e.* Zr^{2+}[25]. Once dissolved into the ionic structure of a molten salt, the species would normally be exposed to ion coordination interactions, as expected, but also to coulombic interactions as well.

One of the most important features of the ionic solvent characteristics of molten salts is the oxygen anion, O^{2-}. This anion is able to exist freely in a molten salt environment and will alter the "oxoacidity" of the melt based on the activity of oxygen anions in the melt [26, 27]. This concept is directly related to the acidity of aqueous solvents, which is dependent on the activity of the hydronium ion, denoted as a_{H^+}: the negative logarithm of the activity of H^+ions is referred to as pH in aqueous systems, whilst in non-aqueous molten salt media, this principle may be applied to the negative logarithm of the activity of O^{2-}, the pO^{2-}. This specific anion is able to coulombically interact with species dissolved in a molten salt, leading to oxocaid-oxobase couples. Adopting the general conventions, an oxoacid is defined as an electron pair acceptor and an oxobase is defined as a complex containing the O^{2-}ion, which acts as an electron pair donor (although the transfer of electrons is not restricted to pairs) [25]. This leads to one being able to describe the oxoacid-oxobase system using Equation 2.2:

$$oxobase \rightarrow oxoacid + O^{2-} \tag{2.2}$$

Depending on the activity of oxygen anions contained within a molten salt system, this oxobase-oxoacid couple has the ability to react with dissolved compounds and is a very important phenomena to control. Moreover, this couple may also coulombically interact with the system in an electrolytic cell. That is, if a molten salt based solute is utilized as an electrolyte, the oxoacid-oxobase couple may take the form:

$$oxobase + ne^- \rightarrow oxobase' + oxoacid + mO^{2-} \tag{2.3}$$

Where the term "oxobase´" is a different, lower oxidation state, oxobase to that of the reactant. However, and more generally, the coulombic interactions of the O^{2-} ion on redox properties of electrochemical cells would take the form:

$$Ox + ne^- \rightarrow Rd + mO^{2-} \tag{2.4}$$

Where the redox potential of the system is given by the Nernst equation:

$$E = E^0 + \frac{RT}{nF} ln \left(\frac{a(Ox)}{a(Rd)} \right) - m \frac{RT}{nF} ln \left(a(O^{2-}) \right) \tag{2.5}$$

Therefore, it is apparent that one may diagrammatically represent the species contained within a molten salt in terms of the redox potential and the $p\mathrm{O}^{2-}$ of the system, similar to that of well know Pourbaix diagrams for aqueous media; a plot of potential *vs.* pH. These potential-$p\mathrm{O}^{2-}$ diagrams are referred to within this thesis as Littlewood diagrams, after Roy Littlewood who first described an in-depth diagrammatic representation in 1962 [28]. More information on the construction and characteristics of these diagrams is given in Chapter 5. The proceeding sub-chapters will study the various radioactive species that have been identified in molten salt media with Littlewood diagrams underpinning these studies.

2.2.1.1 Uranium Species in Molten Salts

In 1961 Molina *et al.* published work which provided an insight into the uranium species that would be stable in the LKE melt. The Littlewood diagram presented within predicted that 4 phases would be present in LKE – UO_3, UO_2, $UO_2{}^{2+}$ and U^{4+} species, with the first two of those species being insoluble in LKE [29]. Interestingly, the paper described three oxidising agents that could be used to form $UO_2{}^{2+}$ species within the melt via a oxoacid-oxobase reaction; reactions with Cu^{2+}, $S_2O_8{}^{2-}$and via bubbling Cl_2 gas through the melt. The diagram depicted domains of stability for the 4 species and the redox conditions required to change from one region to another. However, uranium (V) species were observed in LKE in 1963 by Adams *et al.* [30]. The pentavalent state of uranium, in aqueous systems, is well known to rapidly disproportionate into uranium (IV) and uranium (VI) species,

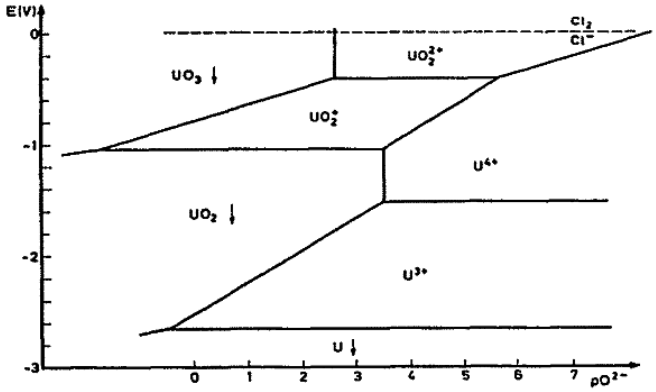

Fig. 2.4: A Littlewood (or predominance) diagram showing the proposed regions of stability of uranium species in LKE. Reprinted with permission from Elsevier: Analytica Chimica Acta, 65 (1973) 245-247.

such as the thermal disproportionation of UCl_5 [31]:

$$2UCl_5 \rightarrow UCl_6 + UCl_4 \tag{2.6}$$

On the other hand, Adams *et al.* were able to show that pentavalent uranium was stable in inert atmospheres or *in vacuo*. This was deduced from absorption spectra believed to be a result of the equilibrium:

$$UO_2Cl_2 \rightarrow UO_2Cl + \frac{1}{2}Cl \tag{2.7}$$

However, the authors were unsuccessful in their attempts to produce the known pentavalent species, UCl_5 and $UOCl_3$; the former being too volatile above the melting point of the molten salt and the latter being unstable. In addition, it was remarked that the UO_2^+ ion exists within LKE in the equilibrium:

$$UO_2^{2+} + UO_2 \rightarrow 2UO_2^+ \tag{2.8}$$

This finding was also reported by Komorov *et al.* [32].

This observation of UO_2Cl species in molten LKE led to a revised Littlewood

diagram in LKE in 1973 [33]. This diagram, reproduced in Figure 2.4, included the species predicted previously with the addition of the UO_2^+ and U^{3+} species; this study used data from the studies of Molina *et al.* and Ishno *et al.* [34] and was presented on the same mole fraction scale and so easy comparisons may be drawn from each of the diagrams. The stability of the UO_2^+ ion within LKE was debated: many studies showed its stability and many showed its instability in the fused salt. Uchida *et al.* published two works in the 1980s with evidence showing that this species was unstable in fused LKE [35, 36]. It was noted that the UO_2^+ ion would exist as an intermediate during the two step, two electron, electrochemical reaction

$$UO_2^{2+} + e^- = UO_2^+ \tag{2.9}$$

$$UO_2^+ + e^- = UO_2 \tag{2.10}$$

The first study utilized the polarography technique to deduce the half-wave potential for the electrochemical couple of Equation 2.10. It was found that $E_{1/2}^{Eq.2.10}$ was equal to -0.487 ± 0.005 V *vs.* 1M Pt(II)|Pt. This study also highlighted that the redox potential for uranyl reduction (Equation 2.11) had been well studied and all values reported are -0.285 V, -0.262 V and -0.271 V [37-38] respectively.

$$UO_2^{2+} + 2e^- = UO_2 \tag{2.11}$$

Therefore, the reduction from UO_2^{2+} to UO_2 (Equation 2.11) is seen to occur before that of UO_2^+ to UO_2 (Equation 2.10). Moreover, it is noted that the UO_2^{2+} species acts as an electron pair acceptor. With the addition of O^{2-} ions, this species undergoes a oxobase-oxoacid reaction, forming insoluble UO_3 in the melt. Therefore, Uchida *et al.* proposed a new Littlewood diagram in 1981 showing no thermodynamically stable region for UO_2^+ ions with the discrepancy being attributed to the

different standard potential value deduced by both authors [35].

The debate continued in 1986 when Martinot *et al.* published yet a new diagram showing the inherent stability of UO_2^+ ions in LKE [39]. Martinot *et al.* utilized cyclic voltammetry and differential pulse polarography to determine that the $UO_2^{2+}|U$ couple did in fact follow the two step electrochemical reaction of Equations 2.9 and 2.10 and, in fact, produced standard potentials for the $UO_2^{2+}|UO_2^+$ couple to be -0.84 V versus the $Cl_2|2Cl^-$ reference; in broad agreement with that deduced by Uchida *et al.* By using these values of standard potential, the author produced a Littlewood diagram with a thermodynamic region of stability for UO_2^+, although it was more narrow than that predicted previously [33]. Martinot *et al.* commented on the fact that the region of stability was evinced and Uchida *et al.* did not take into consideration the UO_2^+ species and seemed to ignore the spectroscopic evidence of its stability.

2.2.1.2 Plutonium Species in Molten Salts

Similar studies to those for the uranium systems in the previous section have been implemented for plutonium species in LKE at 500°C. Martinot *et al.* provided the first depiction of plutonium species in LKE at 400°C in 1973 [40]. The diagram showed the stability of four Pu species: PuO_2; Pu(IV); Pu(III) and metallic Pu which was again based on determination of solubility products coupled with thermodynamic data to deduce regions of stability. Landresse *et al.* predicted the stability of Pu(III), Pu(IV), Pu(V) and Pu(VI) species within the melt. However, the diagram presented showed the regions of stability of Pu^{4+}, PuO_2^+ and PuO_2^{2+} above the anodic melt deposition potential of the melt [41]. The author concluded that these phases would only be stable in an atmosphere of O_2-Cl_2. The author describes these phases as stable which cannot be true if they are only stable as gas outside of the potential window of the melt; that is, the author attributes the stability of these phases as the salt is being anodically decomposed. Moreover,

the author seemed not to comment on the corresponding cathodic half-cell reaction that would occur during anodic decomposition. This phenomenon was recognised by Martinot *et al.* who, in due course, published a new diagram in 1986 showing only the regions of stability within the potential window of the melt [40]. The most recent publication of this system is that of Caravaca *et al.* in 2008 [42]. Although the author did not acknowledge the Littlewood diagrams previously published. The diagram presented here differs from the published diagrams mentioned above and shows the stability of phases: PuO_2; Pu_2O_3; $PuCl_3$ and Pu. Differences between these diagrams, specifically the addition of the Pu_2O_3 phase, are not commented upon by the author.

2.2.1.3 Miscellaneous Species in Molten Salts

Littlewood diagrams for various lanthanides and actinides in molten LKE have also been published. Some, if not all, of these species would be present in spent nuclear fuel and, thus, assessing their stability in LKE is significant. Perhaps the most significant conclusion to be drawn from these diagrams is the perceived difficulty to separate them selectively from the bulk material in spent nuclear fuel (U and Pu species). Littlewood diagrams for La, Nd, Gd, Cm, Th and Pa all show similar reduction potentials for the formation of metallic species from their respective oxides [30, 33, 35, 39-43]. This results in the predicted difficulty of selectively separating these elements via a direct electrochemical reduction pathway. However, as thermodynamic data and experimental techniques have been updated these diagrams may be out of date. Moreover, due to the effect of the oxide ion concentration in the melt playing a role in the electroreduction potentials, it may be apparent to alter the process conditions to provide a more favourable route for the selective electroreduction for uranium dioxide and plutonium dioxide.

Littlewood diagrams are a useful tool for thermodynamically predicting stable species within a molten salt. They allow visualisation of which species are stable

and under which conditions those species will exists or co-exist. Moreover, the diagrams are able to depict the necessary conditions to produce a particular species in the molten salt from another. Many studies have been published which show the stabilities (and instabilities) of uranium species in molten LKE. Although there are some inconsistencies, particularly surrounding the stability of UO_2^+species. All of the previous work highlights the inherent stability of many species in the melt. Moreover, one can conclude that uranium (IV) and uranium (VI) oxide are both insoluble and precipitate out of the melt upon their formation. This gives rise to the ability of one to recover uranium from spent nuclear fuel as a solid deposit at a cathode and is reviewed more extensively in Section 2.2.3. The stability of Pu species in LKE are, again, uncertain. All of the previously published diagrams are in agreement with stability of Pu(III), Pu(IV) species but disagree on the other species mentioned above. Moreover, it is noted that oxobase-oxoacid reactions may play an important role in deducing which species exist within a molten salt. The pO^{2-} value should not be overlooked when attempting to control the conditions of a molten salt system.

2.2.2 Dissolution into Molten Salts

Many of the studies highlighted in Section 2.2.1 produced species in the molten salt via introducing a chloride of that species into the salt mixture itself. The other method of introducing a particular species into a molten salt is via anodic dissolution.

The dissolution of various nuclear materials in LKE has been studied and the literature contains information regarding the solubilities of various nuclear based compounds in this salt. Dissolution of these materials within a molten salt allows one to contain appreciable quantities of nuclear elements in solution within the salt. This can lead to various separation processes which will be expanded upon in forthcoming sections. The solubility product describes how the solid phase of the

compound of the element in contact with a molten salt solvent is in equilibrium with its dissociated ions. The solubility product (K) is defined as (*e.g.*):

$$K_{UO_2} = a_{U^{2+}} \left(a_{O^{2-}}\right)^2 \tag{2.12}$$

As described in the previous subsection, Littlewood diagrams are able to predict regions of stable phases within the melt. Solubility products have been used to construct these diagrams. Dissolution of species into the molten salt (or precipitation titration) allow solubility products to be calculated and, thus, $p\mathrm{O}^{2-}$ values for phase formation to be deduced.

2.2.2.1 Anodic dissolution of uranium mononitride

In an electrochemical cell, one is able to introduce elements into the melt via anodic dissolution. Selectively recovering the metallic form onto the cathode in these circumstances is known as electrorefining and is expanded upon in a latter subsection (Section 2.2.5). It is possible to anodically dissolve uranium into molten LKE as U^{3+} ions from uranium mononitride (UN) [44]. By cathodically polarising a graphite rod dipped into UN powder (at -2.4 V versus an Ag|AgCl reference electrode and molybdenum counter electrode), metallic uranium is deposited onto the graphite electrode. This deposition leads to a UC alloy with a surface layer of metallic U. It is then possible to anodically polarize this to dissolve a quantity of uranium into the melt. This occurs at -0.55 V and the dissolution of UC alloys at a potential of approximately -0.7 V. The threshold of dissolution of UN into the melt was observed to occur at -0.66 V (all of the electrode potentials reported here are with respect to the Ag|AgCl reference electrode). Above this electrode potential, UN is unstable and decomposes to U^{3+} + N_2 due to the reaction:

$$UN + 3\{AgCl\} = UCl_3 + \frac{1}{2}N_2 + 3Ag \tag{2.13}$$

Where the brackets denote components dissolved in the eutectic.

2.2.2.2 Anodic Dissolution of uranium and uranium dioxide

Work done by the Argonne National Laboratory concerned uranium dissolution into LKE containing 10% by weight of UCl_3 [45]. The aim of the study was to ascertain the anodic processes with the goal of maximising uranium dissolution from the zirconium metal cladding hulls and to minimise zirconium dissolution. The author was able to ascertain that uranium dissolves in the melt via electrochemical dissolution. The average dissolutions of 22 batches were analysed and gave, on average, uranium dissolution of 96% wt. and retention of 86% wt. of the zirconium cladding. The electrode potential for uranium dissolution in this work was not reported.

Dissolution of uranium into LKE is also feasible by directly anodizing metallic uranium electrodes [46]. By anodizing this electrode at low current densities ($<$50 mA cm^{-2}) one is able to form U^{3+} species via a single, 3 electron, step. The electrochemical reaction is thus:

$$U \rightarrow U(III) + 3e^{-} \tag{2.14}$$

This coulometric titration method has been applied in other studies *e.g.* Hill *et al.* [37]. Pure, out-gassed, rods of uranium were anodically polarized with a current density of approximately 10 mA cm^{-2}. These authors reported 100% current efficiency for this electrochemical reaction. Moreover, it is possible to produce U(IV) species within the melt by reacting U(III) with coulometrically generated Pt(II) from Pt foil anodes:

$$2U(III) + Pt(II) = 2U(IV) + Pt \tag{2.15}$$

The authors also described the direct anodic dissolution of uranium dioxide into the

melt. This was done by stripping UO_2 anodically. The dissolution was reported to occur at approximately -0.285 V with respect to a Pt(II)-Pt reference electrode. This value is reported to be influenced by oxide impurities within the melt which agrees with Littlewood diagram predictions.

2.2.2.3 Plutonium dissolution

Anodic and direct dissolution techniques have not been extensively reported in the literature. However it is reported that the dissolution of PuO_2 into LKE is feasible via a direct dissolution technique, that is [47]:

$$PuO_2 + Cl_2 \leftrightarrow PuO_2Cl_2 \tag{2.16}$$

It has also been reported that plutonium dissolution into the melt can be achieved via the anodic titration of a $PuPt_3$ precursor. Detailed information of this process is not presented [48].

The anodic dissolution of plutonium nitride is also possible. This is similar to that of uranium nitride reported earlier. It is possible to produce a quantity of plutonium(III) in the melt by polarising PuN anodically in a LKE melt containing small quantities of $PuCl_3$ [49]. The anodic titration equilibrium potential is -0.88V versus the silver chloride reference electrode and was attributed, by the author, to the reaction:

$$PuN + 3Ag^+ = Pu^{3+} + \frac{1}{2}N_2 + 3Ag \tag{2.17}$$

Moreover anodic titration of Pu into LKE is feasible and occurs in a single, 3 electron, step via the electrochemical half-cell reaction [50]:

$$Pu = Pu^{3+} + 3e^- \tag{2.18}$$

Cyclic voltammetry has been used to confirm this reaction. However reaction conditions and requirements are not stated in the literature. From an electrochemical point of view, the method and techniques required for anodic titration/dissolution into the melt should broadly follow those specified for uranium dissolution.

Dissolution of uranium species into LKE has been extensively researched and published in literature. This has not been done for Pu. However, the dissolution of Pu species (*i.e.* anodic polarization) would be possible, albeit at different electrode potentials. The Gibbs free energy change for the formation of U(III) species in the melt is similar to that for Pu(III) species. The polarization potentials predicted from the Nernst equation are slightly more negative to that for uranium. In practice the dissolution potentials of uranium (-0.2V *vs.* Pt(II)-Pt(0)) and plutonium (-0.88V *vs.* Ag|AgCl) are very different. On this basis one could expect that the two materials would be able to be selectively dissolved into the melt. Therefore separation of a mixture of these two elements would be possible via a "first in last out" electrorefining technique. In addition, the dissolution of species into the melt depends strongly on the solubility in the melt which is a function of operating conditions such as pressure and temperature of the salt. Moreover, equilibria between the melts and the cell atmospheres may be manipulated favourably. Dissolution also depends strongly on the complexity of the system.

2.2.3 Electrodeposition using Molten Salts

As mentioned in Section 2.2.1, some species are insoluble within the molten salt. This gives rise to the ability to remove these species via an electrodeposition technique. By electroplating an insoluble species onto an electrode, recovery of that species may be achieved easily. The deposition of nuclear materials via electrochemical pathways has been extensively researched and data are readily available [46-53]. The electrodeposition of radioactive species, in particular uranium species, are known due to the electrorefining process which is described in more detail in

Section 2.2.5 of this thesis. However, although these studies are in broad agreement with each other, one can conclude that because these results depend on various cell designs, activities and electrodeposition techniques, there may be some discrepancies.

2.2.3.1 Electrodeposition of uranium

The first report of metallic uranium formulation via electrolysis of a molten salt solution was presented by Driggs and Lilliendahl in the 1930s [54]. Here, KUF_5 and UCl_4 were added to a NaCl-KCl melt at 775°C. A voltage of 5 V was applied between a molybdenum cathode and the graphite anode, with a current density of 1500 A m^{-2}. Uranium metal began to appear upon the cathode in what was described as a "tree-like" deposit, thought to be dendritic. This occurred as soon as the uranium source was added to the melt. It was also noted that changing the current density to values as high as 3000 A dm^{-2} had no effect on the appearance and particle size of the deposits.

Work carried out by Inman *et al.* also observed dendritic deposits of uranium on tungsten/molybdenum cathodes [46]. The study was based on the electrochemistry of uranium and uranium trichloride in molten LKE and it was deduced that the reduction of UCl_3 transpired in a single, 3-electron step from the U^{3+} species. It was also reported that the dendritic deposits were more profound with a lower current density. When the current density was increased, it was observed that the deposits were compact powders overlaid with the dendritic deposits. This contrasts with the observations by Driggs and Lilliendahl where the current density had no effect on particle size. Inman *et al.* attributed the powdery deposit to a homogeneous liquid-phase reduction of the uranium trichloride by lithium at the electrode surface.

By using a tungsten working electrode, it was found that the deposition of uranium from uranium (III) occurs at a potential difference of -2.541 V at 500°C in LKE with respect to a standard chlorine electrode . This value is in contrast with the

theoretical prediction of -2.744 V and to that in the Littlewood diagram presented by Landresse [33], although this could be due to the experimental conditions used. The author also presented results showing that the addition of oxide ions caused the uranium potentials to change due to the fact that uranium oxide/ uranium oxychloride species were formed in the melt, which again agrees with Littlewood diagram predictions.

To evince the disparity of electrodeposition potentials in the literature it is worth noting a similar experiment conducted by Sakamura *et al* [52]. They reported that the redox potential of the U(III)/U(0) couple is -2.83 V with respect to a chlorine electrode. This discrepancy is due to the very low activities used in this work; concentrations used were in the region of X = 0.03-3x10^{-5}. Other redox potentials are presented as -2.45 V [49], -2.6 V [53] and -3.099 V [55] all with respect to the chlorine electrode.

More recently a study was conducted in order to provide more details about this process in the open literature [56]. A solid iron cathode was employed, rather than a steel one, as reported earlier. Dendritic deposits were observed, regardless of the current density. They were more prominent on the side adjacent to the anode and tended to break off. This agrees with observations made by Inman *et al.* [46]. Perhaps the most important conclusion that can be drawn from this report are the activity coefficients of U and Pu in liquid cadmium. The activity coefficient for Pu is 1.4x10^{-4} whilst that of U is 75. In practice the reduction potentials of both species are very close and so simultaneous deposition of both species may occur. It should also be noted that the rotation of the solid cathode facilitates more uniform deposits. It is apparent that fast rotational speeds, say 20 rpm, lead to non-adherent uranium but rotational speeds of 10 rpm lead to more uniform deposits and high collection efficiencies, although the deposits are still observed to be dendritic.

2.2.3.2 Electrodeposition of plutonium

Plutonium(III) in LKE can be prepared by anodic dissolution. It is then possible to electrodeposit metallic plutonium onto a working electrode if the reduction potential is -1.73 V with respect to the silver chloride reference electrode [57]. It is observed that the current increases as the plutonium is deposited due to the increased surface area caused by deposition. (The current density is related to electrode potential). The deposits are a mixture of Pu metal and LKE salt. It is not certain whether this is occluded melt or is just due to surface adhesion of the salt when the electrodes are removed. This redox potential is similar to that observed by Serp *et al.* who reported the potential to be -1.76V relative to the silver chloride reference electrode [58]. The redox potential is also in agreement with a study by Roy *et. al.* [59].

The electrodeposition of nuclear metals onto electrodes has been highlighted within this section. Perhaps the most striking conclusion one can draw from this review is the discrepancy between deposition potentials. Although the authors' studies all reveal broad agreement, the deposition potentials are significantly different. Of course, due to the Nernstian behaviour of electrochemical deposition, the redox potential of the $U|U^{3+}$ couple depends strongly on thermodynamics and reaction conditions, such as the pO^{2-}. Thus, comparing redox potentials between different authors is difficult. On the other hand, it is important to note that many of the deposits formed on solid cathodes were dendritic. This phenomenon is an important complicating characteristic of the system. If the dendritic growth of uranium on a solid cathode were to become too large then this could either break off and fall into the bulk melt, or could in fact cause short circuiting of the system. Although a study has been conducted in which the cathode was rotated at low RPM –which helps to inhibit dendritic growth – this introduces unnecessary complications into the reaction design. However, there may be ways to facilitate the uniform growth of uranium onto solid cathodes via an electrochemical pulse technique. That is,

instead of applying a constant potential across the electrodes, one could pulse this potential in order to achieve uniform deposits [60].

2.2.4 Reduction of Uranium Oxides in Molten Salts

As shown with the FFC Cambridge process in Section 2.1, molten salts may provide advantageous process conditions for the electroreduction of titanium dioxide to titanium metal. This practice may also be adopted within the nuclear industry in terms of reducing the actinides to their metallic form. Typically, compounds of the actinides possess very negative Gibbs free energies of formation and hence they possess very negative electrochemical reduction potentials, as predicted by the Nernst equation. However, because the alkaline earth - halide molten salts also possess very negative Gibbs free energies of formation, the salt's cation deposition potential is also very negative. This may prove to be very advantageous as it could allow for the electrochemical reduction of actinide oxides to their metallic form in the molten salts, which would not be feasible in aqueous systems.

2.2.4.1 Reduction in LiCl containing Li_2O

Investigations into the reduction of uranium oxides to metallic uranium have been reported in the LiCl molten containing 1 mol % percentage of Li_2O [61-64]. The Li_2O added to the LiCl serves as a reduction agent; the reduction of uranium oxide is not electrochemical but, instead, proceeds via reaction with lithium metal. The thermodynamic decomposition of Li_2O is less negative than that of the LiCl melt. This offers the ability to *chemically* reduce compounds of the actinides by reaction with lithium metal which is plated onto the metal oxide via decomposition of Li_2O.

Hur *et al.* reported the both the electrochemical reduction of U_3O_8 to UO_2 and the chemical reduction of U_3O_8 powder by electrochemically plating lithium onto the U_3O_8 working electrode [61]. In the former study, Hur reported that the reduction potential for the electrochemical reduction of U_3O_8 to UO_2 to be much

less negative to that of the decomposition potential of the molten salt (-0.48 V and -3.46 V respectively). This is in broad agreement to Littlewood diagrams of uranium species in LKE. However, the reduction potential of UO_2 was reported to be only 60 mV more negative to the reduction of Li_2O, whereby lithium metal is plated onto the working electrode. With this particular experimental set-up, the sole direct electroreduction of UO_2 to U would prove difficult, especially if an under-potential for the reduction of Li_2O were to exist, as it would be likely that the reduction of Li^+ would occur simultaneously. However, by deliberately plating lithium onto the U_3O_8 working electrode, Hur *et al.* proved that the reduction proceeds via a chemical reaction with lithium metal. The reaction pathway was attributed to be:

$$Li^+ + e^- \rightarrow Li \tag{2.19}$$

$$U_3O_8 + 16Li \rightarrow 3U + 16Li^+ + 8O^{2-} \tag{2.20}$$

Seo *et al.* published work in 2006 relating to the reduction mechanism of uranium oxide in LiCl containing Li_2O [62]. Two mechanisms were provided; Mechanism I and Mechanism II. The first was the chemical reduction of U_3O_8 by lithium metal when the cell was held at a more cathodic cell potential with respect to the decomposition potential of Li_2O. The second mechanism proceeded via the formation of lithium uranates at cell potentials more anodic to the decomposition potential of Li_2O. Within the study of Mechanism I, the local concentration of Li_2O was measured during the reaction. The concentration was seen to increase, providing more evidence that the reduction of uranium oxide proceeds via Equation 2.20, or more generally;

$$U_xO_y + 2yLi \rightarrow xU + 2yLi^+ + yO^{2-} \tag{2.21}$$

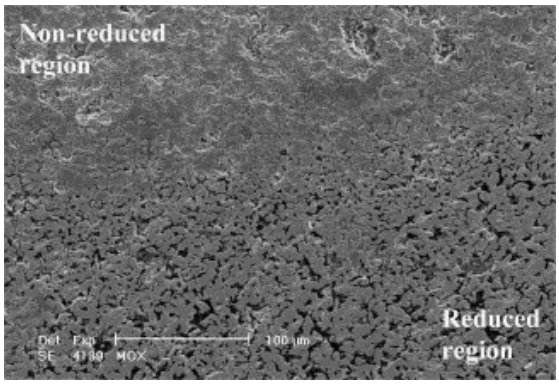

Fig. 2.5: SEM Micrograph showing a partially reduced mixed oxide (MOX) sample. The reduced region is seen to have a structured described as being "coral-like". Reprinted from Journal of Nuclear Materials, 328, *Electro-chemical reduction of MOX in LiCl*, Pages 97–102, Copyright (2004), with permission from Elsevier

During Mechanism II, X-ray diffraction analysis of reaction products showed that lithium uranates were formed during electrolysis. It should be noted that uranium oxides may be converted into lithium uranates according to the partial pressure of oxygen in the cell and the concentration of lithium oxide in the melt [65]. It is also suggested that the uranates that are formed are electrochemically reduced to uranium metal via the following equation:

$$Li_zU_xO_y + (2y - z)e^- + (2y - z)Li^+ \rightarrow xU + 2yLi^+yO^{2-} \qquad (2.22)$$

Jeong *et al.* also observed the two reduction mechanisms in a LiCl melt containing 1% mol. Li_2O [63]. X-ray diffraction analysis observed the formation of $LiUO_3$ as well as the formation of U_4O_9 and UO_2 during electrolysis of U_3O_8. Conversion of UO_2 to U was seen to be an electrochemical reduction as well as a chemical reduction via reaction with lithium metal. The authors also provided a scanning electron micrograph of the uranium product which showed a porous microstructure made up of globules with an approximate width of 10 µm.

Kurata *et al.* investigated the electrochemical reduction of spent MOX fuel in

LiCl [64]. Within this study, the author provided cyclic voltammograms showing the electrochemical reduction of the MOX fuel to be 200 mV more positive to the decomposition of Li_2O. The peak provided is relatively broad and does not show distinct reduction peaks for uranium oxide and plutonium oxide. This could be due to the fact that both of these oxides possess similar reduction potentials, causing the electroreduction peaks to be seen as a single, broad, peak. Also, it is possible that increased levels of CaO in the molten salt reduced the resolution of the two peaks. The microstructure of a partially reduced MOX fuel pellet was also provided and may be observed in Figure 2.5. This image shows two distinct regions; one of the regions shows the reduced part of the sample and other the unreduced region. The author described the reduced regions to have a "coral-like" structure which is similar to that provided by Jeong *et al.* There are a couple of noticeable differences between the reduced and unreduced regions; namely, the reduced region appears to be less dense to that of the unreduced regions. The reduction also appears to propagate from one side of the pellet to the other. The grain boundaries were seen to be reduced first before the reduction propagated into the grain itself. The difference in volume between uranium and it's oxide is attributed to the formation of the porous, "coral-like", structure.

2.2.4.2 Reduction in $CaCl_2$

Following on from the electrochemical reduction in LiCl-Li_2O melts, the electrochemical reduction of UO_2 has also been studied in $CaCl_2$. Sakamura *et al.* studied the direct electrochemical reduction of UO_2 to metallic U in both LiCl and $CaCl_2$ molten salts [66]. Within these investigations, the author showed the direct electrochemical reduction potential of UO_2 to U to be close to the cation's deposition potential, in agreement to that predicted by the Nernst equation and those shown by previous authors. Chronopotentiometry was used to reduce two samples in both of the molten salts. The two samples were different by their tap density; the first

samples were 83% of the density of the pure oxide for both LiCl and $CaCl_2$ salts. The second samples were 98% of the density of the oxide for the LiCl study and 94% for the $CaCl_2$ study.

During the electroreduction of UO_2 in $CaCl_2$, the author observed that the reduction propagated from the outside to the inside of the pellet. Considering the theory of triple phase interlines (see Section 2.3.2), one would expect the electroreduction to begin at the interface between the current collector and the pellet, located on the inside of the pellet. However, UO_2 is known to become sufficiently electronically conductive at temperatures in which $CaCl_2$ are used; UO_2 possesses an electronic conductivity of approximately 0.8 Ω^{-1} cm^{-1}at 1000 K compared to approximately 0.05 Ω^{-1} cm^{-1} 600 K [15, 16]. Because of the electronic conductivity of UO_2 at this temperature, the electrochemical reduction would be prominent at the point where there is an excess of molten salt; the outer region of the pellet. The author also observed the formation of a dense skin of metallic uranium which inhibited the penetration of molten salt and hence suppressed the electroreduction. The result was a pellet of unreduced UO_2 covered in a coat of reduced U. This phenomenon was not observed in the LiCl melt, even though it had a higher tap density and, therefore, was less porous. This was likely due to the low electronic conductivity of the oxide causing the electroreduction to not concentrate around the outside of the pellet. This allowed the diffusion of O^{2-} ions out of the pellet and into the bulk salt to be consumed at the anode, resulting in a more reduced sample compared to that in the $CaCl_2$ melt.

The current efficiency of the electroreduction in the $CaCl_2$ melt was calculated to be less than that in the LiCl melt. This was attributed to a calcium deposition under-potential that was not observed in the LiCl melt. Calcium metal is much more soluble in $CaCl_2$ than lithium metal is in LiCl. This, according to the author, could explain the presence of the under-potential. Because the electroreduction of UO_2 is close to the decomposition potential of the molten salt, any under-potential could

see calcium metal being reduced at the cathode simultaneously to the reduction of UO_2. The calcium would dissolve into the melt and could then be oxidised at the anode, causing a low current efficiency. Similar observations were seen by Iizuka *et al.* who reduced spent MOX pellets in $CaCl_2$ [67].

The electrochemical reduction studies reviewed within this subsection all show the feasibility of reducing UO_2 to metallic U in molten salt media. Perhaps the most important conclusion to draw from these investigations is the fact that the electrochemical reduction of UO_2 to it's metallic form appears to occur in a single step which involves the transfer of 4-electrons;

$$UO_2 + 4e^- \rightarrow U + 2O^{2-} \tag{2.23}$$

Moreover, it is important to conclude that the electrochemical reduction potential of Equation 2.23 is very negative (*ca.* -2.4 V wrt. $Ag|Ag^+$), due to the very negative Gibbs free energy of formation of UO_2. This means that the reduction potential is close to that of the cathodic deposition potential of the molten salt. In a LKE molten salt, there is a chance of lithium metal plating onto the UO_2 cathode causing the reduction to proceed via a chemical reaction as described in Section 2.2.4.1. Although this development would achieve the ultimate goal of reducing UO_2 to it's metal, this may not be desirable in an industrial process as it may inhibit the ability to selectively reduce specific species.

In addition, the microstructural evaluation of the electrodes has shown significant microstructural restructuring during the electrochemical reduction. Dense microstructures have shown to become more porous after electroreduction in molten salts. This change has been seen to both inhibit and facilitate the electroreduction in different molten salts. However, it must be said, that these studies have been carried out using electron microscopy and are thus two-dimensional studies. In order to draw more valid conclusions, a three-dimensional evaluation of the microstructure

should be adopted.

2.2.5 Pyroprocessing (Electrorefining)

Because one is able to titrate species into a molten salt and then recover them electrochemically, this opens up the possibility of an industrial process of the recovery of species. The excellent electrolytic properties of molten salts allow their application to the electrorefining of actinide metals for nuclear recovery. Pyroprocessing or electrorefining is exemplified by the refining process developed by the Argonne National Laboratory in the 1990's. The aim of this reprocessing technology was to reprocess fuel from the integral fast reactor, a liquid metal cooled prototype reactor which was abandoned by the US in the mid-nineties.

In the early 1990s, Pierce presented a method by which actinides could be recovered via a pyrochemical (a combination of pyrometallurgical and electrorefining processes) route [68]. This paper describes the entire pyrochemical process route, including the electrorefining of uranium in molten LiCl-KCl eutectic (LKE). However, only a basic written description of the electrorefiner was presented. The electrorefiner was not widely understood until Laidler presented a more in-depth discussion of the electrorefining step [69, 70].

In these reports, Laidler presented a 100 cm diameter x 100 cm height electrorefining cell made from stainless steel. A 15 cm thick layer of cadmium is placed at the bottom of the cell and, above this; molten LKE is used as the electrolyte, operating at 500°C (see Figure 2.6 for a schematic). The cell contained an anode basket in which chopped fuel rods are placed. Cadmium chloride is also added to the melt as a dissolution mechanism, allowing for a sufficient concentration of actinides in the melt and to promote sustainable electro-transport. A solid stainless steel cathode is used and this set-up allows for a dendritic uranium metal to be deposited at a rate of 3 g Ah^{-1} using a potential difference of approximately 1 V. Any breakage of this dendrite would settle into the cadmium layer which could then be recovered by

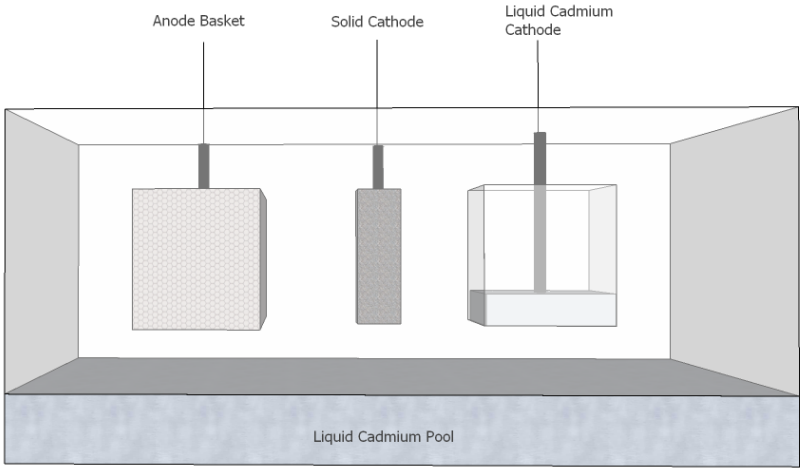

Fig. 2.6: A schematic of an electrorefining cell. Chopped spent fuel rods are placed inside the anode basket. Cadmium chloride is added to the cell to titrate some of the spent fuel into the molten salt. Uranium is deposited onto the solid cathode as highlighted in Section 2.2.3.1. Plutonium is recovered with the use of the liquid cathode. Proliferation resistance is maintained due to the inability to deposit pure plutonium at the liquid cathode.

applying a voltage across the cadmium pool and the cathode. Laidler, also explored the deposition mechanism of plutonium too. It was found that plutonium couldn't be deposited at this solid steel cathode as the chlorides of plutonium and uranium are in equilibrium with each other, according to the reaction:

$$UCl_3 + Pu \rightarrow U + PuCl_3 \quad \triangle G = -100.75\,kJ/mol \tag{2.24}$$

Therefore, any plutonium which was deposited would instantaneously react with UCl_3 in the melt, resulting in $PuCl_3$. Laidler reported that in order to be able to deposit plutonium, the Pu:U ratio needs to be increased and so a second, liquid cadmium, cathode was introduced into the set-up to deposit plutonium. Proliferation resistance is maintained as this is not a pure plutonium deposit but a mixture of plutonium, americium, neptunium, curium, uranium and some rare earth fission products.

Further to this, Hur explored the reduction of spent Light Water Reactor (LWR)

fuels, UO_2 and U_3O_8, in a molten Li_2O-LiCl salt in an inert atmosphere at 650°C [61, 71]. This work described the chemical route which saw lithium act as a transporter of the oxygen in the uranium oxide. It was concluded that two lithium ions from the salt would be reduced into Li_2O, diffuse through the salt and then become oxidised at the anode producing two lithium ions and oxygen gas, when using a platinum anode. When a graphite electrode was used, the oxygen ions were discharged as CO or CO_2. Linear sweep voltammetry was used to characterise the reduction of uranium oxide concluding that the use of Li_2O-LiCl molten salt was a feasible option.

By understanding the stability and dissolution of species into molten salts, it is apparent for separation processes to be conceived such as the pyroprocessing route described in this section. However, the studies presented by Laidler and Pierce both contain very vague descriptions of the process itself. The quantities of cadmium chloride added to the melt are not described, leading to the inability to calculate the activity of, say, U^{3+} ions in the melt. Moreover, the potential for electroplating of uranium species was vague too. However, the reports in the section do show the inherent success of actinide separation with the use of molten salts deployed as electrolytes.

2.3 Review of Microstructural Characterisation and Tomography Techniques

The microstructure of an electrode may have a significant effect on the bulk performance of the system [72-74]. Many of the characteristics of the microstructure dictate the reaction kinetics of the system. For example, the shape of a number of local 3D grains in porous media will dictate the local porosity and tortuosity, as well as other characteristics. Phenomena that are governed by the connectivity between microstructural features must be modelled in three dimensions [75]. Translating this to the system described in this thesis, the diffusion of the ions from the electrolyte

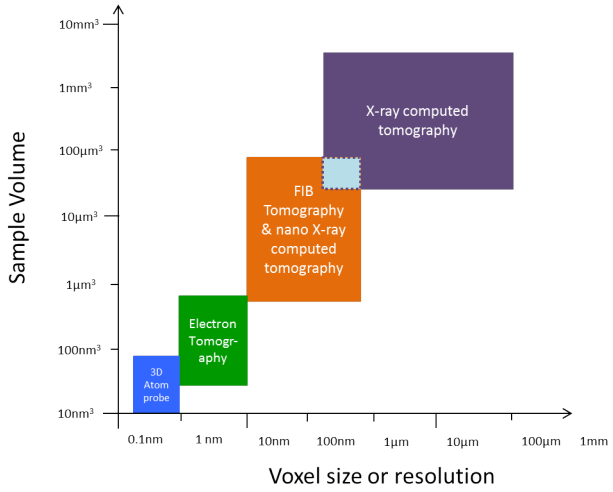

Fig. 2.7: A graph showing the volume analysed by tomography and the resolution (or voxel size) of the reconstruction. The graph highlights the fact that in order to analyse a larger volume, the resolution of the reconstruction is reduced and vice versa. Adapted from [71].

to the reaction site (and vice versa) will be a function of the overall tortuosity of the pores which is, inherently, the connectivity between microstructural features. Two dimensional characterisation techniques, such as scanning electron microscopy (SEM), are unable to analyse the three dimensional features such as the true porosity and tortuosity of the bulk sample (Although SEM may provide a degree of 3D information, the scale of this is negligible and is regarded as 2D information in this thesis). Therefore, the microstructure can not be fully characterised in two dimensions; it needs to be evaluated in three dimensions in order to extract true information on how the microstructural phenomena effects the bulk performance of electrodes.

It is important to highlight that with any tomography technique, there is always a trade-off between the volume of sample studied and the resolution, as shown in Figure 2.7. It is necessary to analyse a volume that is characteristic of the bulk electrode because local imperfections may be analysed that are not representative of the bulk electrode. However, at higher volumes, the resolution of the images is

typically lower and so all the physical phenomena may not be extracted. Figure 2.7 depicts the differing volumes and resolutions that different tomography technologies can achieve [76]. Focused ion beam tomography and X-ray computed tomography are best suited for the work described in this thesis.

There are many tools available that allow one to analyse the microstructure both invasively and non-invasively. Currently, the literature does not contain many studies regarding the microstructure of electrodes used for electroreduction. However, the literature does contain many reports on the microstructure of other electrochemical cells; namely fuel cell and battery systems [77-81]. The latter sub-sections explore the literature on studies completed regarding microstructural characterisation of fuel cell and battery electrodes to provide an insight into how the techniques can be adapted into the work of this thesis. Sub-sections 2.3.1 and 2.3.2 explore the FFC Cambridge process with a view of the microstructural characteristics that may be extracted.

2.3.1 2D Microstructural Evaluation of the FFC Cambridge Process

In order to understand the microstructural characterisation of electrodes in molten salt applications, the FFC Cambridge process (Section 2.1) is reviewed in this section. However, the studies use scanning electron microscopy to deduce the microstructural characteristics and, thus, is only a two dimensional study. This will highlight the need to study the microstructure in three dimensions.

Alexander *et al.* carried out a microstructural kinetic analysis of the reaction procedure of the reduction of TiO_2 to Ti [22]. The experimental procedure was similar to that described by Schwandt. The work was broken down into a set of stages, each describing the microstructural changes of the equations listed in Table 2.1 in Section 2.1. The characterisation during each stage showed significant microstructural reconstruction throughout the three stages, as shown in Figure 2.8. The microstructure of the initial samples of TiO_2 powder and Indian rutile powder

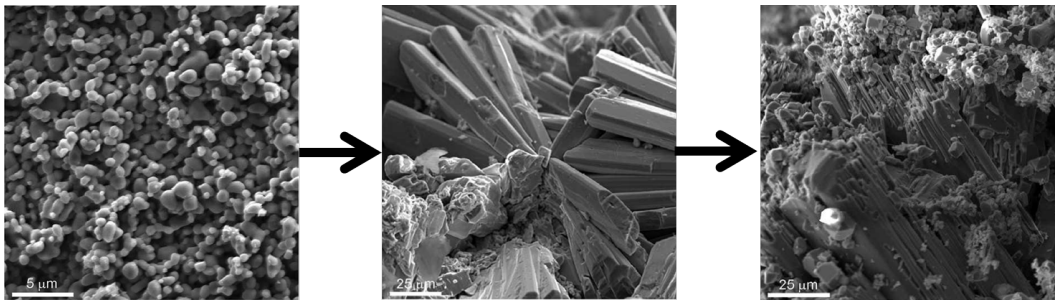

Fig. 2.8: SEM micrographs showing the microstructural evolution of (a) the initial TiO_2 powder to (b) $CaTi_2O_4$ to (c) TiO. Adapted and reprinted from Acta Materialia, 54, *Microstructural kinetics of phase transformations during electrochemical reduction of titanium dioxide in molten calcium chloride*, Pages 2933–2944, Copyright (2005), with permission from Elsevier

had particle sizes of *ca.* 1 µm and over 100 µm respectively. During phase 1 it was observed that the electrochemical reaction with the electrolyte caused $CaTiO_3$ to form on the perimeter of the particles. This was attributed to the fact that calcium ions are more readily available at the surface of the particles. It was also observed that the interior of the particles had reduced to Ti_2O_3. This reduction proceeded with little effect on the microstructure. During the latter stages of phase 1, the formation of the much denser TiO resulted in significant reconstruction of the microstructure. Due to this reconstruction, the kinetics of the reaction are slowed as the Ti_2O_3 breaks up, nucleates and grows. This growth causes voids to appear, allowing for more electrolyte to reach the Ti_2O_3 particles and electrochemically react. This phenomenon causes the exterior of the particles to become more reduced than the interior. The particles can be seen to have grown to *ca.* 10 µm from *ca.* 1 µm. Following this was the reduction of $CaTiO_3$ and TiO to form $CaTi_2O_4$. This reaction proceeds via a chemical, rather than electrochemical, reaction. Complementary to this reaction is another substantial reformation of the microstructure and the particles were observed to have formed larger, 'lath-shaped needles' of $CaTi_2O_4$ several orders of magnitude in size compared to the initial samples. The last phase is the formation of TiO from $CaTi_2O_4$. Again, a major microstructural reconstruction

occurred with this electrochemical reaction. Alexander *et al.* describes the microstructure changing from the large needles into small, cubical and equiaxed, TiO particles. The reaction occurred at the front of the particles and proceeded to move inwards as calcium oxide dissolved into the melt and was transported to the carbon anode producing carbon monoxide and carbon dioxide.

In conclusion, Alexander *et al.* was able to report that significant microstructural changes occur during the reduction of TiO_2 to Ti. This microstructural reconstruction (nucleation and growth) has rate limiting effects on the reaction and thus not prohibiting the estimation of the rate of reaction via a thermodynamic only route. Further work is needed in order to be able to optimise the reduction process of titanium dioxide to titanium. This study proves the inherent need to characterise microstructures in three dimensions. Microstructural nucleation, growth and other phenomena like salt percolation are all three dimensional characteristics and this report highlights the need to characterise these complex structures in three dimensions. By studying the microstructure in two dimensions, characterisation of the microstructure significantly reduces the resolution and does not permit for three dimensional properties, such as porosity and tortuosity (which can dictate reaction kinetics) to be extracted.

2.3.2 Three Phase Interlines

A three phase interline (TPI) is defined as the points whereby the current collector/fully reduced metal (electronic conductor), the metal oxide (which is typically an electronic insulator) and the electrolyte meet, *i.e.* the conductor|insulator|electrolyte interline [82]. This TPI is the point at which the reaction will take place; the insulator needs to be present as this is the specimen that will be reduced; the conductor phase will allow the transfer of electrons and the electrolyte allows for the transport of ions.

TPIs are naturally a property of the microstructure; a microstructure that con-

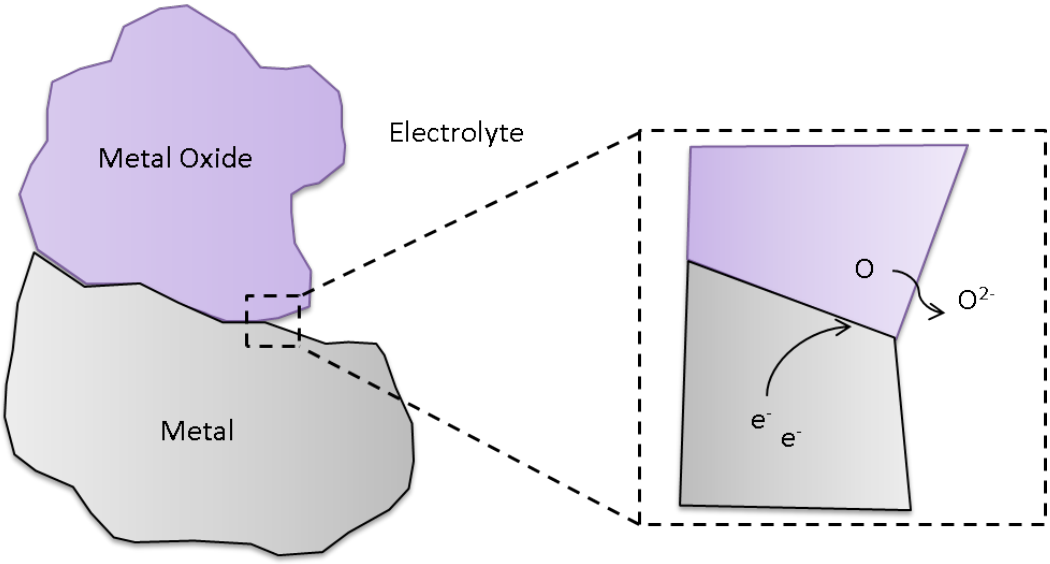

Fig. 2.9: A schematic to visualise Triple Phase Interlines. The schematic shows a metal (electronic conductor, grey shade) in contact with the metal oxide (insulator, purple shade) and electrolyte (ionic conductor, white). Only at the interface between the three phases may the electrochemical reaction occur. The zoomed region shows the oxygen reduction mechanism within the microstructure. Note that the interlines would extend into/out of the page.

tains a wealth of percolated pores would allow for a higher TPI density and, therefore, a higher reaction rate. Figure 2.9 is a schematic of triple phase interlines that may be present in a microstructure of a metallic phase (grey) and an oxide phase (purple) combination; the microstructure shown is surrounded by the electrolyte. One can see that only the regions where the insulator, conductor and electrolyte would be active in the electrochemical reaction. An example is shown in the zoomed region of Figure 2.9. Any other pores that may exists within the macrostructure (not shown) may be considered as inactive as they are not contributing to TPIs. Because of a change of phase associated with electrochemical reductions, there may be a change in the microstructure. This could lead to a change in TPI density and percolation, resulting in a change in the performance of the electrode.

Deng *et al.* proposed a simple, thin layer, electrochemical model that accounted

for a dynamic triple phase interline in $CaCl_2$. This model was able to demonstrate good predictions of the behaviour of a a silver wire in contact with AgCl in a KCl solution [82]. The model was able to predict the linear expansion of a circular TPI in contact with the silver wire and the exponential behaviour of the expansion as a function of applied potential. However, the authors did not use experimentally determined TPIs. Meanwhile, Xiao *et al.* proposed a novel "penetration" model which allowed modelling of the dynamic TPIs. The model was able to deduce some key information such as the optimum polarisation potential leading to the fastest reduction and lowest energy consumption [83]. This model was further expanded in 2007 in order to estimate the diffusion coefficient of the O^{2-} ion and the resistivity in the porous metal layer of the working electrode [84].

Triple phase interlines are defined as the point(s) in which the electronic insulator, electronic conductor and ionic conductor phase are in contact with one another. Although at the temperatures used within the scope of this thesis may be sufficiently high for uranium oxide to be electronically conductive, this TPI may still play a vital role in the efficiency of the electrochemical reduction process. From the models reviewed in Section 2.3.2, it can be seen that the TPIs are a dynamic property of the microstructure. Because of the continued evolution of the TPIs the microstructure of the electrode become more or less dense with TPIs. This, inherently, will affect the bulk performance of the electrode; showing the importance of the TPI density within the microstructure.

2.3.3 Focused Ion Beam Tomography

Focused Ion Beam (FIB) tomography is an invasive tomographic technique and can be used to reconstruct microstructures. For background information on this technique, the reader is referred to Section 3.2.1. Morphology studies can be carried out using imaging via SEM or FIB. The morphology of the cathode is particularly important as it will have an affect on microstructural characteristics which can, in

turn, have significant effect on reaction kinetics. For example, if the morphology contains poorly connected pore tortuosity, then the three phase interline density will be reduced. This reduction in TPI density will cause a low metallic product yield as the electrochemical reaction will not be able to take place across the whole of the sample.

A report on the three-dimensional reconstruction of a solid oxide fuel cell anode using the FIB tomography technique was presented in 2006 [79]. From this study, the author was able to present the first direct measurement for the Triple Phase Boundary (TPB) length; other measurements were estimated from 2D images (*i.e.* [85]). Also, the gas phase tortuosity was extracted from this tomography data using a finite element mesh procedure using commercially available software. The tortuosity was extracted for the three primary axis (x,y,z) and was deduced to be approximately 2, which is consistent with typical fuel cell electrodes [86, 87]. Wilson was also able to reconstruct a 3D image of the electrode, highlighting the different phases. Moreover, a highly valuable 3D map of the triple phase boundaries was presented which showed that 63% of the TPBs were connected. This report highlights the key advantages of 3D tomography and proves that three dimensional analysis is a powerful tool in characterising microstructures.

Furthermore, a study which also utilizes the focused ion beam tomography technique was presented in 2009 [88]. Two FIB tomography techniques were presented; a single beam set-up and a dual beam set-up. The former uses the FIB to both mill and image. For this set-up, the sample stage must be actuated in between each milling and imaging step as the beam must be incident parallel to the sample (to ensure uniform sputtering) whereas the beam should be at a 45° angle to the face of interest during imaging. For the latter technique, the FIB/SEM combination (described in Section 3.2.1) was utilized. Three dimensional reconstructions were obtained from both tomography techniques and compared and contrasted. The results showed a volume percentage porosity to be 11.36% and 11.30% for the sin-

gle and dual beam reconstructions respectively. This result was to be expected as samples for microstructural characterisation were taken from the same precursor. The reconstructions, however, do show that the dual beam technique is able to afford a much higher volume reconstruction. The total volume reconstructions were 75.05 μm^3 and 721.96 μm^3 for the single beam and dual beam respectively, thus representing the bulk electrode more than the single beam approach.

This work was then extended in 2010 and 2011 respectively [89, 90]. The dual beam approach was used to reconstruct a volume of 6.62 x 5.04 x 1.50μm by stacking a sequence of 170 images. The tomography data obtained was coupled with electrochemical impedance spectroscopy. This data was then compared to electrochemical simulations. The results indicated a broad agreement between the simulations and characterisation with the discrepancies being put down to underlying assumptions. Meanwhile, a finite element mesh was also incorporated to the tomography data to conduct a thermo-mechanical stress analysis. The results indicated that the thermal expansion of the Ni and YSZ phases generate internal stresses within the microstructure. These stresses peaked at the interfaces of the two solid phases, indicating that this is potentially an important mechanism for relieving stress in Ni-YSZ electrodes.

These studies highlight both the advantages and disadvantages of using tomography. To take into account the former; being able to couple the microstructural information with electrochemical/mechanical simulations provides an insight to the phenomena on the sub-μm length scales. Understanding the physical phenomena at these length scales provides the possibility of optimising electrode designs for properties such as porosity, tortuosity and TPB or TPI density. However, the drawback with FIB tomography is the destructive nature of the technique. Once the sample has been milled by the FIB, the material is unrecoverable. This translates into the sample not being comparable to itself in a before/after reduction investigation, for example.

2.3.4 X-Ray Computed Tomography

X-Ray Computed Tomography (X-ray CT) is a non-invasive tomography technique. The main disadvantage for traditional X-ray CT is the resolution of this tomography technique is typically lower than that of FIB tomography (Figure 2.7). For background information on this technique, the reader is referred to Section 3.2.2.

A report in early 2010 was published which adopts a nano X-ray CT technique to look at the microstructure of solid oxide fuel cell (SOFC) electrodes [91]. In this report, NiO-YSZ (Yttria Stabilized zirconia) was pressed, sintered and reduced to create a Ni-YSZ pellet which was representative of a SOFC electrode. The nano-CT scanner employed a rotating sample stage and enabled two magnifications of 200x and 800x. The two magnifications enabled a spacial resolution of 200nm and 50nm respectively. In order to reconstruct the images properly, it was important to ensure that the sample is completely contained within the field of view (FOV) during rotation. For this, a FIB lift out technique was used. X-ray projection images were collected at steps of 0.2° across a total rotation of 180°. Amira visualisation and analysis software was then used to reconstruct the microstructure of the SOFC electrode (see [91] for details of the techniques used). The results enabled the author to calculate the porosity of the microstructure to be 8.81% at 800x magnification and 9.25% at 200x magnification which was in agreement to that calculated via FIB techniques of 9.42%. Moreover, the solid phase reconstruction proved that X-ray CT was a viable tool to reconstruct the microstructure of electrodes which is representative of the bulk material.

Later that year, another study was published regarding an analysis of triple phase boundary contact in Ni-YSZ microstructures using X-ray CT [92]. The aim of this study was to depict a comprehensive microstructural map of a SOFC electrode. The samples were prepared using the FIB lift-out method described previously and was characterized using nano-CT [91]. The results of this report showed

that microstructures of electrodes provide some heterogeneous properties (such as triple-phase contacts, porosity, compositions etc.) but these are compensated, at large, by the majority of the microstructure being homogeneous.

This work was then extended to characterise the electrode of a lithium ion battery. Sample volumes of 43 x 348 x 478μm were reconstructed and computed physical properties such as tortuosity, surface area, porosity and particle & pore size distributions [93]. A geometrical analysis was able to provide data that 95% of the pores actually percolated through the entire sample, meaning only 5% of the pores were unable to facilitate electrochemical reactions. The report also provides mosaic plots showing the spacial distribution of tortuosity, surface area and porosity through the sample.

These studies clearly highlight the inherent advantages of X-ray CT; the technique is able to fully characterise microstructures that are representative of the bulk electrode in a non destructive manner, allowing for microstructural evolution to be studied. Moreover, many analytical tools can be used to extract a range of different properties of the microstructure which can be coupled with modelling simulations to not only deduce what is happening within the microstructure but, also, to help optimise the system.

2.3.5 Other Tomography Studies

Following on from the investigations reviewed in the two previous sections, this subsection aims to review literature on tomographic studies that are not focused on electrochemical devices. The aim of this is to deduce the importance of tomographic studies and to show how these studies could be important to the work of this thesis.

A multi-scale tomography study was concluded in 2011 whereby the author used synchrotron X-ray micro-tomography, FIB tomography and electron tomography to study flow channels in porous catalytic structures [94]. Two silica-alumina samples, sintered at different temperature, were studied using multi-scale tomography to de-

duce the effect of sintering temperature on molecular transport through the catalytic structure. By using the microstructural characteristics extracted from the tomography data, the author was able to run a computational fluid dynamic study. This marriage of techniques showed that the lower temperature sintering gave rise to the catalytic structure having larger pores with significantly better transport processes.

A study in 2009 used X-ray CT to discretize the three dimensional structure of a metal based foam scaffold used as bone/cartilage implants [95]. The X-ray CT was obtained using a commercial laboratory based X-ray micro-computed tomography unit. A finite element mesh was applied to this structure to model the elasto-plastic deformation behaviour. A simulation was performed to characterize the mechanical properties by incorporating static and incremental compression tests. The study revealed the most vulnerable regions to failure during mechanical stress.

Synchrotron radiation was used to study the nucleation of micro cracks in a study carried out in 2004 [96]. Miniature fatigue specimens were designed into the cast iron sample which was exposed to a stress cycle. Tomography was conducted before, after and at intervals during the stress cycling. From the reconstructions, the author was able to detect and follow the nucleation of a series of micro-cracks in the structure. The authors concluded that all of the cracks initially grew quickly and then started to decelerate before arrest.

These studies aim to highlight the power of tomography as a research tool. Perhaps the most important conclusion one can draw from this review is the ability to marry tomography data with modelling and simulation software packages to enable one to study how the microstructure affects the bulk performance of the sample. In addition, having the ability to follow the evolution of microstructural characteristics (such as micro-cracks) could be an invaluable tool for the work of this thesis.

2.4 Summary of Literature Review

This literature survey shows the complex nature of the topic under investigation. Studies have all highlighted the apparent stability of actinide species in LKE and have shown the ability to anodically dissolve and cathodically plate species. Other reports have also shown the applicability of molten salt processing of nuclear fuels on the kg scale.

Although many reports have shown the topic of this investigation to be feasible, there is still a need to study the fundamental phenomena within this work. In terms of the electrochemical reduction of uranium oxide to uranium, the studies presented show that this process may be feasible within the lower temperature molten salt of LKE. However, many of the reported potentials for electroreduction differ which could be due to the differences in experimental set-ups. There are also deviations with the stability of uranium species in molten LKE, as well as other actinides and fission products. Electrodeposition potentials also had deviations between authors.

Some very important conclusions may be drawn from the studies of the electrochemical reduction of uranium oxides in calcium chloride and lithium chloride; namely, the apparent direct electrochemical reduction from UO_2 to U with no observable intermediate steps. The electrochemical reduction potentials were all reported to be very close (*ca.* 200mV more positive) to the deposition voltage of the molten salt's cation. With a LKE system, any decomposition of the electrolyte will lead to the formation of lithium metal onto the uranium oxide working electrode. This, will cause the uranium oxide to be reduced to uranium metal via a chemical reaction rather than electrochemically. Although this will result in the desired product, this may not be desirable in an industrial process where the selective reduction of actinide oxides is critical.

One of the most striking observations drawn from this literature survey is the lack of investigations into the effect of oxide ion concentration on the electrochemistry

and how the evolution of the electrode's microstructure affects this phenomena. It has been highlighted that the potential for the electrochemical reduction is a function of the local activity of oxide ions within the microstructure; a variable which would seem to be dynamic during the electroreduction - a function of the inherent microstructure of the electrode.

The microstructure of the electrode is also known to play an important part of the overall efficiency and performance of the electrode. The technique of obtaining tomography data will deduce the total volume that is able to be analysed and the resolution. The techniques of X-ray CT and FIB tomography have both proven successful in being able to reconstruct a representative volume of electrochemical electrode microstructures with high resolutions. The main disadvantage of FIB tomography is the destructive nature of the technique. It will be impossible to analyse the exact same volume before and after electrochemical reduction.

Chapter III. Methodology

3 Methodology

Drawing upon the topics discussed in the Literature Review, this part of the thesis describes the experimental techniques used throughout the work underlining this thesis. Each technique which has been used is described in context to molten salt electrolysis. Process conditions, electrode configurations and the use of different techniques will be discussed and evaluated.

3.1 Electrochemical Techniques

Molten salts at operating temperatures (typically above 350°C) usually produce complete dissociation of the salt, resulting in a high temperature ionic liquid system. In addition, dissolution of salts into a molten salt cause that salt to completely dissociate into its anion and cation respectively, followed by complete integration into the ionic structure of the molten salt. With this, one is able to conceive electrochemical systems within molten salts, as highlighted in Sections 2.2.1 - 2.2.5. Therefore, molten salt systems may be used as electrochemical electrolytes which provide higher kinetics compared to ionic liquids used at (or near) room temperature. The following subsections will provide the theory and explanation of the electrochemical techniques used in this work.

3.1.1 Linear Sweep Voltammetry

Linear sweep voltammetry (LSV) is a technique whereby the voltage between the working electrode and reference electrode is swept linearly in time. The current passed between the working electrode and counter electrode is recorded and redox voltages of species is registered as a current peak at the voltage at which the species is reduced or oxidised. This technique may be used to ascertain the decomposition

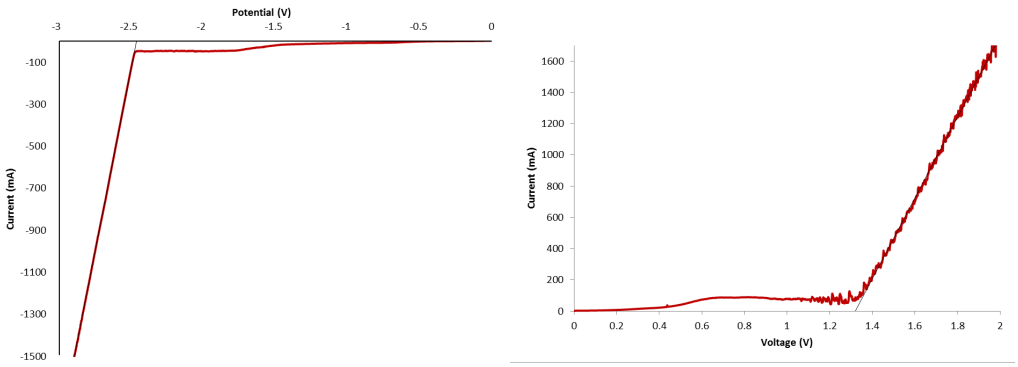

Fig. 3.1: Linear sweep voltammograms at a sweep rate of 100mV $s^{-1}$and a temperature of 400°C using tungsten working and counter electrodes and a Ag|AgCl reference electrode. (a) shows the deposition potential of lithium at -2.45 V. (b) is the evolution of chloride at the working electrode, occurring at +1.3 V.

voltage(s) of an electrolyte, or indeed to study electrochemical phenomena in molten salt electrochemistry [97].

The scan rate can be altered to study different phenomena that may occur within the electrochemical cell. The scan rate is simply the rate at which the voltage is swept and has units, typically, of mV/s. If a low scan rate is adopted, the system will be limited by electron transfer as the slow scan rate impedes the movement of electrons. On the other hand, if a high scan rate is used, then the system will be diffusion limited; electrons are readily available but ions, which are usually supplied by diffusion through the molten salt (melt), are limited by the rate of diffusion.

LSV was used to experimentally determine both the anodic evolution potential of chlorine gas and the cathodic deposition potential of lithium metal in the LKE electrolyte. These values were calculated to be -2.45 V and +1.32 V respectively (with reference to the Ag|AgCl reference electrode, see Section 4.6) and can be seen in Figure 3.1. This gives rise to the LKE electrolyte having a potential window of 3.77 V, which is in agreement to the thermodynamic prediction presented in Chapter 5.

Figure 3.1 (a) is the linear sweep voltammogram at the cathodic extreme. As the potential is swept from a value of 0 V, the current response starts to become more negative. This is likely due to double layer capacitance effects, as expected. Once the potential reaches a value of -2.45V, there is a significant increase in the current response (ignoring the minus sign - this is only indicative of the direction of electron flow). At potentials more negative than -2.45V, the formation of lithium metal is thermodynamically favourable, as described by the equation

$$Li^+ + e^- \rightarrow Li \; \Delta G = -349 kJ/mol \tag{3.1}$$

Where the Gibbs free energy stated is with respect to the Cl|Cl$^-$ system (*i.e.* the Gibbs free energy of formation for chlorine is 0 kJ/mol.). Figure 3.1(b) shows the anodic potential sweep voltammogram . Salt decomposition is seen to occur at *ca.* 1.1 V, after which the current response becomes more noisy. This is due to the formation of chlorine gas bubbles on the surface of the electrode, as described by the equation:

$$2Cl^- \rightarrow Cl_2 + 2e^- \; \Delta G = 0 kJ/mol \tag{3.2}$$

The formation of bubbles reduces the surface area of the electrode that is open to the electrolyte. This, in turn, causes the impedance of the electrode/electrolyte interface to increase and hence current to decrease. Once the bubbles are evolved from the surface of the electrode, the surface area increases, causing the impedance to drop and thus the current to increase.

To conclude, linear sweep voltammetry is a DC based electrochemical method based on sweeping the potential linearly in time. In the context of this section, LSV has been used to calculate the decomposition potentials in LKE at 400°C. The decomposition potentials were inferred by sweeping from 0V to extreme potentials both positive and negative to this. This resulted in the decomposition of the salt onto

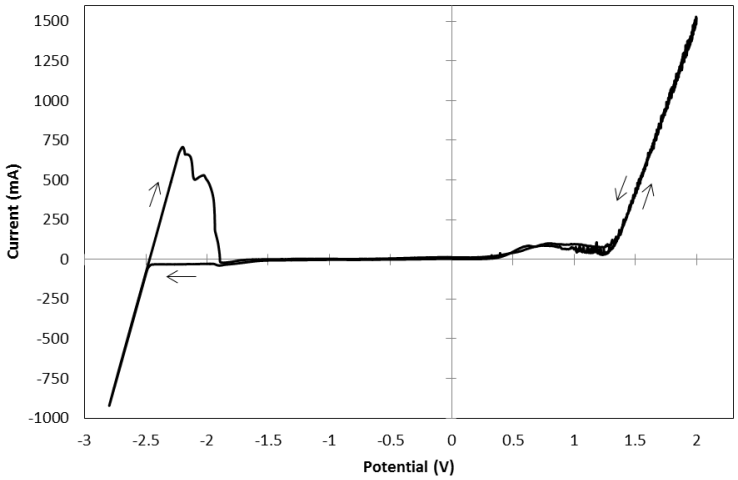

Fig. 3.2: Cyclic Voltammogram of LKE at 400°C. A tungsten working electrode was used with a graphite counter electrode and Ag|AgCl reference electrode. Many similarities exist between the CV here and the LSV technique shown in Figure 3.1. The main difference is the currents passed on the anodic scan from -2.45 V to -1.8 V which is due to the re-oxidation of lithium.

the working electrode as described by Equations 3.1 and 3.2. It should also be noted that LSV may also be used to study the reversibility of electrochemical reactions, although a more popular technique for this type of study is cyclic voltammetry.

3.1.2 Cyclic Voltammetry

Cyclic Voltammetry, as with LSV, is a DC electrochemical technique. The difference between cyclic voltammetry is that when a vertex potential is reached, the direction of the linear sweep is then reversed. This allows for the applied potential to cycle from one potential to another a number of times. A major difference between the two voltammetry techniques is that cyclic voltammetry is able to identify redox couples, *i.e* peaks associated with the reduction and oxidation of species.

A cyclic voltammogram (CV) was obtained from a cell operating at 400°C with tungsten working and counter electrodes. The CV is shown in Figure 3.2. The scan begins sweeping cathodically from 0 V to a minimum of -2.8 V. After -2.45 V, the CV depicts a large current response. This is due to the scan reaching the deposition

voltage of lithium *(cf.* Equation 3.1). Lithium continues to plate from -2.45 V until the vertex potential of -2.8 V. At this point the sweep direction is reversed. Lithium continues to plate until the potential of -2.45V is reached. As the potential becomes more positive of this value, lithium ions become thermodynamically more favourable. The result is a large, positive, current response which is due to the dissolution of the deposited lithium back into the bulk melt:

$$Li \rightarrow Li^{+} + e^{-} \tag{3.3}$$

This is a good example showing the advantage of cyclic voltammetry over linear sweep voltammetry. Comparing the decomposition potential inferred from Figure 3.2 to that obtained by LSV (Figures 3.1(a) and (b)) one can observe both methods have deduced equal anodic and cathodic decomposition potentials, defining the potential window to be 3.77 V.

In conclusion, cyclic voltammetry sweeps from one potential to another, linearly with time. The difference between cyclic voltammetry and LSV is the ability to reverse the direction of sweep a number of times. This can be seen from the potential-time curves in Figure 3.3.

3.1.3 ChronoAmperometry/ChronoPotentiometry

Following on from the sweep techniques outlined in Sections 3.1.1 and 3.1.2, the last DC electrochemical techniques used in this work are chronoamperometry and chronopotentiometry. Chronoamperometry is a technique whereby by the potential of the working electrode is held constant for a defined period of time and the current response is measured, where as the opposite is true for chronopotentiometry; that is, the current drawn from/applied to the cell is held constant and the potential difference of the cell is measured.

Chronoamperometry is a useful technique which may be employed, for example,

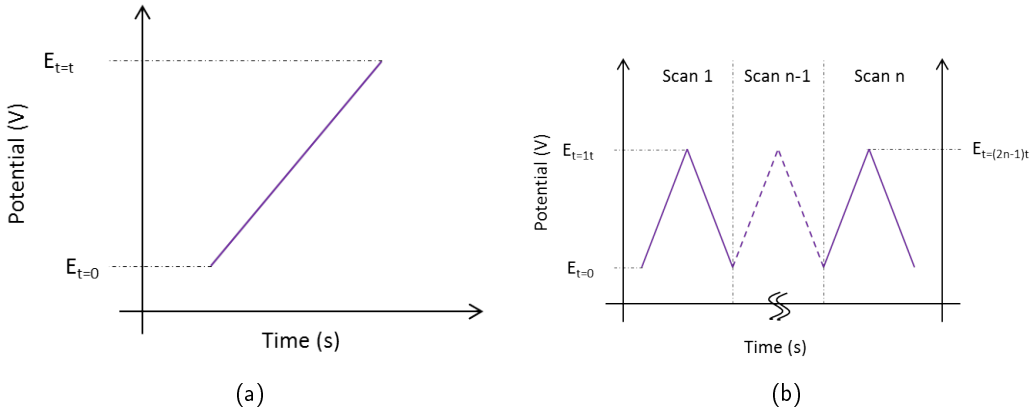

Fig. 3.3: Potential-time graphs for (a) linear sweep voltammetry and (b) cyclic voltammetry. LSV is a single sweep from one potential, $E_{t=0}$, to another potential, $E_{t=t}$. CV reverses the sweep after $E_{t=t}$ has been reached and returns the potential to the same value as $E_{t=0}$. This cycle may be repeated N number of times.

to decontaminate a molten salt electrolyte. That is, a potential more positive of the alkali/alkali earth metal deposition potential may be applied for a prolonged period of time, known as pre-electrolysis [98]. Any electro-active species that are contaminating the molten salt are therefore removed from the molten salt, either by a solid/liquid deposit (the latter, if more dense than the molten salt, may collect at the bottom of the cell) or by the formation of gaseous species. For example, if the melt was contaminated by dissolved $PbCl_2$ (existing as completely dissociated anions and cations), pre-electrolysis would remove these species as described by the following equations:

$$Cathode : Pb^{2+} + 2e^- \rightarrow Pb \tag{3.4}$$

$$Anode : 2Cl^- \rightarrow Cl_2 + 2e^- \tag{3.5}$$

The lead formed from Equation 3.4 would either alloy with the working electrode or form a pool of liquid lead at the bottom of the electrochemical cell. The chlorine formed from Equation 3.5 would escape the melt as gas.

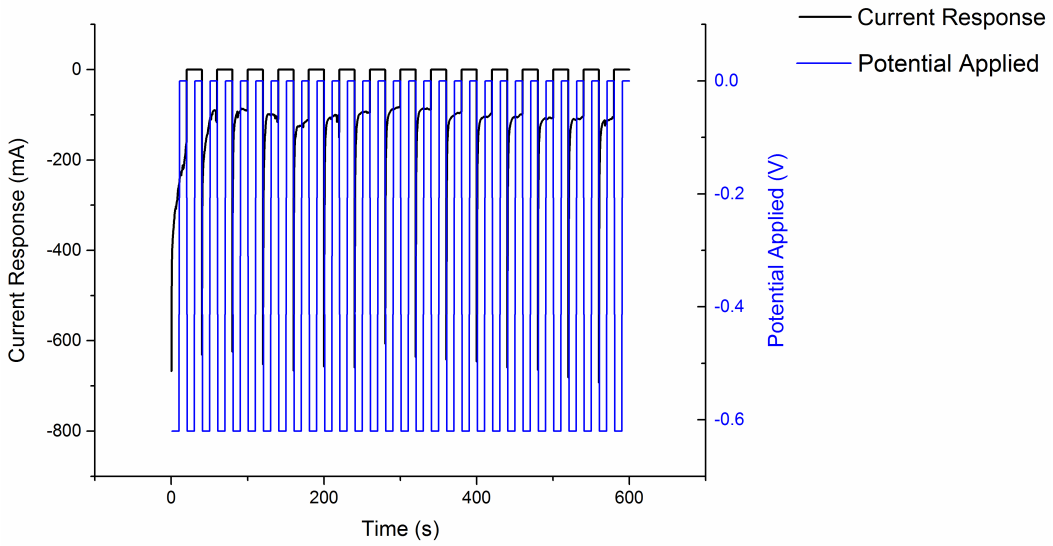

Fig. 3.4: A graph showing the pulsed chronoamperometry technique being utilized. A concentration of lead (II) chloride is present in the salt leading to Pb being plated onto a steel working electrode. The potential applied (blue) is pulsed at a potential of -0.62V, with respect to the Ag|AgCl reference electrode, for ten seconds and then OCP is maintained for 10 seconds. The current response is shown in black

Moreover, pulsed chronoamperometry may be employed as a technique for producing smooth deposits [60]. By pulsing the potential from OCV to a defined cell voltage, adherent and less dendritic deposits may be formed. Figure 3.4 is a graph depicting the pulsed technique being utilized. This process has been successfully implemented to understand the nucleation and growth of chromium electroplating in LKE [60].

Chronoamperometry is particularly useful for this work. Once the redox potentials have been deduced, it will be possible to understand the kinetics of the electrochemical reaction by holding the cell at the desired voltage. For example, if a reduction process was discovered at a potential of -1.5 V *vs.* Ag|Ag^{+}, one could then polarise the cell at this voltage for a period of time to study reaction kinetics. The current passed will slowly decay to, or close to, zero once the electrochemical reaction has completed. Integrating the area under the curve will allow one to

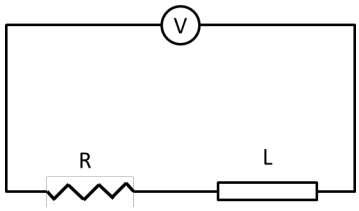

Fig. 3.5: Electric circuit with resistance and inductance

deduce the amount of coulombs required to complete reduction at a given current density.

3.1.4 Electrical Impedance Spectroscopy

Electrical impedance spectroscopy (EIS), also known as frequency response analysis, is an AC technique that extends basic concepts of resistance in electric currents. The main difference between resistance and impedance is the latter contains both magnitude and phase, whereas the former only contains magnitude. Therefore, impedance can be described as the complex ratio of voltage to current. One must note that in DC circuits, there is no sinusoidal effect from current or voltage and so the impedance and resistance are equal.

EIS was initially applied to determine the double layer capacitance of electrodes and has since become increasingly popular as an electrochemical diagnostic tool [99, 100]. EIS is a technique whereby an AC current (usually of low amplitude) is perturbed over a constant DC current. The frequency of this perturbation is changed and is usually swept from a high frequency to a low frequency. The high frequency perturbations usually help resolve phenomena that occur quickly within the system (such as charge transfer) whereas the low frequencies help describe those that are limiting (such as diffusion of ions).

Consider a simple electric circuit containing a resistance, r, an inductance, L, and an applied voltage of $\upsilon(t) = V_m e^{j\omega t}$, as shown in Figure 3.5 [101]. Kirchoff's law for this closed loop is:

$$r\,i(t) + L\frac{di(t)}{dt} = V_m e^{j\omega t} \tag{3.6}$$

This first order linear differential equation has a specific solution of the form $i(t) = Ke^{j\omega t}$. Substituting this solution in;

$$rKe^{j\omega t} + j\omega LKe^{j\omega t} = V_m e^{j\omega t} \tag{3.7}$$

Impedance, Z, is defined as the ratio of voltage to current:

$$Z = \frac{rKe^{j\omega t} + j\omega LKe^{j\omega t}}{Ke^{j\omega t}} = r + j\omega L \tag{3.8}$$

If a capacitance is considered instead of an inductance then the impedance is:

$$Z = r - j\left(\frac{1}{\omega C}\right) \tag{3.9}$$

Inspecting Equations 3.8 and 3.9, one can identify real and imaginary parts to the equations. It can therefore be concluded that the real resistance of impedance (which has no phase associated with it) is the real part of the solution whereas the capacitance and/or inductance contribute to the imaginary part of the solution. EIS, therefore, allows the study of the effects of phase changes on the electric circuit.

In conclusion, electrochemical impedance spectroscopy is an AC electrochemical technique. The basis of this technique is to perturb an AC potential/current on top of a stable DC potential/current. The benefit of using EIS is that an analogous circuit can be fitted to the data. This provides information such as electrolyte resistance and double layer capacitance which is fundamental to the electrochemical behaviour of electrodes. There is some literature on EIS for *pyroelectrochemical* applications ([102-104]) but there is substantially more literature on the application of EIS on fuel cells and batteries [105-109].

3.2 Tomography Techniques

The microstructure of the electrode may have a substantial effect on the overall performance of the electrode. It is also known that the local activity of pO^{2-} within the electrode may have an effect on the reduction potential. A highly tortuous microstructure could therefore impede the diffusion of O^{2-} ions out of the bulk electrode, causing a change in the local activity of oxygen anions and, therefore, the pO^{2-}.

However, as the microstructure of the electrode is inherently a three dimensional characteristic, it must be studied in three dimensions [110]. Two dimensional methods may be used to study phenomena such as the mean linear intercept which, in turn, may be used to estimate the average grain size of particles in the microstructure. However, this can only be done under certain assumptions [111]. By employing three dimensional techniques, these phenomena may be calculated without any bias or assumptions which could lead to an increased performance of predictive modelling tools.

There are many different tools and techniques available to characterise the microstructure of electrodes. However, it is important to note that there is a trade off between the volume of the sample that can be analysed and the resolution of the tool/technique, as summarised in Figure 2.7 in Section 2.3. The two main techniques that have been identified for this work are focused ion beam tomography and X-ray computed tomography.

3.2.1 Focused Ion Beam Tomography

Focused ion beam (FIB) tomography is a technique that combines the milling capabilities of a FIB and the imaging capabilities of a scanning electron microscope (SEM). The FIB is used to remove small layers of material whilst the SEM records images after each layer has been removed. These images are then combined into

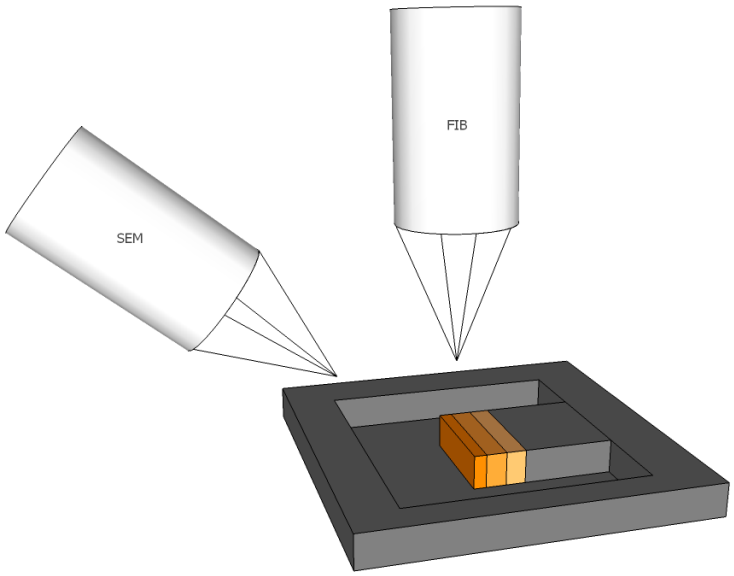

Fig. 3.6: A schematic depicting the FIB Tomography technique: The FIB is used to mill away sections (shown as shades of orange) whilst the SEM images the surface. These images are then stacked together to reconstruct the sample volume in three dimensions.

a stack of images and can then be reconstructed into a 3D representation of the volume.

A FIB is composed of an ion source, usually gallium, which is accelerated and focused onto the sample via electrostatic lenses. The gallium ions are able to sputter material from the sample, allowing the sample to be milled. When a FIB is combined with a SEM the sample may be milled via the FIB and sequential images are taken by the SEM via an alternating milling/imaging. The SEM is held at a constant, known, angle to the FIB (usually 45-55°) which is normal to the cross section of the sample. This combination of FIB and SEM to reconstruct 3D volumes is commonly known as "slice and view". Using algorithms, the images may be concatenated to render a 3-dimensional image of the sample from the collection of 2-dimensional images. Due to the milling nature of the FIB the sample is destroyed during analysis. Figure 3.6 is a schematic of the technology.

Because the volume reconstruction is derived by stacking sequential 2D SEM

micrographs, the resolution of the final reconstruction is a function of the SEM's specifications. Although describing the effect of the SEM specifications is beyond the scope of this report, it is important to understand that parameters such as the acceleration voltage, magnification and scanning speed all can have a huge effect on the final resolution of the sample. Moreover, the resolution is also a function of the FIB as the voxel size is define by parameters associated with both the SEM and FIB. The SEM will define the x and y dimensions, whereas the z dimension is define by the FIB; that is, the thickness of sample that is milled away during each step will deduce the z voxel dimension [112].

A Carl Zeiss XB1540 "Cross-Beam" focussed-ion-beam microscope was used for FIB tomography reconstructions. Typically, the FIB was operated with an acceleration voltage of 30 kV and milling currents were between 5-20 nA. For SEM imaging, acceleration voltages ranging from 1-30 kV were used. Experimental set-up produced a voxel size of, typically, 80 nm^3 to be achieved.

3.2.2 X-Ray Computed Tomography

X-ray computed tomography (CT) is another tomographic technique used to reconstruct a three dimensional reconstruction of a sample. X-ray CT directs X-rays towards the sample which produces a two dimensional radiograph of the sample. This is repeated a number of times as the sample is rotated along a single axis. For medical applications, the X-ray source and detector rotate around the sample allowing for the measurement at different angles. For material applications, another configuration is typically used whereby the detector and X-ray source are static and the sample rotates, as shown in Figure 3.7. Once the measurements have been taken, algorithms are then used to reconstruct a three dimensional image. The great advantage that X-ray CT has over FIB tomography is the fact that it is a non-destructive technique. That is, the sample is able to be used again whereas the use of FIB tomography destroys the sample. This advantage also paves the way for

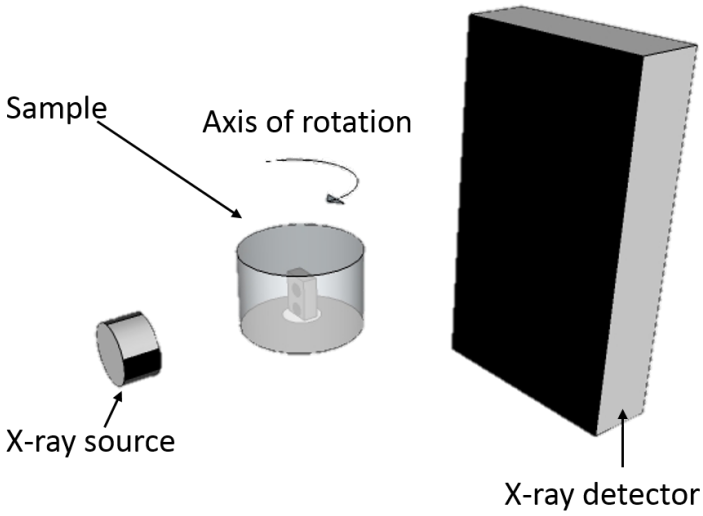

Fig. 3.7: X-Ray CT Scanner

the possibility of *in situ* tomography, enabling studies of microstructural evolution.

Although this technique is non-destructive, the resolution is typically not as good as that of FIB tomography. Also, artefacts are very typical in X-ray CT reconstructions. These artefacts (such as streaks and contrast effects) are usually as a result of beam hardening and reflections/refractions of the photon beam during measurement acquisition.

For X-ray CT measurements taken for the work of this thesis, a Nikon XTH225 ST laboratory scanning system was used, which allows for a maximum resolution of 3 µm. A photon energy of 120 kV was used with a 0.1 mm tin filter. This filter was applied to reduce beam hardening effects. This set-up resulted in MCEs measuring *ca.* 5 x 8 x 0.5 mm (W x L x D) to be reconstructed.

3.2.3 Microstructural Characterisation Techniques

After the tomography of the electrodes has been carried out, the output data will typically be an image sequence or ortho-slices of the sample volume. Depending on the technique that has been used to acquire the data, the image sequence may need to be cropped and filtered in three dimensions prior to full reconstruction.

Figure 3.8 is a diagrammatic representation of the algorithm adopted in this work to crop, align and filter images sequences acquired from FIB tomography prior to microstructural reconstruction. This is important as it allows for the removal of any artefacts that may appear during production of the image sequence. Figure 3.8(a) shows an example of an electrode during milling with the FIB. Firstly, the face of interest is cropped and is shown in (b). This is done for all images and then aligned with one another. The next step is to convert the images into a binary image to allow for segmentation of the pore phase and solid phase. Figure 3.8(e) shows the pixel count histogram of the cropped image and shows that there is not a great peak separation between the pore (dark) and solid (light) phases. Therefore, filtering processes are required in order to accentuate this difference. In this example, an adaptive histogram equalisation filter has been performed in three dimensions to produce the image in Figure 3.8(c). The pixel count histogram for this image is shown in Figure 3.8(f) which now shows a very good peak separation. The minimum pixel count between these two histogram peaks is then used as the threshold to convert the image into a black and white image; that is, greyscale pixels with a value equal to or higher than the threshold value are assigned a value of unity in the binary image whereas those below are assigned to zero. This produces the binary image shown in in Figure 3.8(d). This image will then be filtered using erosion and dilation methods to remove the "salt and pepper" noise from the image, if necessary.

Once this has been achieved, the microstructure is then reconstructed in three dimensions using the Avizo Fire 8 software package. This allows for easy phase segmentation of each of the phases and allows for precise microstructural information to be extracted.

The tortuosity of microstructures is one specific characteristic that may be defined in a number of forms. Firstly, the geometric tortuosity may be defined as the ratio of the shortest tortuous pathway length over the length of the microstructure [113]. Also, the tortuosity may also be extracted from the ratio of the macroho-

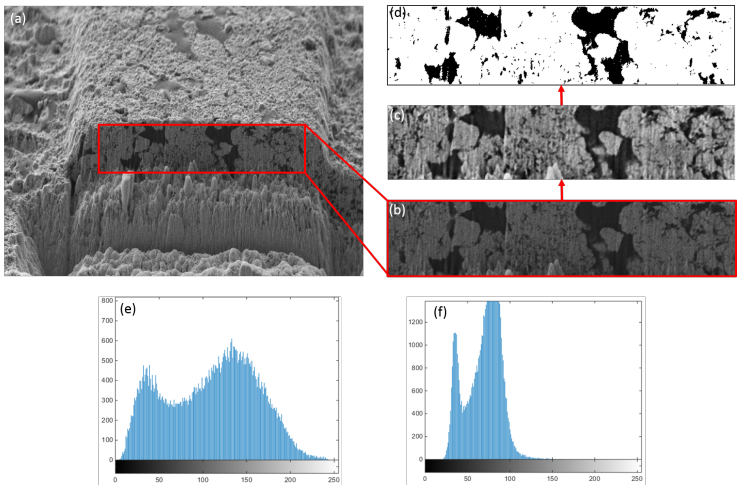

Fig. 3.8: Shows (a) the raw data image which is then (b) cropped and aligned with the rest of the sequence, (c) filtered to accentuate the contrast difference between the solid and pore phase and then (d) binarised. Pixel count histograms are shown for (e) the cropped image and (f) the filtered image, to show the effect of the filtering.

mogeneously defined heat flux through a control volume to the average heat flux within the pore phase sample volume [79, 114]. This methodology will be adapted in the work of this thesis to gain an insight into the tortuosity of the pore phase of the electrodes.

Firstly, a surface mesh was created in Avizo Fire 8 and imported into the Star-CCM+ computational fluid dynamics software package. A volume mesh is then created to enable modelling of the heat flux (which is analogous to mass flux) through the pore phase. This is then to be compared to the heat flux through a control volume of equal dimensions (a sold box of equal x, y and z dimensions to that of the pore phase). The tortuosities in each direction (τ_x, τ_y and τ_z) may be calculated by modelling the heat flux through the surfaces in the required axis and keeping all other surfaces adiabatic. The tortuosities may then be extracted by the application of Equation 3.10

$$\tau = \varepsilon \frac{Q_{CV}}{Q_{PORE}} \tag{3.10}$$

Where τ is the tortuosigy, ε is the porosity, Q_{CV} is the flux of the control volume and Q_{PORE} is the flux of the pore phase. For derivation of this equation, the reader is referred to [114]. By applying a heat gradient from one surface to the opposite direction while keeping all other surfaces adiabatic, the heat flux may be determined for that coordinate system. Therefore, tortuosities in the x,y and z directions may all be modelled and used to extract the tortuosity of the pore phase in those directions.

3.3 Diffraction Techniques

3.3.1 X-Ray Diffraction

Chemical identification is an extremely important tool and may be combined with electrochemical characterisation techniques to provide extremely robust evidence of electrochemical processes. One of the most important aspects of characterisation is phase identification, which can be achieved using X-ray diffraction (XRD). The basis of XRD is that electromagnetic waves of similar size to the crystal structure (*i.e.* X-rays) may be diffracted by a crystal structure. In 1912 Bragg offered a mathematical expression to denote the conditions necessary for diffraction to occur, known as Bragg's law:

$$\eta\lambda = 2dsin\theta \tag{3.11}$$

where n is a positive integer, λ is the wavelength of the incident X-ray, d is the interplanar distance and ϑ is the diffraction angle. Powder diffraction - a common X-ray diffraction technique - makes use of monochromatic X-rays of known wavelength. The angle at which the incident X-rays are diffracted is measured, and by using Bragg's law, it is possible to derive the crystal spacing of the sample.

An X-ray diffraction spectrometer works by directing X-rays at a known angle to the sample. The diffracted X-rays are detected by an ionizing chamber. Both the X-ray source and ionisation chamber are capable of moving in order to change

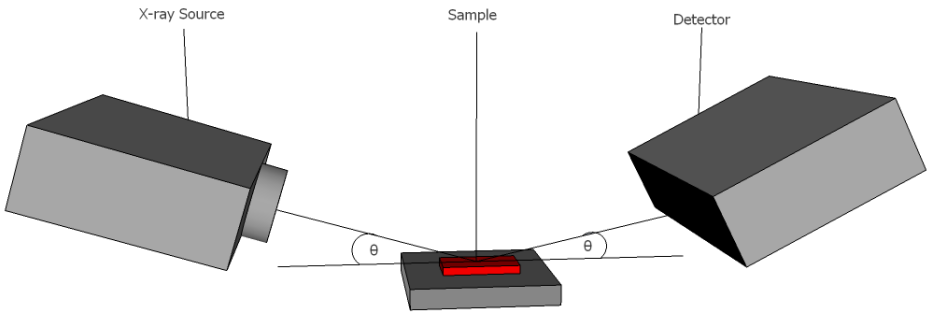

Fig. 3.9: X-ray Diffraction Spectrometer

the scattering angle, ϑ. A schematic of the X-ray spectrometer is shown in Figure 3.9. The resulting dataset of XRD are diffraction peaks or Bragg peaks; typically, a graph of intensity (arbitrary units) versus twice the diffraction angle, 2ϑ. The spectrometry data obtained can then be compared to a database to deduce the composition and or crystal structure of the sample [115-119].

For the purposes of an example, X-ray diffraction has been used to analyse a metallic tungsten rod. A sample of commercially available tungsten was analysed using XRD. Figure 3.10 shows the spectra that has been refined using Rietveld refinement (a theoretical line profile fitting of the spectra based on a least squares approach, for more information see [120]) . The different peaks have been identified and are attributed to the different crystal spacings.

Visual inspection of Figure 3.10 confirms no contamination is present within the tungsten rod as all diffraction peaks have been identified and are comparable to database spectra [121, 122].

To conclude, X-ray diffraction is an extremely useful tool in phase identification of chemicals. It allows for rapid phase identification and is a non-destructive technique. By measuring the scattering angle and the intensity of these diffracted X-rays (of a known wavelength) one is able to deduce the three dimensional structure of the crystal. This is extremely important as it is able to deduce whether samples possess contaminants and to infer their crystal structure.

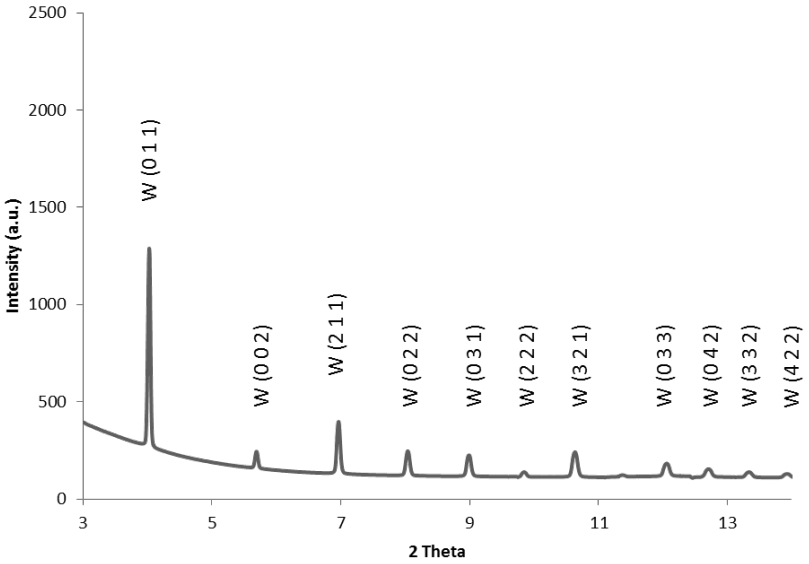

Fig. 3.10: XRD of a Tungsten rod taken at Diamond Light Source. Due to the high flux, there is an extremely good signal to noise ratio. All planes of tungsten have been fitted using Rietveld refinement.

3.3.2 *In-Situ* Synchrotron Diffraction Techniques

Synchrotron radiation is an extremely powerful tool which can provide an insight into electrochemical pathways *in situ*. The major advantage of gaining phase identification *in situ* is due to the fact that there is no risk of contaminating or changing the phase of the sample when preparing for *ex situ* analysis. Within the work of this thesis, X-ray synchrotron diffraction and neutron diffraction have been utilized. A brief description of these techniques is highlighted below.

3.3.2.1 X-ray Synchrotron Radiation

When electrons experience acceleration they emit electromagnetic radiation. When the electrons are accelerated radially, they produce synchrotron radiation in the form of high energy X-rays. This synchrotron radiation can be tailored to obtain the desired electromagnetic wavelength or energy. The type of acceleration that electrons experience can be classified into two main types of acceleration device;

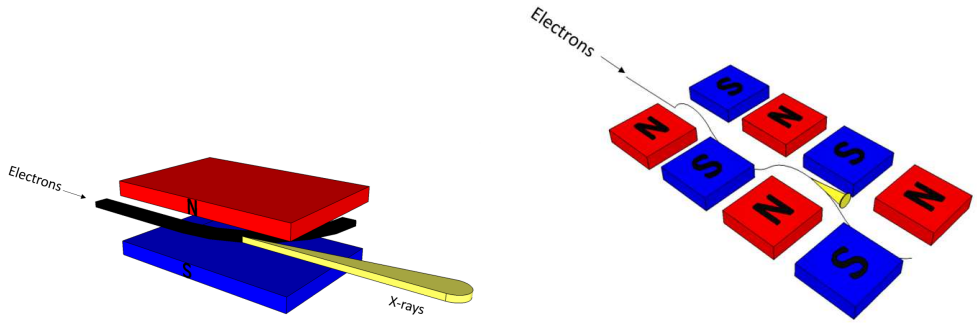

Fig. 3.11: Synchrotron radiation created by (a) bending magnets and (b) undulators

bending magnets and insertion devices. Bending magnets typically provide a broad range of electromagnetic wave energies which is also known as a white beam. Insertion devices may provide a electromagnetic waves of specific flux. This is done by passing the electrons through a periodic magnetic structure, causing the electrons to wiggle a specific number of times with a certain frequency. The two types of acceleration are shown schematically in Figure 3.11.

Once the X-rays have been emitted, they go through a series of optics to collimate and focus the beam. One of the most important optics can be regarded as the monochromator which allows only X-rays of certain energies to be passed. The monochromator works on the basis of Bragg's law. By determining the frequency of X-rays required, the angle at which the monochromator sits (which has a well defined d-spacing) can be manipulated to reflect certain wavelengths. It should be noted that if no monochromator is used then a white beam is produced.

Electron synchrotron radiation can be applied to electrochemical cells by looking at the X-ray diffraction *in situ*, such as the work done by Bhagat [21]. However, for heavy metals, such as tungsten and uranium, there is a possible problem as X-ray attenuation is significant. Figure 3.12 shows the attenuation length of X-rays of varying energies for uranium [123]. From this, one can see that the attenuation length of uranium is *ca.* 12.5 µm at 30 keV. This could prove difficult in gaining

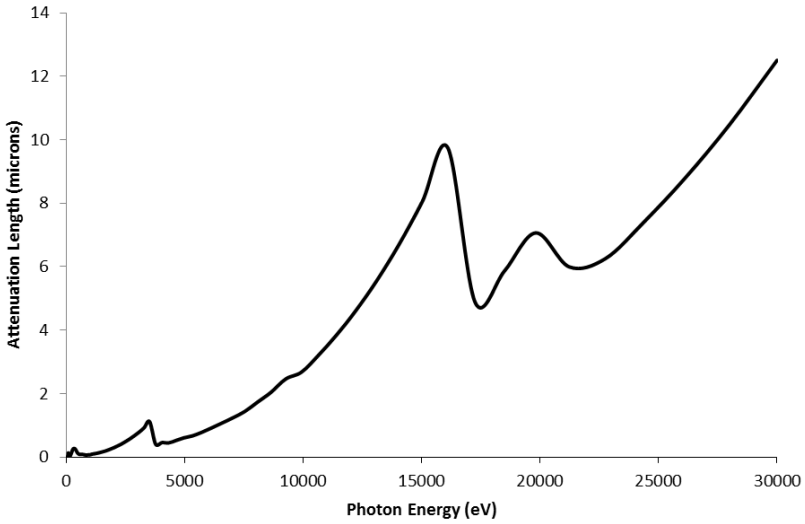

Fig. 3.12: Attenuation length of uranium, adapted from [115]

a good signal to noise ratio, although some synchrotrons allow for higher energy photons (say 150 keV).

3.3.2.2 Neutron Synchrotron Radiation

Neutron radiation is another type of synchrotron radiation which is produced via a proton accelerator. Unlike X-rays, which interact with the electron cloud surrounding the atom, neutrons interact directly with the nuclei of atoms. Neutrons are produced by accelerating negatively charged protons via a linear accelerator and synchrotron ring. After leaving the synchrotron ring, the protons are driven towards a tungsten target. Bombardment by these protons drives neutrons from the nuclei of the tungsten target, which are then directed to different instruments. One of these instruments can be a neutron diffractometer.

The problem highlighted in Section 3.3.2.1 can be ameliorated to an extent with neutron diffraction. The attenuation of neutrons by heavy metals is not as significant to that of X-rays. Literature values show that uranium and tungsten have an absorption cross section of 7.57 and 18.3 barns respectively (for 2200m/s

neutrons). This is comparable to known attenuators of neutrons, such as lithium, which has an absorption cross section of 70.5 barns [124].

These two synchrotron techniques have the potential to provide *in situ* diffraction data, permitting the electrochemical reaction pathway to be followed as the reaction happens. This has the great advantage of removing potential contaminations that may arise in the *ex situ* analysis preparation procedures.

3.4 Summary of Methodologies

Throughout this chapter, the scientific methods and techniques have been presented with examples of their use in order to define a clear outset to the acquisition of the scientific results that are presented in proceeding chapters of this thesis.

As discussed in Section 3.1, the electrochemical techniques used in this thesis range from potential sweep methods to electrical impedance spectroscopy. By utilizing a range of techniques, many different electrochemical effects may be investigated in order to provide in-depth electrochemical studies.

In addition, by coupling the chemical characterisation with microstructural investigations, presented in sections 3.2 and 3.3 to the electrochemistry, a full analysis of the electrochemical reduction and any chemical or structural effects may be understood.

The next chapter of this thesis - experimental rig design - works in tandem with this chapter to provide a full definition of the experimental techniques and methods used. It is perceived that the combination of these two chapters will allow for full reproducibility of the results that are presented in Chapters V-VIII.

Chapter IV. Experimental Rig Design

4 Experimental Rig Design

This section further expands on the methods used within this work and, in particular, defines the experimental set-ups used to produce the experimental results presented in Chapters VI-VIII. The previous chapter is to be used as a basis of understanding of the different techniques, whereas this chapter uses those methods to show the evolution of the experimental design and how this design allows for the control of process variables. Specifically, it denotes the experimental conditions and the equipment used throughout the studies that underline this thesis.

Reproduction of scientific results is largely affected by the experimental set-up chosen and so, therefore, the experimental rig design is expanded upon largely within this chapter. It is beyond the scope of this thesis to outline an exhaustive list of conditions that require adequate controlling (in terms of the electrochemistry, molten salt environment) but, instead, the reader is directed to the following reference, if necessary [125]. This chapter will describe the general experimental set-ups used to study the electrochemical reduction of uranium dioxide to uranium in LKE. It should be noted that all potentials reported within this thesis are with respect to the Ag|AgCl reference electrode, unless otherwise stated. For more information, the reader is directed to section 4.6.

4.1 Laboratory Reaction Vessel

The reaction vessel for the work of this thesis has undergone a series of iterations in order to optimise safety, integrity and optical visibility. Heavily oxidising and corrosive environments can exist within a molten salt cell and these must be accounted for during the design [126, 127]. The cell has incorporated argon inlet and outlet streams to reduce the oxidising environment and reference electrodes have

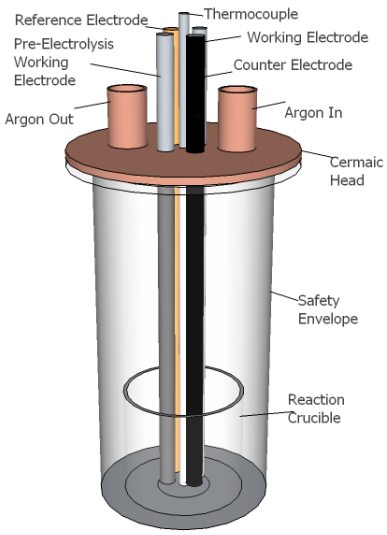

Fig. 4.1: Showing the Electrochemical Cell. The molten salt is contained within the Reaction Crucible which sits inside the Safety Envelope. The electrodes are held into the cell head using Suba-Seals. The cell head incorporates gas in/out line and is fixed to the safety envelope via a metallic clamp.

been designed in order to minimise ionic resistance between itself and the working electrode.

4.1.1 Electrochemical cell

The electrochemical cell is composed of two glass vessels; a reaction crucible and a safety envelope. The safety envelope is incorporated to prevent the salt from leaking from the electrochemical cell into the experimental environment due to a breakage. A vertical, tall form, flat bottom Pyrex glass cylinder (GPE Scientific) was custom built to act as the safety envelope. The top of the cylinder contains a flange to allow for an air tight seal managed by the use of a ceramic vessel head (see below). The actual reaction vessel is a smaller Pyrex tall form beaker which sits inside the safety envelope. A schematic of the electrochemical cell vessel can be seen in Figure 4.1.

4.1.2 Temperature control

4.1.2.1 Optical Access Furnace

Due to the relatively low melting point of the LiCl-KCl eutectic (compared to other common molten salts) a furnace was conceived and built in order to provide optical access to the LKE electrolyte. This furnace set-up has the main advantage of allowing identification of contamination of the salt and the state of the electrodes in the electrochemical cell both easily and rapidly. The main disadvantage of this set-up is the longer time required to reach the reaction temperature.

The temperature is maintained via an equimolar sodium nitrate – potassium nitrate salt bath, heated by an in-house custom built nichrome wire immersion heater which is comprised of a 0.5 mm diameter, 4.5 m long coil of nichrome wire contained within a custom built silica glass sheath. The salt bath is contained within a 5 L (180 mm O.D) heavy duty Pyrex glass beaker (Scientific Lab Supplies) to allow optical visibility. The temperature of the system is monitored via a thermocouple which is immersed in the reaction vessel. The power of the immersion heater is controlled via a variable AC controller (variac) which is connected to a mains power supply. A schematic of the temperature control equipment can be seen in Figure 4.2 and a photograph of the electrochemical cell inside the thermostatic bath can be seen in Figure 4.3.

Due to the high thermal conductivity of the nitrate salt, the temperature of the reaction vessel is kept relatively constant when disturbances occur. This is shown by Figure 4.4. The temperature gradually increases in an hour to the melting point of the eutectic; 352°C. after which the temperature remains constant due to the latent heat of melting. After approximately one hour, the salt has completely melted and the temperature of the salt begins to increase. The salt reaches the working temperature (in this instance) of 410°C where it remains for the duration of experimentation. After a total time of approximately 4.5 hours, the cell is removed

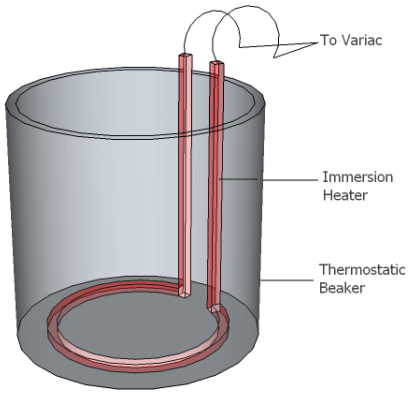

Fig. 4.2: Shows the optical access furnace. It is comprised of custom built immersion heater which sits in the thermostatic salt bath. Once molten the electrochemical cell is lowered into the furnace.

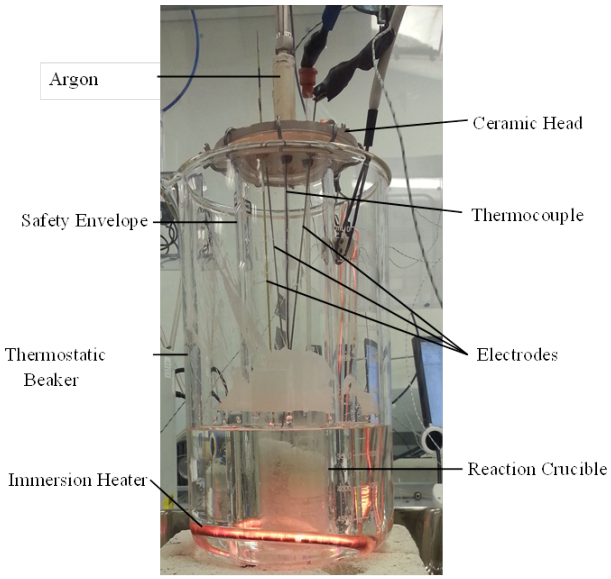

Fig. 4.3: Shows the electrochemical cell inside the optical access furnace. Note, the LKE salt is not molten to aid visualisation

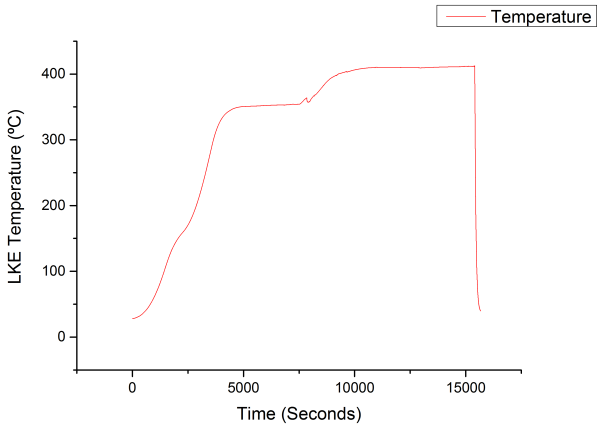

Fig. 4.4: A graph showing the temperature of the eutectic molten salt inside the optical access furnace. There is an initial temperature increase until 352°C; the melting point. The temperature remains stable until all of the salt is molten. After which the temperature increases to 410°C at which it remains constant until the reaction vessel is removed from the furnace.

from the furnace. At this point, the thermocouple is removed from the melt itself to avoid the thermocouple becoming frozen into the salt.

4.1.2.2 Lenton Vertical Tube Furnace

An alternative furnace was also available to provide heat to the electrochemical cell. The furnace is a horizontal split-tube furnace (CSC 12/90/300V Furnace, Lenton). The furnace was custom built to fit the electrochemical cell and allowed faster heating to the electrochemical cell. This furnace was also able to provide a stable temperature as seen in Figure 4.5. From this plot, one can draw many similarities to Figure 4.4. Both images show that the salt undergoes an initial increase in temperature until the melting point. Once all salt has become molten, the temperature of the molten salt increases to the working temperature of 400°C. Once at the working temperature, there is only slight deviation in the temperature (1°C) which is deemed negligible.

Two furnace set-ups have been employed throughout the experimentation of

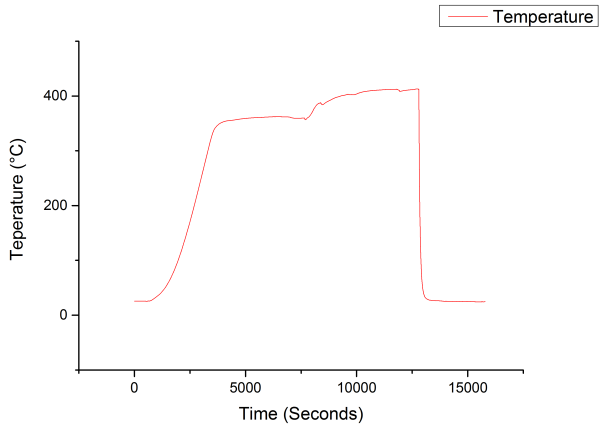

Fig. 4.5: A plot of temperature of the LKE salt versus time during heating in the Lenton furnace. There is an initial temperature increase until 352°C; the melting point. The temperature remains stable until all of the salt is molten. After which the temperature increases to 400°C (the working temperature) at which it remains constant until the reaction vessel is removed from the furnace.

this thesis. An optically accessible furnace was conceived and built to facilitate the identification of any issues with the molten salt, such as contamination. Figures 4.2 and 4.4 show the inherent stability of the temperature of the molten salt inside each furnace set up. Only small deviations (approximately 1°C) occur when the fused salt is at working temperatures in excess of 400°C which is deemed negligible.

4.1.3 Cell Head

The cell head is an airtight fitting which allows the electrodes to penetrate into the cell. Phyrophillte (Aluminium Silicate) (Ceramic Substrates and Components Ltd) was chosen as the cell head as it is has the benefits of being machinable before sintering and it becomes thermally insulating after sintering. A number of holes were drilled into the ceramic prior to sintering, depending on the experiment. Table 4.1 depicts which holes were drilled for each particular experimental set-up.

Once drilled, the ceramic is then sintered at a ramp rate of 250°C hr^{-1} to 1000°C and is then held for one hour. Electrodes and thermocouples are held in the ceramic

Holes drilled for	Electrochemical Characterisation	Effect of pO^{2-} studies	UNH decomposition (see Chapter VI)
Argon In/Out	✓	✓	✓
Pre-electrolysis WE	✓	✓	✗
Working Electrode	✓	✓	✗
Counter Electrode	✓	✓	✗
Reference Electrode	✓	✓	✗
Thermocouple	✓	✓	✓
pO^{2-} indicator electrode	✗	✓	✗

Tab. 4.1: Description of holes drilled for use of different experimentation

head using size 13 Suba-Seals (Sigma-Aldrich) which are capable of maintaining the airtight environment. A PTFE gasket (Sci-Labware) is used to facilitate a good seal between glass flange and ceramic head. The ceramic head is fixed to the safety envelope using a metallic clip (Sci-Labware). The gas inlet and outlet connections were also fitted with check valves to ensure that the airtight environment was not compromised during attachment of the purge gas system.

4.1.4 Typical Laboratory Experimental Set-up

All glassware was cleaned with hot soapy water and Decon 90 (Decon Laboratories Ltd) and then rinsed with deionised water and acetone. All equipment was administered into the MBraun glove box (see Section 4.8) and the cell was assembled using the following procedure:

1. The salts were weighed using scales with an accuracy of ±50 μg. Typically a mass total of 100 g LKE was used.

2. The salts were mixed together by shaking them together in a sealed container for 60 seconds.

3. The salt mixture was poured into the reaction crucible.

4. The reaction crucible was inserted into the safety envelope.

5. The cell head (containing all electrodes) was affixed to the safety envelope with a metal clamp. PTFE gaskets are also used to ensure a gas-tight environment.

6. The air-tight cell was removed from the MBraun glove box and inserted into the furnace.

7. Gas lines were purged and attached to the electrochemical cell.

8. Once the working temperature was achieved (400-450°C) pre-electrolysis was performed for 2 hours.

9. After pre-electrolysis had terminated, the pre-electrolysis working electrode (Mo or W rod, 1-3 mm Ø) was removed and the UO_2 working electrode was inserted into the molten salt and left for 10-30 minutes to stabilize.

10. Electrochemical measurements were taken using an IVIUMStat potentiostat / galvanostat (IVIUM Technologies).

4.2 *In Situ* Diffraction Reaction Vessel

A novel electrochemical cell has been designed for use with neutron and X-ray diffraction experiments. Considering neutron diffraction, lithium and chloride are both strong attenuators of neutrons. The nuclei of lithium are of a relatively similar size to that of a single neutron and hence posses a high absorption cross section. Considering X-ray diffraction, as X-rays interact with the electron cloud of atoms, the elements in the periodic table with a large number of electrons offer high attenuation to X-rays; for example, uranium. Because of this, the cell had been designed to ensure the path of the neutron is minimized through the LKE to increase the possibility of a high signal to noise ratio. The material of construction was also extremely important. The material would have to be able to withstand the molten

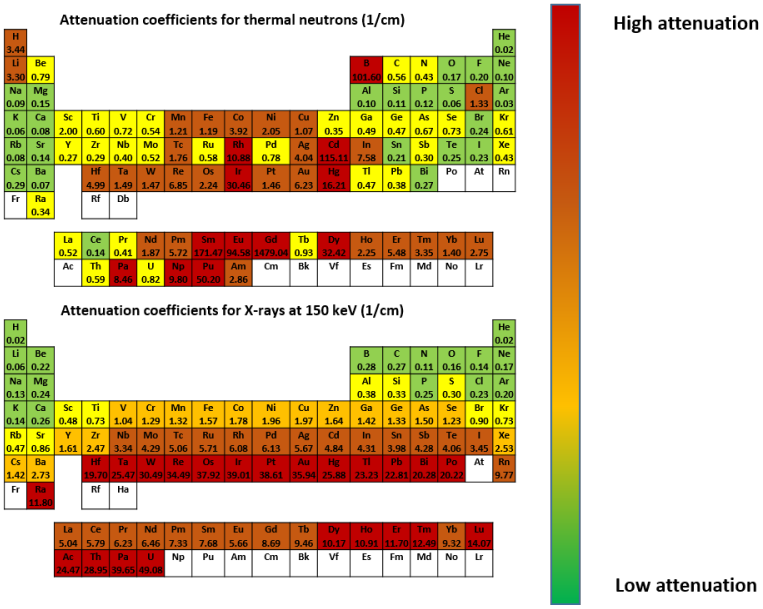

Fig. 4.6: Periodic table showing the attenuation lengths for the elements for both thermal neutrons (top) and X-rays (bottom). Adapted from [128]

salt environment, temperature and not be attenuating. Therefore, the cell was constructed from aluminium as this material may be considered relatively neutron and X-ray "transparent" For example, aluminium has an absorption cross section of 0.231 barns, compared to lithium which has an absorption cross section of 70.5 barns [124]. A summary of the attenuation lengths for the elements for both thermal neutrons and X-rays is provided in Figure 4.6 [128].

4.2.1 Electrochemical Cell

The electrochemical cell was manufactured from aluminium due to it's low attenuation to neutrons and X-rays. The cell also incorporates a "well" at the bottom of the cell where the working electrode is located. This is to reduce the beam path through the cell, thus, reducing attenuation and increasing the signal-to-noise ratio. The balance-of-apparatus components (counter electrode, reference electrode *etc.*) are contained within the main body of the vessel. A photograph of the electrochemical cell can be seen in Figure 4.7(a). On the flange of the cell, six holes were drilled

to allow for the cell head to be bolted on.

4.2.2 Cell Head

The cell head was manufactured from 316 stainless steel and incorporated many design aspects to optimise a number of attributes. Firstly, the material of construction - stainless steel - was chosen to due to its lower thermal conduction coefficient compared to aluminium. This would help keep the top of the cell cool and allow the introduction/removal of electrodes. Also, stainless steel is easy to weld and assisted in production time and cost. The cell head also incorporated a number of hollow, open-ended, cylinders which were welded on top of the head. These were included to help ensure the electrodes were held horizontally and also acted like heat transfer fins; again, aiding cooling of the electrodes. The cell head also incorporated Swagelok fittings to allow for gas to flow through the cell. Lastly, the cell head included 6 holes to allow for bolting onto the cell. A graphite gasket was also used to ensure a gas-tight fit. A photograph of the electrochemical cell head can be seen in Figure 4.7(b).

4.2.3 Heating Jacket

Heating was supplied to the electrochemical cell head via a custom built flexible ceramic pad heater. This is comprised of a high grade nichrome wire encapsulated inside aluminium oxide "beads" which allow for its flexibility. The heating pad and insulation was wrapped around the electrochemical cell body and secured into place with a number of jubilee clips. Power was provided via a 3-phase power supply which was controlled using a Eurotherm PID controller whose input was a K-type thermocouple which was immersed into the molten salt.

(a) (b)

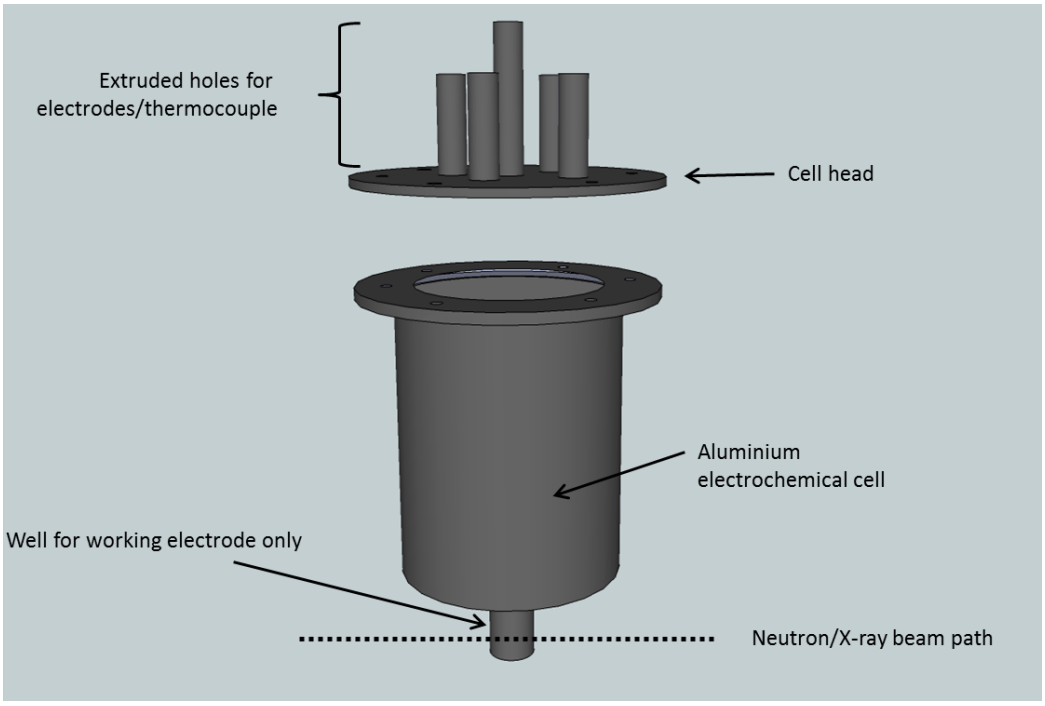

(c)

Fig. 4.7: (a) *In situ* diffraction cell body, (b) diffraction cell head and (c) an exploded schematic of the cell and cell head assembly

4.2.4 Experimental Set-up Of The Molten Salt Cell

The electrochemical cell was assembled inside an inert gas filled glove box which maintained an oxygen and moisture composition of <0.1 ppm. 300 g of dried LKE (see Section 4.4) was loaded into the electrochemical cell, along with the electrodes and thermocouple. Note, due to local rules within the synchrotron buildings, the uranium dioxide working electrode was unable to be loaded into the electrochemical cell inside the glove box and was required to be inserted into the cell on the beamline itself. All electrodes were secured to the cell head via silicone Suba-Seals (Sigma-Aldrich).

Check valves were incorporated into the cell head to ensure a flow of inert gas could pass through the cell during the experimentation and to ensure a gas tight environment during transportation from the glove box to the beam line. Once the electrochemical cell was secured onto the beamline sample stage, the source gas line (research grade argon for X-ray diffraction experiments and research grade helium for neutron diffraction experiments (<0.5 ppm H_2O & O_2)) was purged and connected to the electrochemical cell. The outlet gas was pumped through a "gas trap" to absorb any chlorine gas that may form during electrochemical measurements. The gas trap was comprised of a sequence of four Dreschel bottles: the first was empty to ensure no liquid flowed into the cell's gas outlet stream due to any back pressure; the second and third bottles contained NaOH solutions to absorb chlorine containing vapours from the cell and the last bottle was filled with de-ionised water.

The heating jacket was then secured to the electrochemical cell and connected to the PID-controlled power source. A layer of ceramic-based, flexible, furnace-grade insulation was also wrapped around the heating jacket. The insulation and heating jacket were fixed to the cell via a number of jubilee clips. The cell was heated at a ramp rate of 10°C min^{-1} from room temperature to a working temperature of 450°C. Once the electrolyte became molten and reached the working temperature,

pre-electrolysis was performed for 2 hours to remove any electro-active contaminants.

Once pre-electrolysis had terminated, the UO_2 metallic cavity electrode (see Section 4.3.1) working electrode was inserted into the cell. During this procedure, the inert gas flow rate was increased to help reduce the risk of oxygen and moisture entering the cell from the ambient atmosphere. The working electrode was placed into the well of the cell and connected to the potentiostat. The electrode was left for 30 minutes to stabilise in the molten salt before electrochemical measurements were taken.

4.2.5 *In Situ* X-Ray Diffraction Experimental Set-up

Energy Dispersive X-ray Diffraction (EDXD) measurements were taken on beam line I12 (JEEP) at Diamond Light Source in the UK. This diffraction technique differs from conventional, angle-dispersive, X-ray diffraction as the lattice plane distance – or d-spacing – is derived by determination of the wavelength of the diffracted polychromatic photons, as opposed to being derived from the diffraction angle of monochromatic photons [129]. The diffraction angle may be kept constant by the use of a collimator. As a direct result of using a collimator to define a constant Bragg angle, a lozenge shaped gauge volume in space is defined whereby only photons that are scattered within this volume will be detected by the detector. Placing the sample within this gauge volume has an advantage of being able to eliminate the signal from balance-of-apparatus components (the electrochemical cell, for example) and ensures that a high signal-to-noise ratio from the working electrode is collected. This is a useful advantage when using small samples, such as MCEs, which are on the sub-milligram range.

The sample stage allowed translations in three dimensions with a 10 μm resolution. This ensured that the cell could be aligned in each direction by remotely moving the stage; the MCE was aligned in the X and Y directions using an X-ray imaging detector (which was removed during EDXD measurements). Figure 4.8

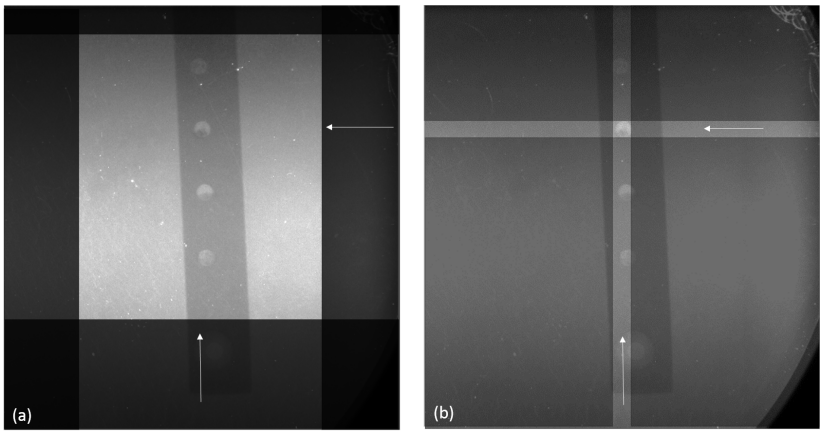

Fig. 4.8: X-ray images of the MCE in the well of the electrochemical cell showing X-Y alignment. (a) Shows the MCE with the slits open and (b) shows a UO_2 filled hole in the MCE aligned

shows X-ray images of a UO_2 filled MCE in the electrochemical cell. X-Y alignment was achieved by moving the X-ray slits over a UO_2 filled hole using live images. The slits created a 0.3 mm^2 square X-ray beam which helped to increase the signal to noise ratio of UO_2. For alignment in the Z-direction, it was necessary to move the MCE into the middle of the lozenge-shaped gauge volume. This was achieved by varying the stage's position in the Z direction and measuring the signal-to-noise ratio of UO_2.

During the experimentation, a 0.3 × 0.3 mm white X-Ray beam of energies ranging from 45 to 150 keV irradiated a single UO_2 filled cavity on the MCE working electrode, inside the electrochemical cell. EDXD data was collected with a cryogenically cooled 23-element, high-purity, germanium detector (Canberra Industries, Inc.), as shown in Figure 4.9(b). The 23 detector elements are spaced every 8.18°, allowing azimuthal angles from 0° to 180° to be covered. The EDXD data collection was synchronised with the electrochemical measurements using an exposure time of 60 seconds. The take-off angle of 4.5° is defined by the collimator; all other X-rays which are diffracted at angles not equal to 4.5° are not detected. The collected diffraction patterns over the 23 elements were then averaged to produce a powder

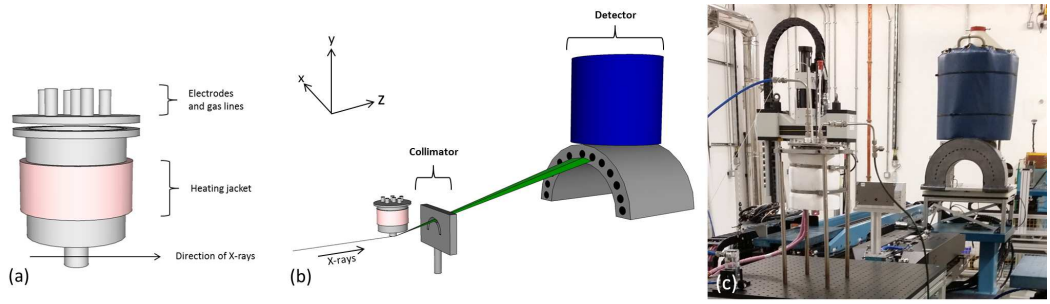

Fig. 4.9: Showing (a) the direction of X-rays and their positions relative to the electrochemical cell and (b) the experimental set-up on the I12 JEEP beamline at Diamond Light Source (c) is a photograph of the experimental set-up.

averaged diffraction pattern, improving the quality of the gathered data. The resulting EDXD data are plotted as a function of the photon energy of the diffracted X-rays, in contrast to powder X-ray diffraction data. These are obtained at a single wavelength and are plotted as a function of the scattering angle, 2-theta.

4.2.6 *In Situ* Neutron Diffraction Experimental Set-up

Neutron diffraction experimentation was done on the ENGIN-X beamline at the ISIS neutron source, UK. Neutron diffraction is similar technique to X-ray diffraction but it is able to provide complimentary data, due to the difference in the interaction of neutrons with nuclei compared to X-rays.

The electrochemical cell was bolted onto the sample stage via a custom built clamp-stand. The sample stage permitted movement of the cell in the X,Y and Z directions all with an accuracy of 5μm. Stage rotation was also permitted with an accuracy of movement of 0.002°. This stage movement allowed for sample alignment to the incident neutron beam. Coarse alignment was conducted with a theodolite which is located at ±45° to the incident beam. Fine alignment was done by moving the sample in the X, Y and Z directions and measuring the signal to noise ratio of the sample.

During experimentation, a 0.5 x 0.5 mm neutron beam irradiated the MCE

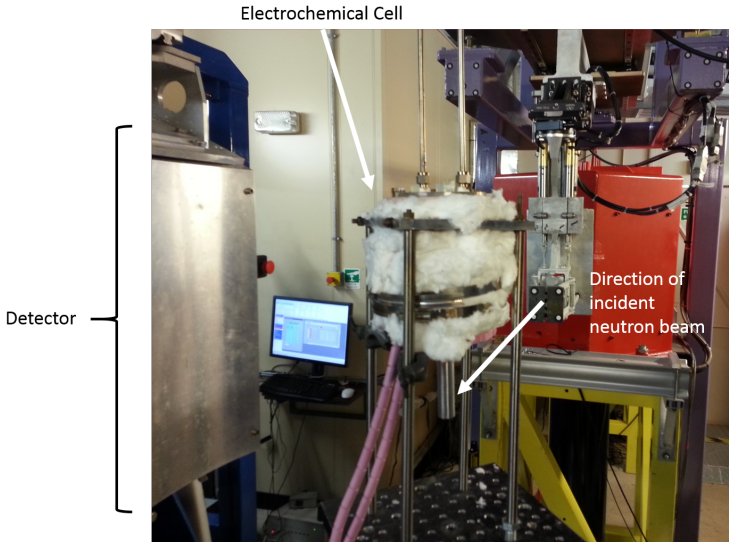

Fig. 4.10: Showing the experimental set-up of the *in situ* electrochemical cell on the ENGIN-X beam line at ISIS neutron source, UK.

working electrode and data was collected using two detector banks. The ENGIN-X detector set-up comprised of two diffraction detector banks which were located at horizontal diffraction angles of $\pm 90°$ to the incident neutron beam. These two detectors spanned 30° both horizontally and vertically. Each detector bank was comprised of 1200 ZnS/^{6}Li scintillator elements which are arranged in 5 units, stacked on top of one another (each unit is made of 240 horizontally stacked elements). This gives rise to a spatial resolution of 3 x 150mm (horizontal by vertical).

A photograph of the experimental set-up may be observed in Figure 4.10. Observation of Figure 4.10 shows the electrochemical cell which is bolted onto the sample stage (and covered with insulation). One of the two detector banks is visible on the far left of the photo.

4.3 Cathode

For experiments concerning the reduction of titanium dioxide to titanium and alloys (the FFC Cambridge process), the electrode is predominantly a pellet [17-22, 130-132]. The precursor is a (mixture of) metal oxide powder(s) which, typically,

are pressed between 50-100 MPa and then sintered at a temperature of 1100°C. This gives rise to a porous pellet of open porosity ca. 25-35%. However, due to the limited quantities of uranium dioxide powder available, the cathode design utilized within this thesis has been those which hold sub-milligrams of powder. Throughout this study, different forms of cathode have been prepared for the electrochemical reduction of uranium dioxide to uranium of which are expanded upon in the proceeding sub-sections.

It should be noted that the current collector assembly for all electrodes were cleaned via the same systematic procedure: Firstly, the electrode current collectors were dipped into *aqua regia* for up to two minutes. After which, they were then quickly transferred to a bath of deionized water to remove the acid. The current collectors were then cleaned with hot soapy water, rinsed with deionized water and then washed in acetone to remove water stains. The current collectors would then be ready for use.

4.3.1 Metallic Cavity Electrodes

A more recent development of electrodes (compared to pellets) used for studying the reduction of powders is the metallic cavity electrode (MCE). The MCE was first described by Qui *et al.* and was developed in order to study the reduction of powders [133]. The fundamental advantages of this electrode is that it permits the fundamental electrochemical study of powders with substantially less amount of powder required, compared to a pellet. The latter phenomenon is particularly important as relatively large amounts of powder may cause high current responses, which cause high ohmic drops; this is not ideal for potential controlled experiments. As a result, the MCE has been an electrode that features in many papers regarding the reduction of various powders in molten $CaCl_2$ [134-138].

In the experiments presented here, the MCEs were fabricated from 0.5mm thick foils of molybdenum. A number of holes with a diameter of 0.5 mm were drilled

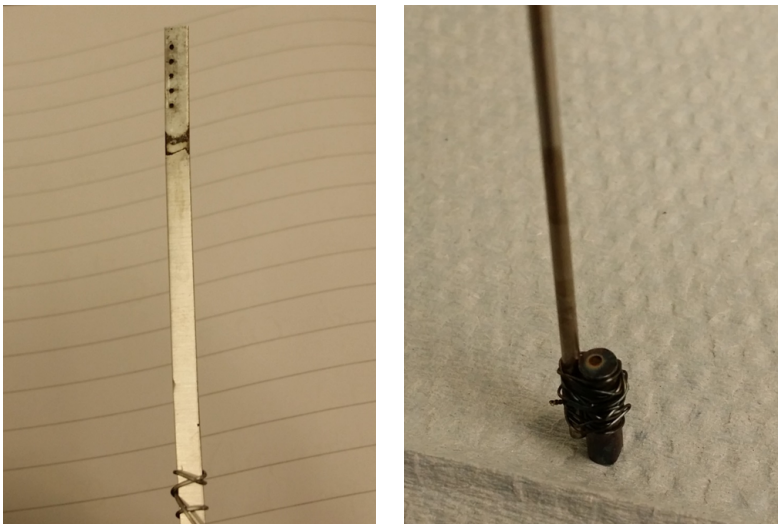

(a) (b)

Fig. 4.11: (a) A UO_2 packed MCE and (b) a UO_2 packed MBE

into the foils (see [133]). The foils with the holes drilled were then cut into strips with a width of *ca.* 4 mm by using a steel guillotine. Once the MCEs had been cut, they were washed with a mixture of Decon 90 and deionised water and dried. Afterwards, they were washed in acetone before being stored, ready for use.

The MCE foils were attached to a molybdenum rod current collector (3 mm Ø, 35 mm length) with 0.2 mm diameter molybdenum wire to ensure an all-molybdenum current collector system was employed. This allows the current response of blank MCEs (MCEs which have not been packed with powder) to be attributed to molybdenum only. Packing of the UO_2 powder was achieved by pressing the powder into the MCE between two optical microscope glass slides by hand. A pin (0.4mm diameter) was also used to push powder inside the MCEs to ensure a high packing of the powder. A 5-hole MCE packed with UO_2 powder can be seen in Figure 4.11 (a).

4.3.2 Micro-Bucket Electrodes

The main disadvantage of the MCE is the fact that powder tends to fall out from the holes during the electrochemical reduction, especially if the powder has a large

particle size distribution. The mechanical stability of packed, non-sintered, powders is low. This combined with a significant volume change during electrolysis in the packed powder could cause the structural integrity of the "pellet" to be compromised and hence result in the powder falling into the bulk electrolyte.

A novel type of micro electrode has been conceived in order to reduce the risk of this phenomena; the micro-bucket electrode (MBE). As the name suggests, the MBE can be pictured to be the shape of a bucket. The "bucket" is packed with powder and attached to a current collector. This arrangement reduces the risk of powder falling out as there is only one cross section open to the bulk salt.

The MBE is comprised of a 3 mm diameter metallic rod (molybdenum, tungsten, *etc.*) with an approximate length of 10 mm. A 0.8 mm diameter hole is then drilled into the circular cross section of the rod, approximately 2-3 mm deep. Powder can then be pressed into the cavity as in the MCE. The MBE is then attached to a molybdenum current collector with the face of the cavity pointing up. The main advantage of this cathode configuration is that the powder does not fall out of the electrode during electrochemical reduction. An image of an MBE can be seen in Figure 4.11 (b).

4.4 Electrolyte

One of the main advantages of using LKE is the absence of highly basic and acidic environments. However, hydrolytic decomposition can occur within the melt if residual moisture is not removed from the system. This hydrolytic decomposition occurs as the temperature of the system is raised and HCl is lost from the system, causing the melt to be contaminated with alkaline products [139]. This is a much greater problem when using LiCl due to its high deliquescent properties. It is therefore necessary to remove any residual moisture from the salts before the reaction temperature is reached. There are a couple of methods in the literature that describe methods of removing moisture [139, 140]. The latter, describes how the dehydration

of $LiCl.H_2O$ occurs and states that full dehydration of LiCl occurs via a two step reaction between 99-110 and 160-186°C. The measurements were carried out at low ramp rates (1-10°C) which resulted in a slow moisture removal process. Therefore, all salts procured for experimentation were dried under vacuum for 24 hours prior to use.

Commercially available anhydrous lithium chloride and potassium chloride (> 99.98%, Sigma Aldrich) were used for all experiments. During the drying procedure, the vacuum oven was first filled with argon gas prior to inserting the salts. Once the salts were loaded, the oven was subjected to a vacuum and re-filled with argon. This purge sequence was repeated 3 times whilst the oven ramped up to a working temperature of 175°C to ensure the salts did not absorb moisture from the oven's environment. Once the working temperature was achieved, the oven was subjected to a vacuum and left for at least 24 hours. After the vacuum drying was complete, the oven was left to cool under vacuum. Once room temperature was achieved, argon was administered into the vacuum oven. The salts were removed and gas-tight lids were affixed to the containers within seconds of opening the vacuum oven. The salts were then transferred to an argon filled glove box (boasting levels of O_2 and H_2O of <0.5ppm) for use or storage. The eutectic was made by mixing the two salts in a ratio of 41:59 mol/mol% LiCl:KCl [25] inside the glove box.

XRD was also used to identify any contamination that may be present in a sample of LKE that was dried using the technique described in above. Figure 4.12 contains the results of this analysis and it is clear that little or no contamination is present due to the high intensity of KCl (1) and LiCl (2) peaks within the data. A full Le Bail refinement was performed and the refined lattice parameters for LiCl and KCl were extracted to be 5.08854 Å and 6.22967 Å which match very closely to the literature data of 5.08 Å and 6.22 Å respectively [141, 142]. It is therefore understood that the drying of salts using the vacuum oven described is adequate to ensure a contamination free eutectic is produced.

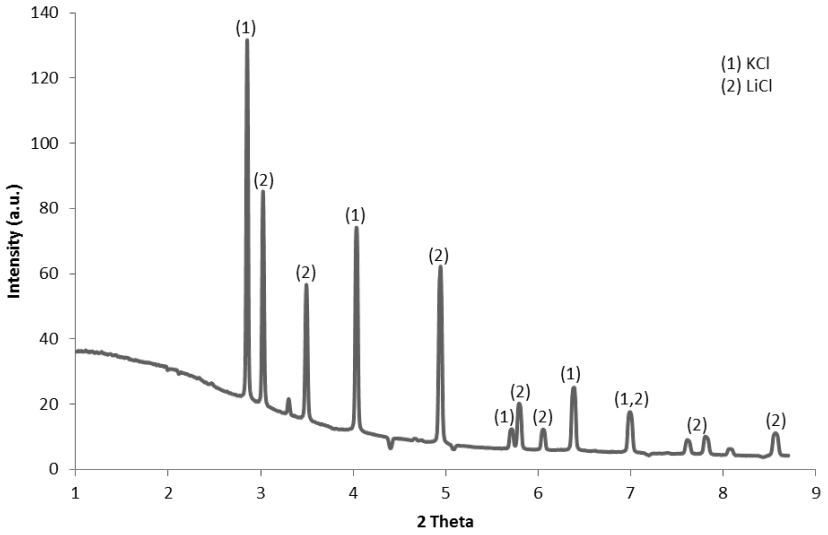

Fig. 4.12: XRD results of LKE that was dried using the technique described in Section 4.4. The peaks are identified to be (1) KCl and (2) LiCl. There are a couple of small peaks due to X-ray florescence of the XRD equipment

4.5 Anode

Unless otherwise stated, all electrochemical measurements taken were used with a dense graphite rod (Alfa Aesar). These graphite rods typically possessed 3 mm Ø and were 35 mm in length. Prior to use, the graphite rods were heated in a flame until they glowed red. This was done to remove any residual water contained within.

4.6 Reference Electrode

The reference electrode is very important whilst carrying out electrochemical measurements. Ideally, the reference electrode will provide a stable, well defined electrode potential which is used to relatively compare the potential of the working electrode. However, in practice, a completely stable reference is not achievable. Instead, reference electrodes are manufactured to provide as stable of a potential as physically possible, of which one is the silver-silver chloride (Ag|AgCl) reference electrode. This reference electrode defines a relatively stable potential by incorporating an electrochemical reduction-oxidation (redox) reaction. The redox reaction for the

Ag|AgCl reference electrode occurs at a potential of -0.197 V with respect to the standard hydrogen electrode, according to the Nernst equation, which is described in more detail in Section 5.

In the work presented in this thesis, Ag|AgCl reference electrodes were manufactured for use with all experiments. The Ag|AgCl reference electrode functions via a reversible redox reaction between a silver wire and its chloride salt. The reactions can be presented as:

$$Ag^{+} + e^{-} \leftrightarrow Ag \tag{4.1}$$

$$AgCl \leftrightarrow Ag^{+} + Cl^{-} \tag{4.2}$$

Giving rise to an overall equation

$$AgCl + e^{-} \leftrightarrow Ag + Cl^{-} \tag{4.3}$$

The membrane of the Ag|AgCl reference electrode has been studied in order to attain the reference electrode with least ionic resistance in the junction between the reference electrode electrolyte and bulk electrolyte. AC phase shifts in electrochemical measurements obtained via potentiostats may occur due to high reference electrode membrane impedance at this junction. Therefore, reference electrodes with a lower membrane junction impedance give rise to a greater sensitivity of potentiostat readings [143]. A phenomena which could be particularly important when investigating small electrodes.

Two membrane materials were used for this study. The first was an alumina based (*ca.* 60% β-Al_2O_3) material named Pythagoras (Multi-Lab Ltd.). This material has been used extensively in molten salt based work [144-148] . The second was a glass membrane based on an all-glass reference electrode conceived by Bockris *et al.* [149]. The reference electrodes were composed of 350 mm (L) x 4 mm (ID)

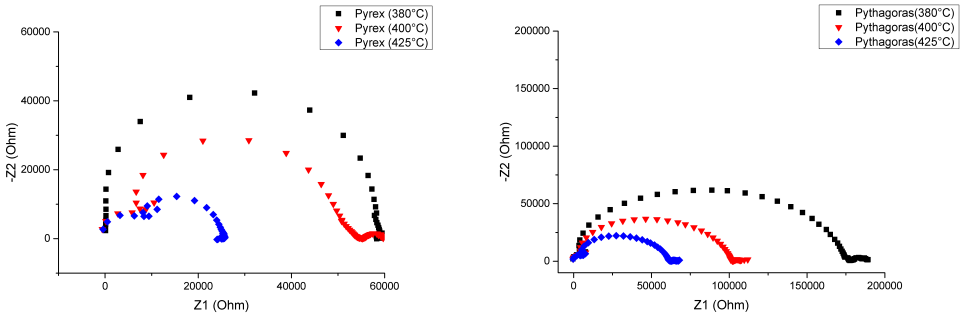

(a) Pyrex Glass RE (b) Pythagoras RE

Fig. 4.13: Reference electrode impedance

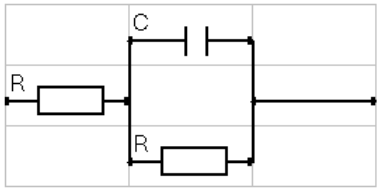

Fig. 4.14: Equivalent circuit model

x 6 mm (OD) Pyrex glass and Pythagoras, closed one end tubes. 0.75 mol kg^{-1} of silver chloride (>99%, Sigma) was added to LKE and was dried under vacuum for 24 hours at 175°C before being transferred to an Argon filed glove box, ready for assembly. The dried salts were funnelled into the electrode membrane and a 0.2 mm diameter silver wire was pushed into the electrodes and sealed with Suba-Seals. This sealed assembly was then removed from the glove box and inserted into the reaction vessel (with temperatures exceeding 400°C) to ensure the salt became molten. The silver wire was pulled up from the bottom of the tube by 2 mm. The electrode was then ready to be used immediately or could be removed, cooled and then stored for later use.

Both Pyrex glass and Pythagoras reference electrodes were tested for ohmic resistivity using electrical impedance spectroscopy (EIS) to ensure that the reference electrode with the lowest ohmic resistivity was employed in later experiments. In these tests, a two electrode set-up was employed whereby the reference electrodes

Ohmic resistance (kΩ)			
	380°C	400°C	425°C
Pyrex	59.55	51.79	25.20
Pythagoras	174.7	100.9	61.76

Tab. 4.2: Ohmic resistance of reference electrodes

were made the working electrode and a graphite rod was made the counter electrode. The molten salt crucible containing 100g of LKE and was raised to working temperatures of 380°C, 400°C and 425°C of which the impedance on both electrodes was tested.

Figure 4.13 shows the results of the test for both electrodes. The data was then analysed by fitting an equivalent circuit model using the IVIUMsoft software package, as shown in Figure 4.14. The first resistance was attributed to the electronic resistance of the silver wire. This is confirmed by similar resistances exhibited for both types of reference electrode at all temperatures. The capacitance was attributed to the double layer which is built up due to the reversible redox reaction of the reference electrode according to Equations 4.1-4.3. The second resistance is attributed to the ohmic resistivity of the membrane material. The results of the ohmic resistances of both electrodes at given temperatures are presented in Table 4.2

From Table 4.2, it is clear that the ohmic resistance of both types of electrodes reduces as the temperature increases. However, the Pyrex glass reference electrodes give rise to significantly smaller ohmic resistance at the desired working temperatures. The results suggest that the ionic movement of ions through the Pyrex glass membrane is more efficient than that of the Pythagoras tubing. Therefore, the all-glass reference electrode was used within the cell during experiments.

4.7 pO^{2-} Indicator Electrode

In molten salts, a phenomenon named oxo-acidity exists; this is a system containing oxo-acids (oxide anion acceptors) and oxo-bases (oxide anion donors). Analogous to acid-base couples in aqueous solutions, the oxo-acidity of a molten salt may play a key role in defining the stabilisation of species in the melt. By definition, the oxo-acidity of a melt is characterised by the (negative logarithm of) activity of oxide anions dissolved in the melt. Again, one can draw comparisons with the aqueous acid-base system whereby the pH of the solution is defined as the (negative logarithm of) activity of hydrogen cations. That is, the oxo-acidity (or oxo-basicity) of a molten salt system is defined as the value pO^{2-}: the negative logarithm of the activity of oxide anions within the melt:

$$pO^{2-} = -log\left(O^{2-}\right) \tag{4.4}$$

Where the parenthesis denote the activity of the ion in which they contain. In practice, it may be highly difficult to compute the real activity of the ionic solutes in molten salt media. However, because of the strong ionic nature of the molten salts, they tend to act as ideal solutions. Therefore, one can approximate the activity of ions dissolved inside the melt to be equal to the concentration (molality) of that ion. That is, the activity coefficient of ionic solutes is unity. This assumption is, generally, permitted because the ionic solutes, generally, do not alter the ionic strength (or idealisation) of the molten salt solvent [25].

In order to understand the effect of the pO^{2-} on electrochemical redox reactions, the reader is referred to Section 5. However, in terms of allowing one to monitor the oxo-acidity of a molten salt, the use of a pO^{2-} indicator electrode may be utilized and is described here.

As the oxo-acidity of a molten salt is dependent on the oxygen anion, O^{2-}, the use of a membrane allowing the selective mobility of O^{2-} is necessary. Yttria

stabilized zirconia (YSZ) is a membrane that contains such properties and may be used in order to create such a device. By doping zirconia with a percentage of yttria, vacancies are created within the material which are large enough to accommodate oxide anions. Because the valency of yttria (Y^{3+}) is lower than that of zirconia (Zr^{4+}), for every 2 molecules of Y_2O_3 inside the lattice, an oxygen vacancy is created to ensure overall charge compensation [150, 151]. The concentration of yttria inside the membrane will define the number of vacancies within the lattice; the more yttria inside the lattice, the higher the number of vacancies and, therefore, a higher ionic conductance is foreseen. On the other hand, increasing the concentration of yttria inside the lattice will have other undesirable effects on the material. As such, a typical percentage doping of yttria is around 3-8 mol% [152]. These vacancies inside the lattice allow the conductivity of oxide anions via the vacancy diffusion mechanism; oxygen "hopping" through the vacancies. With this is mind, one can conceive a reference electrode which is susceptible to a change in the activity of oxide ions. By measuring the potential of this electrode to that of one which is not susceptible to changes in the activity of O^{2-} ions (such as an all-glass $Ag|Ag^+$ reference electrode), any changes in the measured potential must be due to a change in pO^{2-}.

YSZ tubes containing 8 % mol. yttria were procured measuring 6.35 mm OD x 4.78 mm ID x 350 mm L (Multi-Lab). The tubes were baked at 400°C for 2 hours to remove any residual moisture. The tubes were then transferred to the MBraun glove box (see Section 4.8) for storage. During preparation of the pO^{2-} indicator electrodes, the same procedure was followed as in the manufacture of the $Ag|Ag^+$ reference electrodes described in Section 4.6 . However, a known quantity of Na_2CO_3 or Li_2CO_3 is also added to the salt. These carbonates decompose in the molten salt and introduce a O^{2-} ions into the electrode via the following equations:

$$(Na, Li)_2CO_3 \rightarrow 2(Na, Li)^+ + CO_3^{2-} \tag{4.5}$$

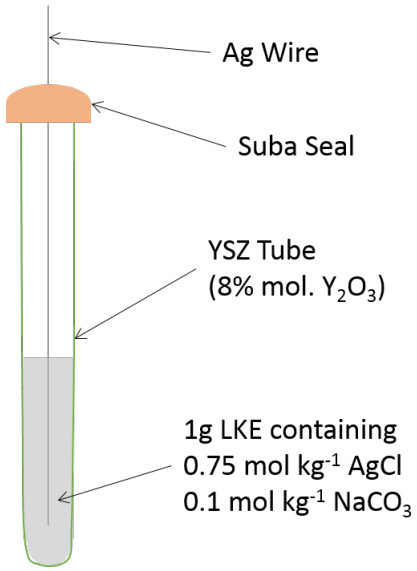

Fig. 4.15: Showing a schematic of a pO^{2-} indicator electrode.

$$CO_3^{2-} \rightarrow CO_2 + 2O^{2-} \tag{4.6}$$

The dissociation constant for the carbonate ion (Equation 4.6) is sufficiently large so that if the partial pressure of CO_2 in the atmosphere is low, full dissociation occurs [25]. By ensuring a flow of inert gas in the cell, for example, these conditions may be achieved. Therefore, the addition of one mole of $(Na,Li)_2CO_3$ into the salt, introduces one mole of O^{2-} ions into the bulk. A schematic of a pO^{2-} indicator electrode is shown in Figure 4.15

4.8 Glove Box

A glove box is required for all experimentation and preparation due to the hygroscopic nature of the salts, as described in Section 4.4. Two glove boxes have been used in this work; the first for cell preparation and the second to carry out experiments.

For preparation of the cell, it is imperative that the salts are open to a dry inert atmosphere. An MBraun glove box is utilised for this work, maintaining an

argon atmosphere with <0.5ppm of oxygen and water. This glove box, however, is not large enough to accommodate all of the heating equipment to take the cell up to the required reaction temperature and so a custom built glove box is used for experimentation.

Once the cell has been sealed inside the MBraun glove box, it is transferred to the custom built glove box. The atmosphere is dried by pumping the air through a calcium carbonate desiccant and back into the box. The humidity is controlled via a Pico Humidiprobe attached to a Eurotherm PID controller and solid state relay which controls the desiccant pump. This glove box is able to maintain an environment of 0.3% relative humidity. The temperature of the glove box is monitored via 6 K-type thermocouples, attached to each panel, and two convection fans to ensure heat is distributed evenly inside. If the temperature reaches a level ≥80°C, the power supply to the furnace is automatically disengaged until a manual reset is performed.

4.9 Summary

This chapter has outlined all of the experimental equipment used to procure experimental results in the proceeding chapters. The combination of Chapters III and IV should adequately describe the experimental set-up, procedures and theory all used to derive the experimental results outlined in Chapters VI, VII and VIII.

Chapter V will present novel Littlewood diagrams which have been used extensively throughout the design of experiments. Chapter VI will portray the production of uranium dioxide powder whilst Chapters VII and VIII focus on the characterisation of the electroreduction and materials respectively.

Chapter V. Littlewood (Predominance) Diagrams

Sections of this work have been peer reviewed and published in the Journal of Applied Electrochemistry (Brown, L. D., Abdulaziz, R., Simons, S., Inman, D., Brett, D. J. L., & Shearing, P. R. (2013). *Predominance diagrams of uranium and plutonum species in both lithium chloride–potassium chloride eutectic and calcium chloride.* Journal of Applied Electrochemistry, 43(12), 1235-1241.)

5 Littlewood Diagrams

Littlewood (or Predominance) diagrams are a useful tool for rapid prediction of a metal-oxide-halide molten salt system (although other molten salt systems - such as nitrates - may also be used). The use of thermodynamic data, experimentation or a combination of both may allow visualisation of a molten salt system and to predict the conditions necessary for certain species to be stable. Analogous to Pourbaix diagrams, Littlewood diagrams are a plot of potential *vs.* the negative logarithm of the activity of O^{2-} ions, commonly known as pO^{2-}.

With pure molten salts - using a metal halide salt as an example - the system can be understood to be a complete dissociation of the metal cations and halide anions. That is, the salt exists as a liquid composed of ionic media. By employing the Gibbs free energy of formation of this halide cation to be equal to zero, the molten salt system may be depicted with the Gibbs free energy of formation of the halide acting as an internal reference. This notion is very simple and is the basis of the thermodynamic prediction of molten salt systems.

Assuming that a small concentration of the cation's metal oxide is added and is soluble in the salt, not only does the salt now consist of the metal cation and halide anions, but a new anion, O^{2-}, exists. The relative Gibbs free energy of

formation of this oxygen anion may be then also be calculated (with respect to the internal reference) and be used to deduce the Gibbs free energy of electrochemical half cell reactions, that involve O^{2-} ions. This allows for thermodynamic description of electrochemical reductions or oxidations of, say, an oxide or oxychloride. This defines the foundations in which Littlewood diagrams are used to describe a molten salt system.

5.1 Thermodynamic Definition of a Molten Salt System

Novel, thermodynamically calculated, Littlewood diagrams at unit activity are presented for the first time in LKE at 500°C. Named after R. Littlewood, who first described them in 1962 [28], these diagrams are analogous to Pourbaix diagrams in aqueous media and are able to thermodynamically describe a metal-molten salt system. Littlewood diagrams are constructed by plotting the electrode potential, E, versus the negative logarithm of the activity of oxide ions in the melt, the pO^{2-} (as opposed to pH in Pourbaix diagrams). Lines are used to separate regions of stability of different species in the molten salt media. The interface between two species define when those two species co-exist together, both with an equal activity. The thermodynamic definition of the U-LKE system is important as it highlights the complexity of different species that can exist/co-exist within the melt.

A fundamental phenomenon of these diagrams is the three different types of reaction that can occur within a molten salt electrochemical cell: the sole transfer of oxygen anions; the sole transfer of electrons and the transfer of both electrons and oxygen anions. Vertical lines depict reactions that describe oxide ion transfer, horizontal lines portray reactions involving electron transfer and, lastly, diagonal lines depict the reactions that involve transfer of both electrons and oxygen anions. Examples of these different reactions can be seen in Equations 5.1 - 5.3 respectively (where “M” denotes a generic metal).

$$MO + 2Cl^- \leftrightarrow MCl_2 + O^{2-} \tag{5.1}$$

$$MCl_2 + 2e^- \leftrightarrow M + 2Cl^- \tag{5.2}$$

$$MO_2 + 4e^- \leftrightarrow M + 2O^{2-} \tag{5.3}$$

In order to plot the interfaces, equations linking the pO^{2-} to the cell potentials for each half-cell reaction are required. The free energies of these system equations can be related to electromotive force, E, via Equations 5.4 and 5.5. The pO^{2-} is then related to the cell potential via the Nernst equation (Equation 5.6).

$$-\Delta G^0 = nFE_0 \tag{5.4}$$

$$-\Delta G = nFE \tag{5.5}$$

$$E = E_0 + \frac{RT}{nF} ln \left(\frac{\Pi_j a_j^{\upsilon_j}}{\Pi_i a_i^{\upsilon_i}} \right) \tag{5.6}$$

By applying this equation to the electrochemical reaction of Equation 5.3, for example;

$$E = E_0 + \frac{RT}{nF} ln \left(\frac{a_{MO}}{a_M \, a_{O^{2-}}} \right) \tag{5.7}$$

The lines separating each region may be defined as the point at which both species co-exist each at unit activity which allows Equation 5.7 to be written in a more

suitable form:

$$E = E_0 - \frac{2.303RT}{nF} log(a_{O^{2-}}) \tag{5.8}$$

To incorporate oxygen into the system, a definition of the standard state of oxide ions is required. The pure oxide of the cation of the chloride melt is therefore defined as unit activity. Due to the standard free energy being defined in this way, values will change depending on which melt is used to define the oxide ion. In the case of a a mixed system or a eutectic, the activity of O^{2-} ions may be defined by one of the metal chlorides and adhered to throughout. One will find that by calculating the diagrams using another cation oxide as the basis, the diagram will look the same but will be shifted along the X (pO^{2-}) axis.

However, in the case of this work in LKE, a weighted molar average of formation of O^{2-} ions will be taken under the principle that O^{2-} ions will have a Li^+, K^+ and Cl^- environment as their nearest neighbour shells. This is due to the melt having a quasi-crystalline structure [153-155]. As the O^{2-} ions are a minority in the melt, and that the melt is a eutectic formed from two alkaline metal salts, the nearest neighbour shells would be that of chloride ions, of which are produced via dissociation of both lithium chloride and potassium chloride at the molar average of 59% LiCl and 41% KCl. Therefore, the pure oxide of the cation is calculated to be of a weighted average of both Li_2O and K_2O. The following passage shows how the standard free energy of O^{2-} ions has been calculated:

In a pure potassium chloride melt, the standard state of oxide ions would be K_2O. The reaction to form oxide ions would thus be

$$2K + \frac{1}{2}O_2 \leftrightarrow 2K^+ + O^{2-} = \Delta G_{K_2O} \tag{5.9}$$

The standard free energy of formation of the oxide ion can therefore be defined as

$$\Delta G^0_{O^{2-}_K} = \Delta G^0_{K_2O} - 2\Delta G_{K^+}{}^0 \tag{5.10}$$

Similarly, Equations 5.9 and 5.10 can be written for Li_2O:

$$2Li + \frac{1}{2}O_2 \leftrightarrow 2Li^+ + O^{2-} = \Delta G_{Li_2O} \tag{5.11}$$

$$\Delta G^0_{O^{2-}_{Li}} = \Delta G^0_{Li_2O} - 2\Delta G_{Li^+}{}^0 \tag{5.12}$$

At 773 K the standard free energy of K_2O & metallic K are -252.77 kJ/mol [156, 157] & -362.66 kJ/mol [158, 159] respectively. For Li_2O & LiCl the values are -496.75 kJ/mol [156, 157, 159] & -344.85 kJ/mol [159, 160] respectively. By assuming a weighted average of oxide ions produced from lithium and potassium, a standard free energy of oxide ions in the melt can be calculated:

$$\Delta G^0_{O^{2-}} = 0.59^*\Delta G^0_{O^{2-}_{Li}} + 0.41 * \Delta G^0_{O^{2-}_K} \tag{5.13}$$

Using Equation 5.13, the standard Gibbs free energy of oxide ion formation has been calculated to be -357.91 kJ/mol.

Now that the standard free energy of the oxide ion is known, it can be used to deduce the relationship between the oxygen pressure, oxide activity and potential, *i.e:*

$$\frac{1}{2}O_2 \leftrightarrow O^{2-} + 2e^- \tag{5.14}$$

Applying the Nernst relationship to Equation 5.14, one yields:

$$E_{O^{2-}} = E_{0_{O^{2-}}} - \frac{RT}{nF} ln \frac{(a_{O_2})^{0.5}}{a_{O^{2-}}} \tag{5.15}$$

By varying the pressure of oxygen within the system, Equation 5.15 can be used to

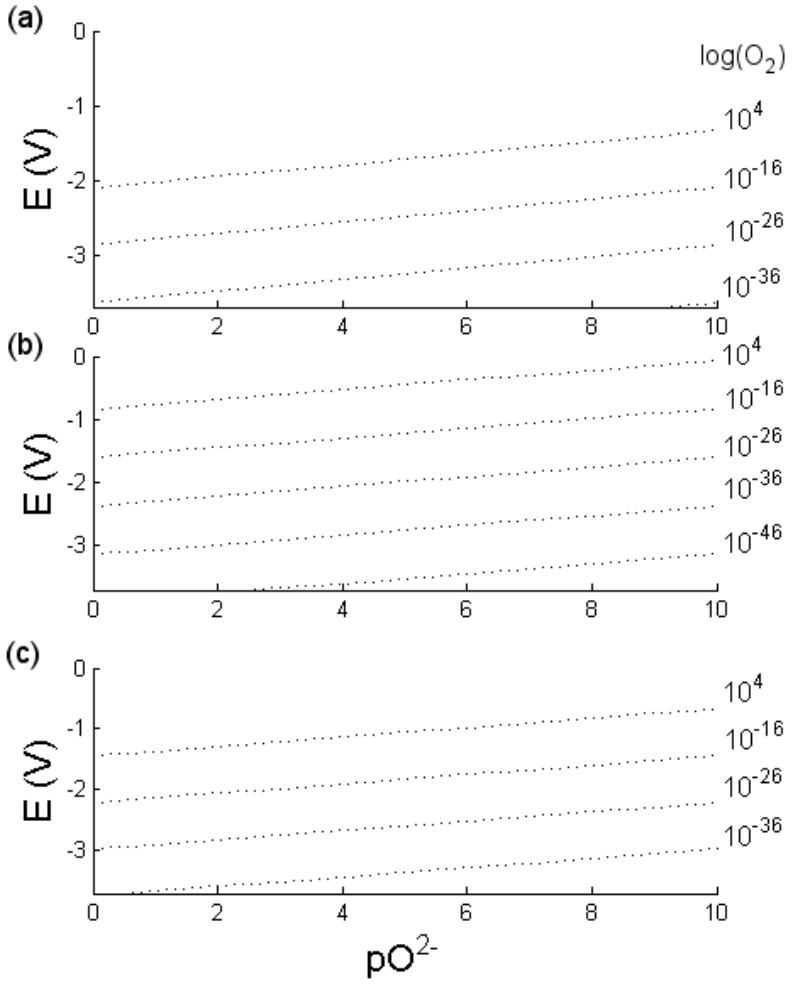

Fig. 5.1: Shows the relationship between oxide activity, potential and (logarithm of) oxygen pressure for (a) LiCl, (b) KCl and (c) LKE at 773 K.

plot the relationship between oxygen pressure, oxide activity and potential. These base graphs have been constructed for both LiCl and KCl in order to present the different conditions each salt possess. These are shown in Figures 5.1(a) and 5.1(b) respectively. A third diagram is also presented in Figure 5.1(c) using the analogy of O^{2-} ions being formed from both Li_2O and K_2O, as mentioned previously. The diagrams shown in Figure 5.1 can then be used as a base diagram whereby the different regions of stability are superimposed. The regions of stability are calculated by applying the Nernst equation to each reaction that may occur in the molten salt

environment, such as those shown in Equations 5.1 - 5.3. Thermodynamic data used was obtained from references [156 -168].

5.2 Uranium Species in Molten Salts

Novel Littlewood diagrams (using thermodynamic calculations only) are presented at unit activity for uranium species in both LKE and $CaCl_2$. Additional calculations were made in the $CaCl_2$ molten salt due to the recent high interest in this particular salt and to enable comparisons to be drawn with a salt that operates at a higher temperature compared to LKE. It should be noted that all diagrams presented in this chapter are with reference to the $Cl^-|Cl_2$ couple. The regions of stability are named from the thermodynamic data used to construct the diagrams. However, this does not necessarily depict the species that actually exist, but instead describes the oxidation state of the metal. For example, a region named UCl_3 does not necessarily mean that UCl_3 exists. However, it does describe that U exists in the salt in the 3+ oxidation state, as indicated by Equation 5.16:

$$UCl_3 \rightarrow U^{3+} + 3Cl^- \tag{5.16}$$

5.2.1 LKE

The Littlewood diagram for uranium species in LKE is presented in Figure 5.2. The solid black lines depict the conditions necessary for the two species (which that line separates) to co-exist together, both at unit activity. The regions themselves depict when only the species that belongs to that region exists at unit activity. Other species may exist; however, their activity will be less than unity. Observation of Figure 5.2 shows many regions of stability for various uranium species. These regions include a large region for lithium uranate, regions for oxides and chlorides as well as a small region for an oxychloride. This shows the complexity of the uranium-LKE molten salt system.

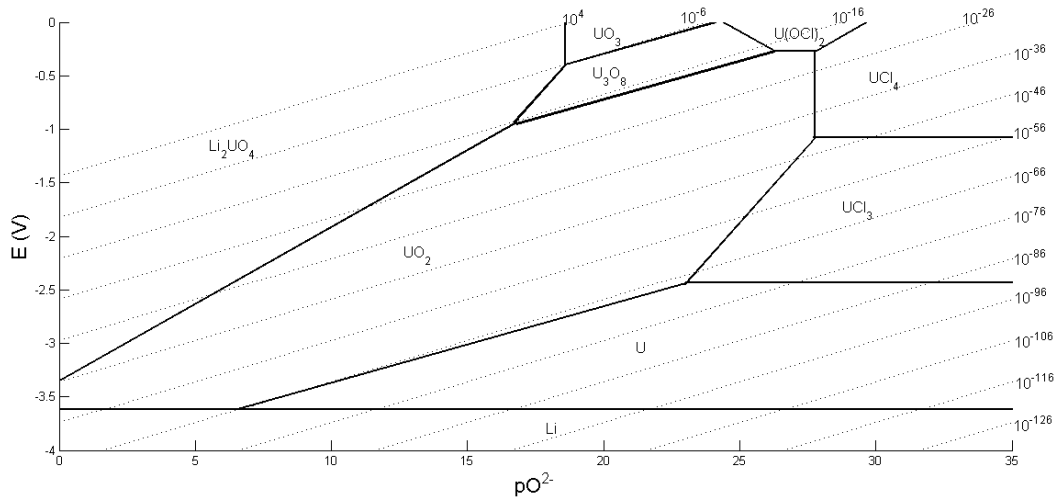

Fig. 5.2: Uranium species in the LKE molten salt at 773 K. Potassium deposition has been been omitted due to it having a more negative deposition potential to lithium. Potassium uranate has also been omitted.

Perhaps the most important aspect of this diagram is that of the thermodynamically predicted reduction mechanism for the electroreduction of uranium dioxide to metallic uranium. The diagram predicts a simple, 4-electron transfer reduction to the metallic phase. This is in agreement to the observations made by Sakamura *et al.* and Iizuka *et al.,* who also observed a 4-electron transfer [66, 67]. Another important prediction of this electroreduction is the dependency of the activity of O^{2-} ions. Figure 5.2 predicts that the electrochemical reduction will only occur with a pO^{2-} level between 6-23. If attempting to electrochemically reduce at a pO^{2-} of < 6, one will reach the cathodic decomposition potential of the molten salt before reaching the electrochemical reduction potential. Therefore, the microstructure of the UO_2 working electrode may have a significant effect on the electrochemical reduction. For example, if one assumes a highly tortuous electrode with a low density of TPIs then this would result in the inhibition of the diffusion of O^{2-} ions away from the electrode. This, in turn would increase the local level of pO^{2-} at the electrode and, thus, affect the electrochemical reduction potential.

In addition, it is worth noting that if one desired to produce uranium metal via

the electrochemical reduction of U_3O_8, then the electrochemical reduction mechanism is predicted to be:

$$U_3O_8 \rightarrow UO_2 \rightarrow U \tag{5.17}$$

The reaction pathway shown in Equation 5.17 is the same reaction pathway as seen by Hur *et al.* and by Jeong *et al.* [61, 63].

It is also important to note that the electroreduction of UO_2 to metallic U in LKE is more facile at higher temperatures, with respect to controlling the $p\mathrm{O}^{2-}$ of the melt. This is due to the fact that at low temperatures and low values of $p\mathrm{O}^{2-}$ (ca. 0–6) lithium deposition would occur preferentially to the oxide reduction. These observations show that Littlewood diagrams are a very useful tool to predict metal-molten salt systems.

5.2.2 $CaCl_2$

The Littlewood diagram for uranium species in the $CaCl_2$ is presented in Figure 5.3. Perhaps the most striking comparison of the diagrams in Figures 5.2 and 5.3 are the differences in location of the phases: the region for stability of UO_2 is smaller and is shifted to lower values of $p\mathrm{O}^{2-}$ in the calcium chloride melt, compared to that of LKE. This is explained thermodynamically: as the temperature of the system is increased, the Gibbs free energy change of the electrochemical reaction is less negative and, therefore, the Nernst potential becomes less negative for given activities of oxide ions. Differences in stability between Li_2O and CaO are not considered.

Again, the electrochemical reduction from UO_2 to U in $CaCl_2$ is also predicted to be a single, 4-electron transfer process. This prediction is also in agreement with studies that observed this electrochemical mechanism and with the predicted reaction mechanism in the LKE melt [63, 169].

Additionally, the region of stability of UO_3 has now shifted to potentials more

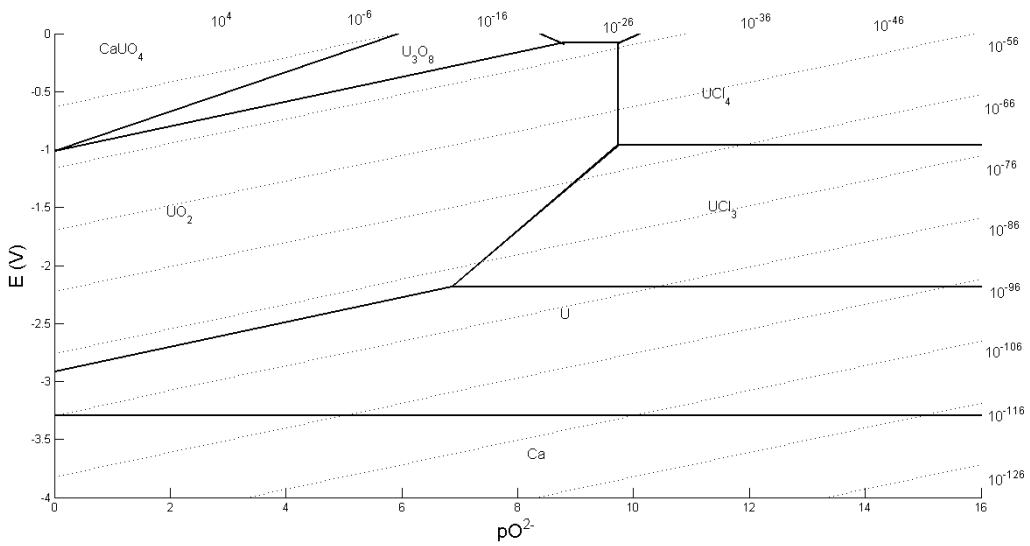

Fig. 5.3: Littlewood diagram showing uranium species in $CaCl_2$ at 1073 K

anodic than the anodic decomposition potential of calcium chloride. That is, if one were to assume a $p\mathrm{O}^{2-}$ level of 7 and were to sweep the potential from *ca.* -0.4 V to more positive potentials, then one would evolve chlorine gas as a product of melt decomposition before reaching the potential to oxidise U_3O_8 to UO_3. Therefore, the Littlewood diagram predicts that it would not be possible to electrochemically reduce UO_3 to U_3O_8 in $CaCl_2$ at 1073 K.

Moreover, it is important to note that the electroreduction of UO_2 to U in $CaCl_2$ is facile compared to that of LKE. This is because there is a large region of stability of UO_2 to U, which does not depend on the activity of oxide ions. This would, therefore, mean that the microstructure of the electrode would not be as important in ensuring the local level of $p\mathrm{O}^{2-}$ remains within the necessary levels.

5.3 Plutonium species in Molten Salts

Plutonium species have also been considered during this investigation as spent nuclear fuel will contain a certain percentage of plutonium dioxide. And, as mentioned in Section 1.1, plutonium may also be burned up inside a (MOX) nuclear reactor. Therefore, the electrochemical reduction of plutonium dioxide would also be of great

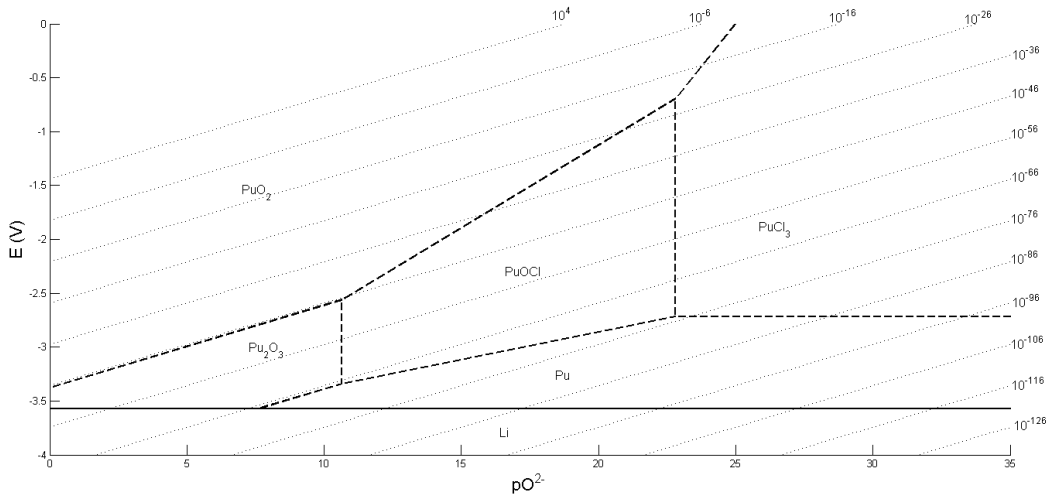

Fig. 5.4: Littlewood diagram of plutonium species in LKE at 773 K.

interest within the scope of this Ph.D thesis. Again, the Littlewood diagrams are constructed in both LKE and $CaCl_2$ molten salts.

5.3.1 LKE

Figure 5.4 shows the Littlewood diagram for plutonium species in LKE at 773 K. For the plutonium Littlewood diagrams, dashed lines are used to separate regions of stability instead of solid black lines used in Figures 5.2 and 5.3. Figure 5.4 shows only 5 regions of stability for various plutonium species, including a relatively large region of stability for the oxychloride, PuOCl. Interestingly, the Littlewood diagrams predicts intermediate phases in the electroreduction of PuO_2 metallic Pu: the first is Pu_2O_3 and the second is PuOCl. Moreover, similar to the uranium species in LKE, the Littlewood diagram predicts that the pO^{2-} must not fall below a level of *ca.* 7.5 as this would cause the reduction potential of Pu_2O_3 to Pu to be more cathodic than the cathodic decomposition potential of LKE.

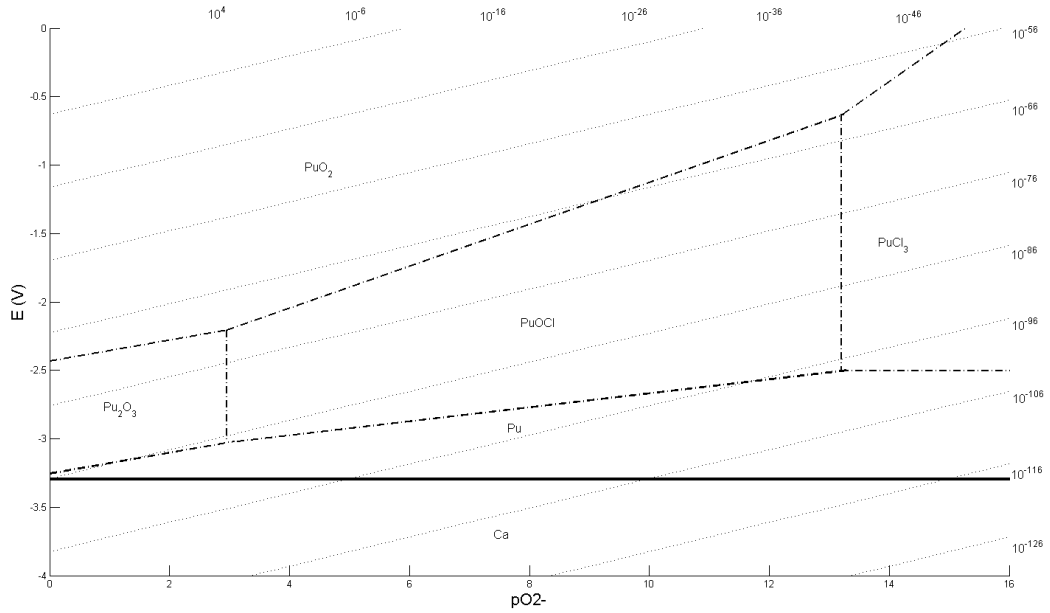

Fig. 5.5: Littlewood diagram of plutonium species in $CaCl_2$ at 1073 K

5.3.2 $CaCl_2$

Lastly, the stability of plutonium species in $CaCl_2$ are presented in Figure 5.5. This Littlewood diagram also shows 5 stable species. However, the region for stability for Pu_2O_3 is much smaller. Again, the diagram predicts an intermediate species in the electrochemical reduction of PuO_2 to metallic Pu. Similarly to Figure 5.3, the reduction is not dependent on the level of pO^{2-}. However, if the electroreduction occurs at low levels of pO^{2-} (say 0.1), any under-potential associated with electrolyte decomposition could see electroplating of calcium metal to occur (due to decomposition of the molten salt).

5.4 Prediction of Selective Electroreduction

Considering that spent nuclear fuel pellets contain both uranium and plutonium dioxide (alongside other rare earths and actinides), thermodynamic prediction of the feasibility of selective electrochemical reduction and separation of these species is desirable: this can be achieved by superimposition of the uranium and pluto-

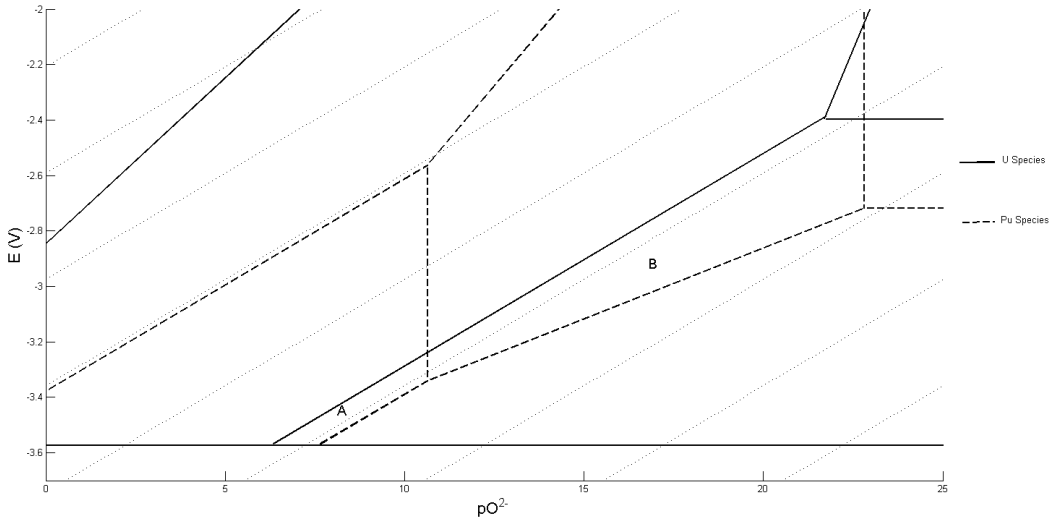

Fig. 5.6: Superimposed Littlewood diagrams of uranium species and plutonium species in LKE at 773 K. Points A and B show the regions in which one could selectively electrochemically reduce $UO_2$to metallic U without also producing metallic Pu.

nium based diagrams in LKE. Figure 5.6 shows a magnified section of the result of superimposing Figures 5.2 and 5.4.

It can be seen that there would be an inherent difficulty at separating both species at unit activity due to the reduction potentials of $UO_2|U$ and $Pu_2O_3|Pu$ being very similar (*ca.* 100 mV apart), as denoted by point A on Figure 5.6. The diagram also shows that in order to produce metallic uranium from a mixed oxide sample, PuO_2 will also be electrochemically reduced to produce Pu_2O_3. However, the reduction potentials of PuOCl|Pu, and $UO_2|U$ diverge at higher values of pO^{2-}, leading to a greater possibility of being able to selectively reduce to metallic species, as shown by point B. Figure 5.6 provides *a priori* guidelines to inform the experimental conditions required for selective reduction of mixed oxides; for example, production of metallic uranium is feasible by reducing a mixture of uranium dioxide and plutonium dioxide, as the reduction potential of $UO_2|U$ is more positive than that of the $Pu_2O_3|Pu$ reduction potential. The lines are, however, very close to one another and give a narrow region whereby reduction to produce metallic ura-

nium only, as depicted by point A. The diagram is extremely useful in predicting the conditions necessary for this selective electrochemical reduction to occur. The Littlewood diagram is also able to predict different reduction mechanisms and the conditions necessary to achieve this.

5.5 Differences Between Previously Published Diagrams

In previously published papers containing Littlewood diagrams of uranium and plutonium (see Section 2.2.1), information has been empirically derived through titration methods of the nuclear elements into the molten salt. As a direct result of this, the activities of these nuclear species are all less than unity (approximately, in concentrations of 0.02 mol kg^{-1}). Thus, the location of lines depicting regions of stability are shifted to different values of pO^{2-}.

The method of producing these diagrams here is based purely on thermodynamic data and is, therefore, inherently more flexible in accounting for the effects of changing activity. For example, if one were to take the concentration of PuOCl to be 1x10^{-1} mol kg^{-1} (an approximation to the activity) then the pO^{2-} value at the equilibrium of Pu_2O_3|PuOCl would be shifted towards the left on the diagrams to lower pO^{2-}. This can be calculated as follows:

$$E^0 = \frac{2.303RT}{nF} log\left(\frac{[Pu_2O_3]}{[PuOCl]^2[O^{2-}]^3}\right) \tag{5.18}$$

Assuming the activity of Pu_2O_3 to be unity Equation 5.18 simplifies to:

$$pO^{2-} = \frac{\triangle G}{3x2.303RT} + \frac{2}{3} log([PuOCl]) \tag{5.19}$$

This would result in the line separating Pu_2O_3 and PuOCl to shift to a value of *ca.* 9.9, as shown by point C in Figure 5.7. Furthermore, points D and E show where the line would be if the activity of PuOCl were 10^{-2} , and 10^{-3}, respectively. It can therefore be seen that one would be able to alter these regions by changing

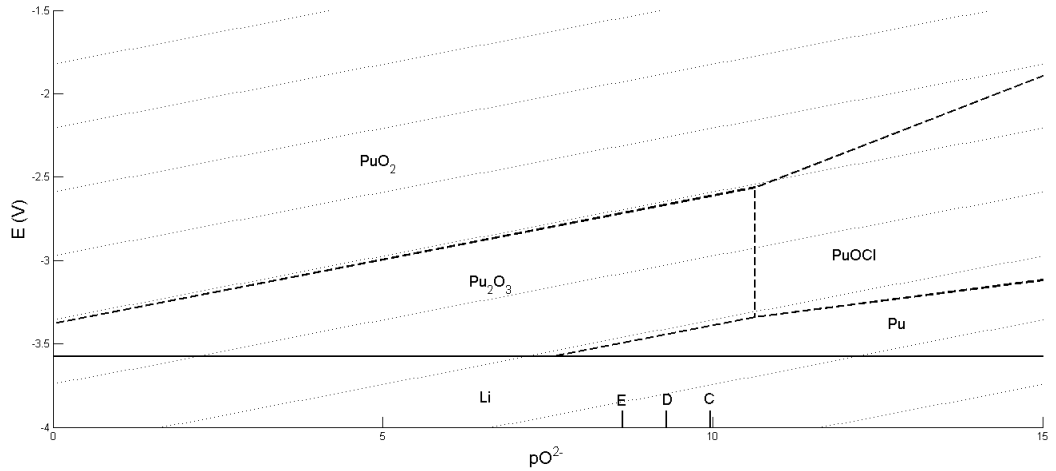

Fig. 5.7: Littlewood diagram at 773 K showing the effect of changing the activity of PuOCl to be less than unity. Points C, D and E depict the level of pO^{2-} where the line separating the Pu_2O_3 and PuOCl regions would be at activities of 10^{-1}, 10^{-2} and 10^{-3} respectively.

the activity of the appropriate species within the melt. Lower activities could be used, for example, creating larger regions of stability. By ensuring all species are at a lower activity, the diagrams would change further.

5.6 Conclusion

To conclude, novel Littlewood diagrams have been presented for both uranium and plutonium species in LKE and $CaCl_2$ molten salts based solely on thermodynamic data. Inherently, these diagrams are limited by the thermodynamic data available but they provide a useful tool to predict the state of molten salt systems. Although the eutectic is assumed to be ideal, in the case of LKE, the diagrams agree with previously published diagrams obtained experimentally, allowing for changes in species activity. There is no issue of complex ion formation in the LKE mixture and so ideality is a good approximation to the real system.

The diagrams presented allow for the thermodynamic prediction of separation of these species via a direct electrochemical reduction technique. The electrochemical reduction of UO_2 to metallic U is more facile at higher temperatures, as at lower

temperatures there is a need to control the pO^{2-} values to ensure electrochemical decomposition of the melt is not favoured over the electrochemical reduction process. However, if the level of pO^{2-} is adequately controlled, the Littlewood diagrams predict this electroreduction to be feasible. If the level of pO^{2-} is not adequately controlled, lithium electroplating due to decomposition of the molten salt could become more favourable. Therefore, the microstructure of the electrode could play an important role in the efficiency of the electroreduction. If the microstructure impedes the diffusion of O^{2-} ions out of the electrode, this would lower the local level of pO^{2-}: causing the deposition of lithium to become more favourable.

This phenomenon is not observed in the $CaCl_2$ molten salt, due to the higher temperature in which this system operates; that is, the level of pO^{2-} does not cause the decomposition of the molten salt electrolyte to become more favourable. However, in the case of the reduction of Pu_2O_3 to metallic Pu, low values of pO^{2-} may electroplate Ca metal simultaneously if any underpotentials exist.

Moreover, superimposition of the uranium and plutonium Littlewood diagrams in LKE show a narrow window for selective reduction to metallic uranium in a mixed oxide system containing both UO_2 and PuO_2. The diagrams predict that the electrochemical reduction of PuO_2 to Pu_2O_3 or PuOCl is inevitable in this process. Depending on the reduction mechanism, the window for selective production of uranium metal is as small as 100 mV at low values of pO^{2-} up to *ca.* 400 mV at high levels of pO^{2-}.

Lastly, the flexibility of the Littlewood diagrams has been described: techniques that can be used to predict regions of stability at various activities (or concentrations) of species in molten salt systems. This approach can be adopted to help optimise molten salt electrochemical cell designs to be able to selectively favour specific electrochemical reactions.

Chapter VI. The Production of Uranium (IV) Oxide

6 Production of Uranium Dioxide

This chapter of the report describes the how uranium dioxide was produced in-house. Chemical characterisation was also performed on the product to confirm its chemical structure.

6.1 Production of UO_2 from UNH

At the time of writing, pure grade samples of uranium dioxide are not stocked by commercial suppliers. Therefore, in order to have studied the electrochemical reduction of this compound, it was necessary to produce uranium dioxide from available uranium compounds.

The proceeding subsections will highlight experimentation that was undertaken to allow for a relatively pure grade of uranium dioxide to be produced. This section will first chemically characterise the precursor, uranyl nitrate hexahydrate, and describe experimentation used to produce uranium dioxide. Lastly, a chemical characterisation of the product is presented.

6.1.1 Characterisation of UNH

Depleted uranyl nitrate hexahydrate (UNH), considered as legacy waste at UCL, was used for the experiments of this thesis. The UNH was first characterised by X-ray diffraction to deduce the chemical structure. UNH crystals were crushed using a pestle and mortar and then inserted into a 0.5mm Ø glass capillary. A lab based X-ray diffractometer (STADI P, STOE & Cie GmbH) with a molybdenum source was used to gain an X-ray diffraction pattern. The resulting X-ray diffraction pattern can be observed in Figure 6.1.

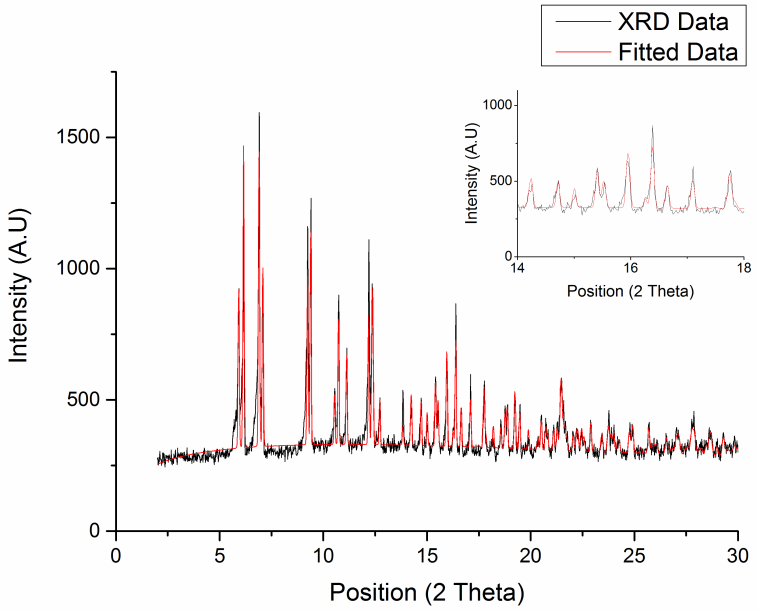

Fig. 6.1: Diffraction pattern (black) and refined data (red) of the uranyl nitrate hexahydrate precursor. The inset is a selected range of the data which shows a very good fit.

A Rietveld analysis was conducted on the diffraction pattern which fitted to that of uranyl nitrate hexahydrate. The lattice parameters were extracted to be 13.27, 8.07 and 11.53 Å (a,b,c) which is comparable to 13.18, 8.00 and 11.47 Å as analysed by Hall *et al.* [170]. Visual inspection of Figure 6.1 shows the Rietveld refinement to fit the raw data well. The inset also shows an enlarged region between 14 and 18° which allows one to see how well the refinement fits. In addition, there were no peaks that were unidentified in the data set. This suggests that the UNH precursor is of a good purity and would allow accurate transformation into uranium dioxide

6.1.2 Thermal Decomposition of Uranyl Nitrate Hexahydrate

Uranyl nitrate hexahydrate (UNH) may be used to produce uranium oxides via a thermal decomposition reaction pathway: The thermal decomposition has been extensively studied and the result of the thermal decomposition is either U_3O_8 or

UO_3, depending on the reaction conditions [171-178]. From the literature studied, it is apparent that the thermal decomposition occurs in a two steps; a dehydration reaction followed by a de-nitrification reaction. The reactions are shown as Equation 6.1 and 6.2 respectively.

$$UO_2\left(NO_3\right)_2 \cdot 6H_2O \rightarrow UO_2\left(NO_3\right)_2 \cdot H_2O + 5H_2O \tag{6.1}$$

$$UO_2\left(NO_3\right)_2 \cdot H_2O \rightarrow UO_3 + H_2O + 2NO_2 + \frac{1}{2}O_2 \tag{6.2}$$

Studying Equation 6.2 one can evaluate that toxic nitrogen dioxide gas is produced along with uranium (VI) oxide which could be reduced in hydrogen to form uranium (IV) oxide (see Section 6.1.3).

Uranyl nitrate hexahydrate was thermally decomposed via heating in an argon atmosphere using a hot plate. 5 g of UNH crystals were placed into a small Pyrex beaker which itself was placed into a larger flanged Pyrex vessel. A ceramic cell head was custom built from Phyrophillte (Ceramic Substrates and Components Ltd.) and was used to seal the reaction crucible. The ceramic cell head incorporated Swagelok connections for gas inlet and outlet, as well as a hole for a sheathed K-type thermocouple which was held into the cell head via a Suba-Seal. Because of the production of toxic nitrogen dioxide, it was decided to use a flow of inert gas to remove the NO_2 that was produced during the decomposition. A flow of approximately 0.3 standard litres per minute of argon gas was admitted into the cell for 2 hours prior to starting the experiment in order to purge the cell atmosphere. This set-up maintained an airtight seal, with the outlet gas being vented into a fume cupboard via a one way valve. The whole assembly was placed on top of a hot plate (Cimarec) which was set to 300°C, after purging was complete. The thermocouple was placed within 5mm of the UNH crystals to ensure an accurate measurement of temperature. A schematic of the set-up can be seen in Figure 6.2.

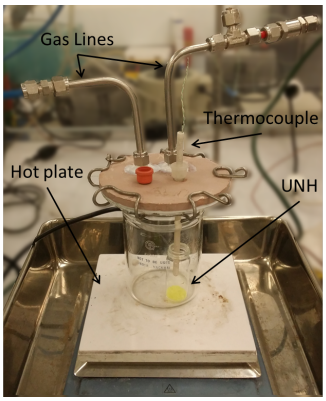

Fig. 6.2: Photograph of the experimental set-up showing the UNH, hot plate, gas lines and thermocouple

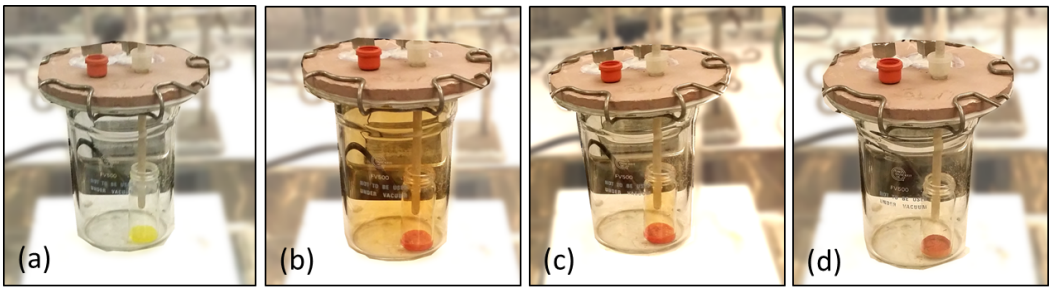

Fig. 6.3: Images of the cell at various stages in the thermal decomposition showing (a) melting of the UNH, (b) de-nitrification of UNH and a change in colour, (c) towards the end of de-nitrification the product remained in the liquid state and (d) the product has turned into a brick-red crust.

During the heating of uranyl nitrate hexahydrate, a number of observations were made. A photographic time-line of the reaction cell is shown in Figure 6.3. At 70°C, the crystals had become molten and the liquid began to bubble slowly. This would be expected as the melting point of UNH is 62°C. Once the melt had reached a temperature of 103°C, a colour change was observed: the melt turned from a fluorescent yellow/green (typical of UNH) to a burnt-orange colour. Although no *in situ* chemical analysis was possible while the sample was in this state, it is expected that this was the complete dehydration of UNH to form yellow cake, which has a characteristic burnt orange colour (another theory of this colour change is attributed to be "polymerization products" [179]). This step has been attributed

Temperature of phial	Observations
70°C	UNH became liquid. Whilst in the molten state the UNH bubbled at a slow rate
103°C	A colour change from fluorescent green/yellow to a burnt orange liquid (similar to a 0.01M iodine solution). Slow bubbling was also present.
110°C	Bubbling became more vicious. The viscosity of the liquid appeared to become higher. The viscous liquid started to become a burnt orange colour. Cell filled with an orange gas.
150°C and above	The liquid began to solidify into a brick-red coloured powder. The formation of orange gas reduced significantly. The powder that formed started to become a brick-red coloured crust.

Tab. 6.1: Observations during the thermal decomposition of UNH

to the following reaction:

$$UO_2(NO_3)_2.6H_2O \rightarrow UO_2(NO_3)_2 + 6H_2O \tag{6.3}$$

After a temperature of 110°C had been reached, a more aggressive bubbling was observed along with the production of an orange gas, as seen in Figure 6.3(b). This is due to the de-nitrification of nitrogen oxide, which is well known to be an orange gas. This de-nitrification is attributed to the equation:

$$UO_2(NO_3)_2 \rightarrow UO_3 + 2NO_2 + 1/2O_2 \tag{6.4}$$

Once the reaction displayed in Equation 6.4 had completed (no more gas was formed) the melt remained a burnt orange colour as seen in Figure 6.3(c). Upon increased heating, the melt solidified into a brick-red coloured crust, as seen in Figure 6.3(d). No further reactions occurred as the sample was taken above 150°C. A summary of the observations can be seen in Table 6.1

A sample of the brick-red crust was ground into a fine powder and inserted into

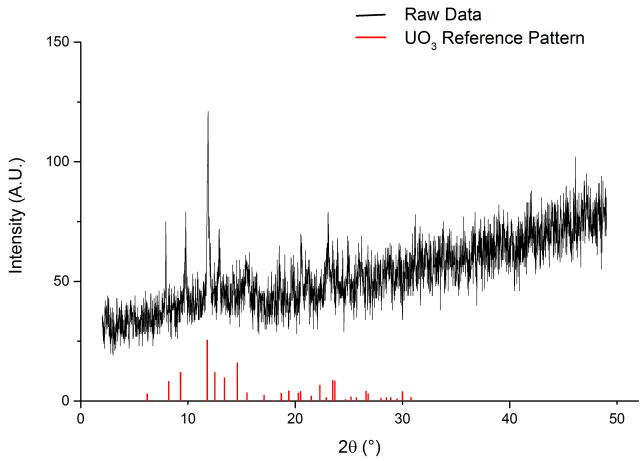

Fig. 6.4: Raw XRD data (black) of the brick-red compound formed from the thermal decomposition of UNH. A reference pattern for UO_3 is superimposed onto the graph (red).

a 0.5 mm Ø capillary tube for XRD analysis. The data is displayed along side a reference pattern for UO_3 in Figure 6.4. A full Rietveld analysis was not possible on this data set owing to a poor signal-to-noise ratio. This is most likely due to combination of large powders (typical product of a pestle and mortar) and the high attenuation of UO_3. It is likely that creating smaller powders and using a smaller XRD capillary would yield better results.

However, by comparing the raw XRD data obtained to a reference pattern for UO_3, one is able to conclude that there are similarities in the peak positions; specifically, the most intense peak in the raw data resides at a 2ϑ value of 11.87° (±0.005°), which is comparable to a 2ϑ value of 11.8(±0.05°) from literature [180]. Although lattice parameters were not able to be extracted and compared, it is likely that the product is, at least, an oxide of uranium which is likely to be UO_3. This conclusion is supported by authors who have all produced uranium oxides (UO_3 and U_3O_8 only) from the thermal decomposition of UNH [172-176].

Thermal decomposition of UNH is known to produce an oxide of uranium where uranium possesses an oxidation state greater than 4. The observations concluded

in Table 6.1 are similar to those reported by Hartland and Nesbit [174]. The oxide that is produced is likely to depend on the conditions in which the decomposition occurs but the result of the thermal decomposition seems to produce UO_3 or U_3O_8. Because of the apparent inability to produce UO_2 from the thermal decomposition of UNH, a further reduction step is necessary.

6.1.3 Production of UO_2 via Hydrogen Reduction

An interesting property of uranium (IV) oxide is it's thermodynamic stability within a hydrogen atmosphere. That is, there is no apparent hydrogen reduction of UO_3 and U_3O_8 below the composition of $UO_{2.0}$ [31]. Therefore, the reduction of either UO_3 or U_3O_8 (or a combination of both) to form pure UO_2 in a H_2 atmosphere is possible.

Indeed, the kinetics of this chemical reaction has been characterised by using thermo-gravimetric analysis (TGA) of UO_3 and U_3O_8 produced via the calcination of ammonium diuranate [182]. The author investigated the reduction of UO_3 to UO_2 using TGA at temperatures of 500-600°C in various concentrations of hydrogen. From this study, one can extract that the reduction reaction occurs in two steps; the first being a reduction of UO_3 to U_3O_8 and the second being the reduction of U_3O_8 to UO_2. The chemical reactions can be seen in Equations 6.5 and 6.6 respectively. The order of reaction for Equation 6.5 was found to be zero whilst that of Equation 6.6 varied between zero and 0.65; depending on the reaction conditions [182].

$$3UO_3 \rightarrow U_3O_8 + \frac{1}{2}O_2 \tag{6.5}$$

$$U_3O_8 \rightarrow 3UO_2 + O_2 \tag{6.6}$$

From this information, it was conceived that the product of the thermal decomposition of uranyl nitrate hexahydrate (whether it is pure UO_3 , U_3O_8 or a combination

of both) presented in Section 6.1.2, would be applicable for this reaction.

For this experiment, a horizontal tube furnace (Lenton Furnaces) equipped with PID temperature control was used as a heat source. A sealed quartz glass reaction tube twice the length of the furnace was used to hold the UO_3 powder obtained by thermal decomposition of uranyl nitrate hexahydrate. Silicone rubber stoppers were equipped with gas inlet/outlet connections on each side of the furnace, allowing for gasses to be flowed through the entire tube. This experimental set-up allows for the tube to be completely purged with an inert gas prior to introducing hydrogen at temperatures above the auto-ignition temperature of hydrogen.

The product of the thermal decomposition of UNH was first ground into a powder using a pestle and mortar to increase the surface area to volume ratio. The powder was placed into a ceramic boat and was then placed into the hot zone of the furnace. The tube was then sealed with the silicone stoppers and a gas leak test was performed with argon. The tube was purged with argon gas until all oxygen was removed, according to the following reaction:

$$t_p = -\frac{V}{\dot{Q}} ln \left(\frac{C_f - C_p}{C_i - C_p} \right) \tag{6.7}$$

Where t_p is the purging time for the initial concentration of oxygen, C_i to reach the final concentration, C_f. C_p is the concentration of oxygen in the purging gas, whilst V is the vessel ullage volume and $\dot{Q}$ is the purge gas volumetric flow rate.

The furnace was then ramped to a working temperature of 500°C before the hydrogen was admitted at a ratio of 20% in argon. After 2 hours, the hydrogen flow was stopped and the furnace allowed to cool to room temperature with the argon flow remaining on. The product of this was a dark brown / black powder, confirmed by XRD to be uranium (IV) dioxide (a sample of the product was inserted into a 0.5 mm Ø XRD capillary and was subjected to XRD analysis). The results of the XRD can be seen in Figure 6.5.

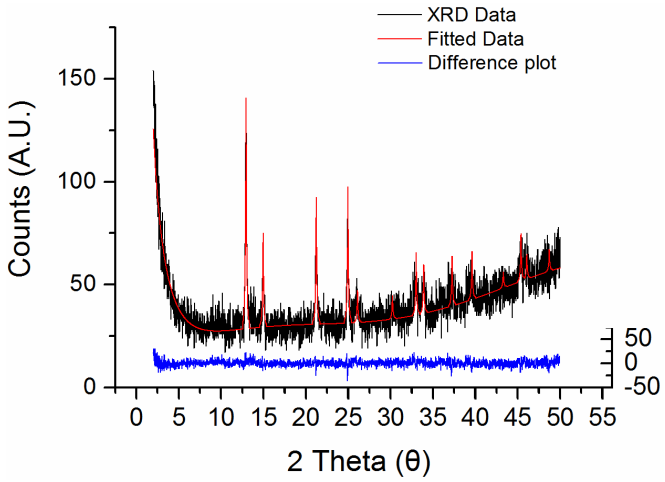

Fig. 6.5: XRD analysis of the product of hydrogen reduction. A Rietveld refinement (red) has been fitted to the raw data (black). The error of this is displayed as a difference plot (blue) below the raw and refined data.

A full Rietveld analysis of this data yielded a cubic lattice parameter of 5.465 Å. The error of this Rietveld analysis is displayed as a difference plot underneath Figure 6.5. This value for the lattice parameter is comparable to the cubic lattice parameter of 5.468 Å obtained by both Barrett *et al.* and Desgranges *et al.* [183, 184]. Moreover, there are no peaks in the raw data that are unaccounted for. This chemical characterisation is, therefore, indicative of a high purity UO_2, which supports the theory of the thermodynamic stability of UO_2 in a hydrogen atmosphere at 500°C.

6.2 Conclusion

Due to the apparent thermodynamic stability of uranium dioxide in hydrogen atmospheres, there is no danger in reducing uranium oxides below a composition of $UO_{2.0}$. Therefore, it is feasible to produce a high grade of uranium dioxide via the thermal decomposition of uranyl nitrate hexahydrate and subsequent hydrogen reduction. The product of this experimentation was a relatively coarse powder that would be applicable in the use of metallic cavity electrodes and micro-bucket electrodes, as described in Sections 4.3.1 and 4.3.2 respectively.

Chemical analysis of the product showed that pure uranium dioxide had been produced from the UNH precursor.

Chapter VII. Electrochemical Characterisation

7 Electrochemical Characterisation of UO_2|U

This chapter will expand upon the theory presented in the form of Littlewood diagrams in Chapter V. Figure 5.2 predicts that the electroreduction of uranium dioxide to uranium is feasible and presents the conditions necessary. These predictions and conditions are then used to study the electroreduction using the uranium dioxide powder that was produced in-house (as shown in Chapter VI). All electrode potentials within this chapter are reported *vs.* $Ag|Ag^+$ reference electrode (see Section 4.6).

The first section of this chapter focuses on the sweep voltammetry techniques to study the electroreduction, before looking at constant potential electrolysis. Lastly, this chapter studies the effect of the oxygen anion on the electroreduction.

7.1 Sweep Voltammetry on UO_2 electrodes

Uranium dioxide electrodes have been studied in LKE by utilising some of the electrochemical techniques described in Section 3. Both metallic cavity electrodes (MCE) and micro-bucket electrodes (MBE) have been used throughout these studies. Each pressed MCE hole allows in the region of 0.04 mg of powder to be studied, whereas MBEs provide in the region of 0.2 mg of powder. In order to gain a higher current response, a number of holes may be studied with MCEs.

7.1.1 Single Scan Cyclic Voltammogram of UO_2 Electrode

In order to study the electrochemical reduction of uranium dioxide to uranium, electrochemical techniques have been adopted. To characterise the effect of UO_2, baseline tests were first carried out on blank (or empty) MCEs.

Using the laboratory experimental set-up, blank MCEs were studied in LKE. During this investigation a sweep rate of 50 mV s^{-1} was employed. The resulting

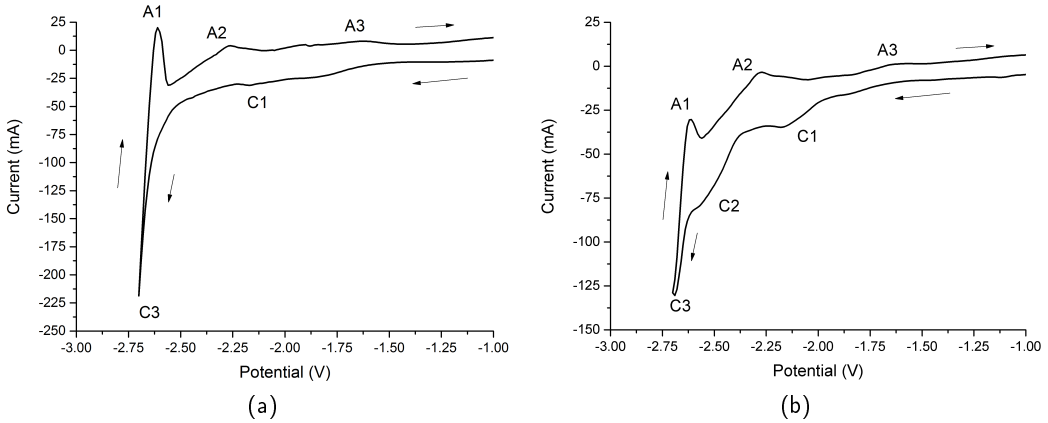

Fig. 7.1: Cyclic Voltammogram of (a) an empty MCE working electrode and (b) UO_2 MCE working electrode in LKE at 400°C. Both experiments are *vs.* the $Ag|Ag^+$ and used a graphite counter. The scan rate for both CVs was 50 mV s^{-1}. Peak C2 is missing from the CV performed on a blank MCE.

cyclic voltammogram can be observed in Figure 7.1(a). Peaks arising from the cathodic sweep are labelled with a "C" and those arising from the anodic sweep labelled "A".

Observation of the cathodic sweep in Figure 7.1(a) reveals two peaks: C1 and C3. Peak C1 is likely to be due to a reduction process occurring on the molybdenum current collector; possibly the reduction of an oxide film present on the electrode. The shape of peak C3 is very typical of electrolyte deposition; therefore, this peak is attributed to be due to the electrochemical deposition of lithium from the LKE melt (potassium is expected to plate at more negative cell voltages). Peak A1 is due to re-oxidation of the lithium (and possibly potassium) that was electroplated at peak C3. The two other peaks further along the anodic sweep, A2 and A3, are attributed to oxidation processes occurring on the current collector.

Cyclic voltammetry was also performed on a UO_2 filled MCE, resulting in the voltammogram presented in Figure 7.1(b). Comparison of Figure 7.1(b) to Figure 7.1(a) shows one obvious difference: the extra reduction peak C2. Because this reduction peak was not observed in the blank cyclic voltammetry, it is attributed

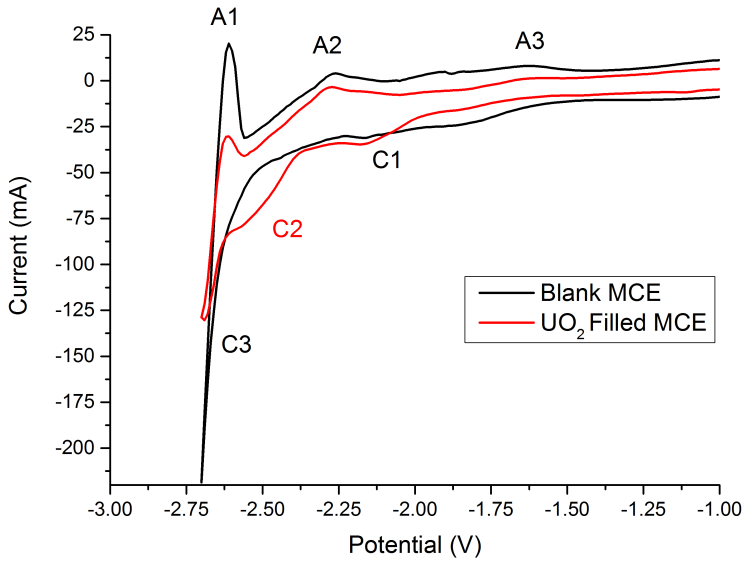

Fig. 7.2: Shows Figure 7.1(a) and Figure 7.1(b) superimposed onto one another. The peak C2 is clearly shown to be due to the addition of UO_2 powder to the working electrode.

to the electrochemical reduction of uranium dioxide to metallic uranium, as shown by Equation 7.1:

$$UO_2 + 4e^- \rightarrow U + 2O^{2-} \tag{7.1}$$

This reduction mechanism is also supported by the Littlewood diagrams presented in Section 5; that is, one reduction peak is indicative of a 4-electron process, as predicted by the Littlewood diagram. The reduction peak, C2, is in close proximity to the decomposition potential, which suggests that the $p\mathrm{O}^{2-}$ of the melt is *ca.* 6 (predicted by the Littlewood diagrams in Chapter 5). In addition, there is no observable oxidation peak on the anodic scan with the UO_2 filled working electrode. This suggests that the oxygen anions that have been liberated due to Equation 7.1 have diffused away from the boundary of the electrode, and have reacted with the counter electrode. Therefore, these oxygen anions are not available at the working electrode to re-oxidise the uranium.

Another difference in the two cyclic voltammograms is the change in peak height of A1, shown clearly in Figure 7.2. In the CV of the blank MCE, this peak is seen to be a positive current, which is expected of re-oxidation of lithium metal. However, peak A1 is seen to be negative in Figure 7.1(b). This can be explained by the following: Because the reduction of UO_2 to U is very close to the decomposition of the electrolyte, the electroreduction of uranium dioxide to metallic uranium is still occurring during lithium electroplating and dissolution. Therefore, whilst dissolution of lithium is occurring, the electrochemical reduction is too. The net current passed during these two electrochemical reactions equates to be a negative current. Additionally, lithium metal will chemically reduce UO_2 to U to via Equation 7.2

$$UO_2 + 4Li \rightarrow U + 2Li_2O \tag{7.2}$$

Li_2O is soluble in LKE and so once formed, will dissolve into the molten salt. This would, therefore, also decrease the charge passed on peak A1 due to less lithium being available to be anodically dissolved.

It is also important to note the difference in background current passed within the region of -1 to -2 V both cathodically and anodically. Because two different electrodes were used in each investigation, the immersed surface area is not equal. Thus, the difference in current passed is due to the effects of double layer capacitance: a direct function of the surface area of the electrodes.

Single scan cyclic voltammetry has been utilized to deduce that electrochemical reduction of UO_2 powder has occurred in LKE at 400°C. Due to the very negative potential at which this peak is formed suggests that it is due to the 4-electron reduction of uranium dioxide to uranium metal, supported by the predictions made by the Littlewood diagrams presented in Chapter 5.

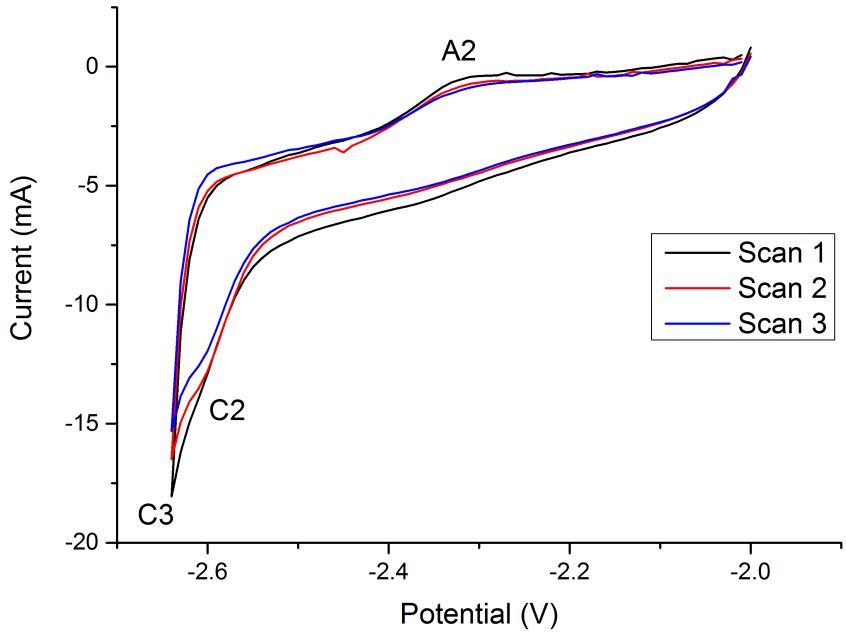

Fig. 7.3: Cyclic voltammogram of a two-hole UO_2 working electrode in LKE at 400°C. The peak current of C2 is seen to decrease as the scan number increases.

7.1.2 Multiple Scan Cyclic Voltammetry studies

Following on from the single-scan cyclic voltammograms presented in the previous subsection, this subsection investigates the effect of a number of scans on the UO_2 MBEs.

A single hole MBE filled with UO_2 was subjected to three scans within cyclic voltammetry to investigate its effect on peak C2. This technique was also employed to further investigate the absence of an oxidation peak in Figure 7.1(b). A scan rate of 10 mV s^{-1} was utilized and the results are displayed in Figure 7.3.

As the cyclic voltammetry was cycled between -2.0 V and -2.65 V, peak C1 is not easily observed (the CV begins at the same potential as peak C1). Peak A3 occurred at a potential of *ca.* -1.6 V and so is not present. Observation of peak C2 in Figure 7.3 shows that the peak current passed is reduced after each scan. In addition, there is still no observable re-oxidation peak associated with C2. This is

indicative of the O^{2-} ion diffusing to, and being consumed at, the counter electrode and not being available for re-oxidation. These phenomena may be explained by the following: The reduction of the peak current at C2 may be attributed to less material being available for electroreduction. That is, during the cathodic sweep a certain amount of UO_2 is electrochemically reduced to uranium via Equation 7.1. As there is no re-oxidation of this uranium occurring, there is less material available to be reduced on the next scan and hence the peak current is reduced.

It is also important to note the absence of peak A1. This is due to the fact that the cathodic range is less negative to that compared in Figure 7.1. Therefore, no lithium metal is expected to have electroplated onto the electrode (unless an underpotential exists). This causes the absence of the dissolution peak, A1.

To expand this investigation further, a single-hole MCE (which contains less powder than the MBE) was exposed to the same conditions but with a larger number of cycles/scans. The results of this investigation are displayed in Figure 7.4. The results seen in Figure 7.4 are similar to those shown in Figure 7.3 with a few differences.

The first is that a less negative current is passed in Figure 7.4. This is due to the fact that there is approximately half of the powder in the MCE compared to Figure 7.3. Secondly, the shape of peak A2 is different. Because this peak has been shown not to be involved with the electrochemical reduction of UO_2, this difference is not considered here.

The peak current, again, is seen to reduce with an increase in the number of scans. This further supports the theory that the UO_2 electrode is undergoing a net reduction during cyclic voltammetry. In addition, the reduction of the peak current is seen to become increasingly smaller after each scan. To compare, a reduction charge of -546 μC is passed on scan 2 compared to -51 μC on scan 10. This reduction in charge passed is indicative of the UO_2 becoming fully reduced to U metal, but could also be due to the loss of powder. This could occur due to the mechanical

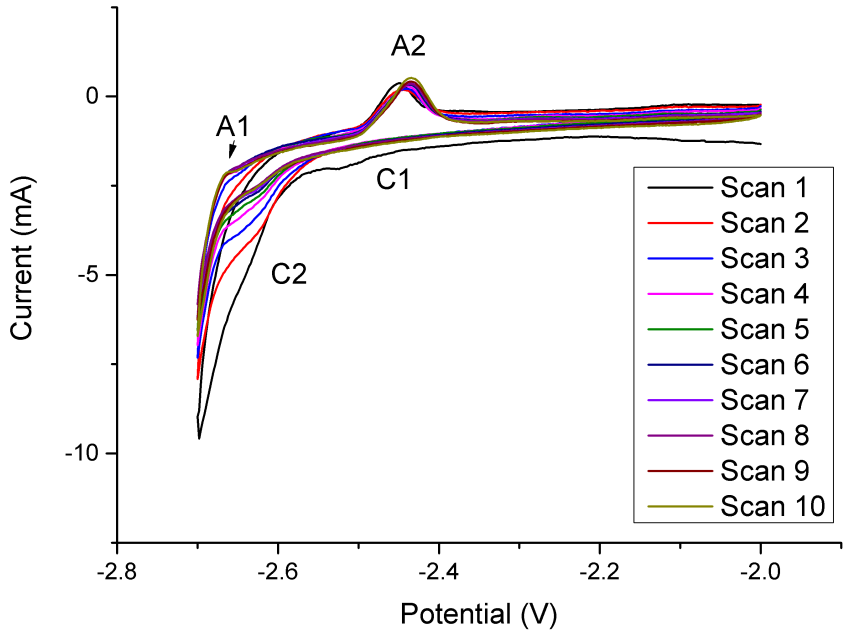

Fig. 7.4: Cyclic voltammogram of a single-hole UO_2 filled MCE working electrode in LKE at 400°C.

integrity of the electrode being compromised by the reduction in volume associated with the reduction of UO_2 to U.

Moreover, peak A1 appears to become visible after scan 9 and scan 10. The shape of the CV on these scans show a more typical shape of re-oxidation of lithium. The fact that this peak becomes more visible supports the theory that the UO_2 inside the MCE is experiencing a net reduction. This is because as the reduction proceeds towards completion (or an inhibition), the combination of negative reduction current and positive dissolution current becomes less negative. The observation of A1 towards the end of electroreduction could also be indicative of the formation of underpotentials associated with a change in the electrode surface. The peak current of C2 seems to reach a steady state value of peak current after scan 7. This is shown by the peak current of C2 in scans 7,8,9 and 10 all being approximately 2.6 mA. This is indicative of the electrode becoming fully reduced, material is being lost from the electrode (due to the volume change associated with the electroreduction)

or the electrochemical reduction is becoming inhibited. The latter could be due to a build up of oxygen anions inside the MCE preventing further electroreduction.

Faraday's law of electrolysis was, therefore, applied to the cyclic voltammograms shown in Figure 7.4. The total charge passed from scans one to seven was -2.16 mC. Using Equation 7.3, the total mass of UO_2 reduced at the electrode was calculated to be 1.5 µg.

$$m = \left(\frac{QM}{Fz}\right) \tag{7.3}$$

Therefore, it is reasonable to deduce that the reduction of the peak current is not due to the reduction proceeding to completion. Rather, it is likely to be due to inhibition of the electroreduction. This inhibition could be due to a number of phenomena: one proposed theory is that the density of TPIs within the centre of the electrode is low. This would be due to the inherent microstructure of the electrode which is a function of, for example, the porosity, tortuosity and salt penetration. Another theory is that the volume change associated with the reduction of uranium dioxide to uranium (approximately 50% reduction in volume) is causing the UO_2 to lose contact with the current collector. The uranium that is formed could also be sintering which would also reduce the volume.

To conclude this subsection, the electroreduction of peak C2 has been studied using multiple scan cyclic voltammetry. From these investigations, it is apparent that the electrochemical reduction occurs at a potential close to the decomposition potential of the melt. During successive scans, the reduction peak current of C2 is seen to decrease. This is indicative of the the UO_2 electrode experiencing a net reduction. This is also supported by the absence of an oxidation peak for re-oxidation of the reduced UO_2. This absence implies that the oxygen anion is able to diffuse away from the working electrode and be consumed at the counter electrode. Therefore, these O^{2-} ions are unavailable for re-oxidation which is responsible to the lack of an oxidation peak. Lastly, the peak current is seen to converge after a high

number of scans. This could be due to the electroreduction reaching completion.

7.2 Constant Potential Electrolysis of UO_2 Electrodes

Following on from the potential sweep investigations presented in the previous subsection, this subsection focuses on potential controlled electrolysis of uranium dioxide electrodes. Chronoamperometry, as described in Section 3.1.3, is a DC electrochemical technique whereby the potential of the cell is held at a constant value while the current response is measured. In order to study the electroreduction with this technique, the potential of the working electrode was held at the peak current potential of peak C2; -2.62 V with respect to the $Ag|Ag^+$ reference electrode.

7.2.1 Constant Potential Electrolysis at Peak C2

Using the optical laboratory set-up, multiple MBE and MCE working electrodes were immersed into the cell and a reduction potential corresponding to peak C2 was applied. The chronoamperomogram of a UO_2 MBE (after baseline subtraction to account for double layer capacitance effects of the current collector assembly) may be observed in Figure 7.5(a). For reference, another chronoamperomogram is presented in Figure 7.5(b) showing the current decay to zero after *ca.* 350 seconds. It can be seen that the current passed begins to increase until about 100 seconds into the electrolysis after which the reduction current begins to decrease towards zero. This is indicative of an electrochemical reduction approaching completion; while the reactant is being converted to product, there is less reactant and hence the reduction current decreases.

By integrating the current passed over time, it is calculated that a total of 1.04 C were passed during electrolysis. By utilizing Faraday's law of electrolysis, the total, theoretical, mass of UO_2 which would be reduced at the electrode equates to 0.728 mg of UO_2. Assuming a 15% porosity of the UO_2 powder (see Section 8.4) in the MBE, an approximate total of *ca.* 0.12 mg of UO_2 would be present. Therefore,

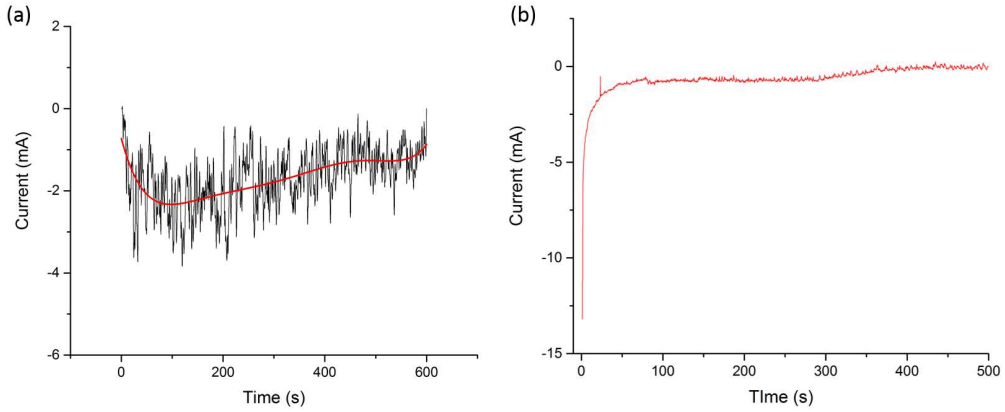

Fig. 7.5: (a) Chronoamperomogram of the constant potential electrolysis (-2.57 V) of a UO_2 filled MBE in LKE (black) with a polynomial fit (red) to clearly show the reduction of the average current. (b) shows chronoamperometry performed on a separate sample resulting in a fully reduced sample.

theoretically, the powder inside the MCE should have been completely reduced. Although the current efficiency was not possible to calculate for this process (due to the difficulty in ensuring all of the powder remains inside the MCE/MBE during electrolysis) the fact that such a significantly higher current was passed assumes a relatively low current efficiency for the process.

Figure 7.6 shows SEM micrographs of the MBE that was the result of the chronoamperomogram presented in Figure 7.5(a) (the particles seen towards the lower right of Figure 7.5(a) are silicon carbide particles left over from sample preparation). Specifically, Figures 7.5(a) and (b) appear to posses the same "coral-like" structure to that shown by Kurata *et al.* during the reduction of MOX fuels [64]. The presence of this coral-like structure provides strong evidence into the reduction of uranium dioxide to uranium metal. The formation of this structure is attributed to the volume change associated with the reduction from oxide to metal: uranium dioxide has a molar volume of 24.61 cm^3 mol^{-1} compared to 12.46 cm^3 mol^{-1} of uranium metal, at room temperature. This reduction in volume would inherently produce porosity within the microstructure of the electrode, producing the coral-like

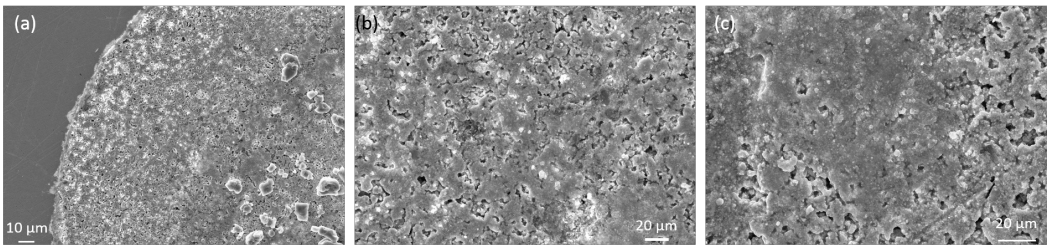

Fig. 7.6: (a) SEM micrograph of the MBE sample reduced using the chronoamperomogram presented in Figure 7.5, (b) zoomed region showing a coral-like structure and (c) showing a dense and coral-like structure.

structure.

Figure 7.6(c) depicts the structure towards the centre of the MBE electrode which shows a small dense region. This dense region is likely to be unreduced uranium dioxide. The electroreduction is dependent on the triple phase interlines which, in the case of MBE/MCE electrodes, propagates from the current collector (which located on the outer edge of the powder) inwards. This results in the centre of the electrode being the last part of the electrode that would undergo reduction.

Because the actual charge passed during electrolysis was much greater than the theoretical charge passed, the electrochemical reduction of this material seems to have a low current efficiency. However, due to the small quantities of powder used in the electrodes, determination of the actual current efficiency is not possible. The presence of this dense phase suggests that the electroreduction is being impeded. The most likely cause of this is due to the build up of O^{2-} ions in the electrode. As mentioned in Chapter 5, a local build up of O^{2-} ions may cause the potential for electroreduction to be dynamic, which would affect the constant potential electrolysis. In extreme cases a change in the O^{2-} ion concentration could completely inhibit further electroreduction. This phenomena would be accelerated towards the centre of the electrode as there would be a higher local concentration of O^{2-} ions liberated at the centre of the electrode compared to the outer edges of the electrode.

7.3 The Effect of O^{2-} ions

As mentioned in Chapter 5, the oxygen anion may have a significant effect on the electroreduction of uranium dioxide to uranium in LKE. The Littlewood diagram presented in Figure 5.2 predicts that the pO^{2-} of the melt must be controlled to higher values than 6 in order for the electroreduction of UO_2 to U to be more favourable than cathodic decomposition of the molten salt.

Because the activity of O^{2-} ions in the melt is predicted to play a significant role in the electrochemical reduction, proper maintenance of the molten salt must be adhered to: in order to avoid oxygen entering into the system. Moreover, the local pO^{2-} level within the electrode may differ from that of the bulk of the electrode. This would occur if the diffusion of O^{2-} ions out of the electrode were to be impeded.

Within this subsection, the effect of the bulk activity of O^{2-} ions will be investigated. The main focus of this investigation is to deduce the effect of O^{2-} ions on the reduction peak C2 shown in Figure 7.1(b).

7.3.1 Dissolution of Na_2CO_3

Within the context of this investigation, sodium carbonate has been used as a source of O^{2-} ions. Sodium carbonate is known to dissolve and fully dissociate, under specific conditions, providing a source of O^{2-} ions. The dissociation of this compound could proceed via a sodium oxide intermediate or via the equilibrium between the oxygen anion and carbonate anion [185, 186]:

$$Na_2CO_3 \rightarrow CO_2 + Na_2O \rightarrow 2Na^+ + O^{2-} \tag{7.4}$$

$$Na_2CO_3 \rightarrow 2Na^+ + CO_3^{2-} \rightarrow CO_2 + O^{2-} \tag{7.5}$$

By inspection of Equations 7.4 and 7.5, both mechanisms provide the production of sodium cations, oxygen anions and carbon dioxide. It should also be noted that for each mole of sodium carbonate added one mole of oxygen anions is produced via dissociation, which is driven by keeping the partial pressure of CO_2 low (achieved by having a flow of inert gas through the cell). Therefore, by adding known quantities of sodium carbonate to the bulk molten salt, the change in $p\mathrm{O}^{2-}$ of the salt may be accurately determined.

7.3.2 $p\mathrm{O}^{2-}$ Indicator electrode calibration

Measurement of the $p\mathrm{O}^{2-}$ of a molten salt system may be realised with the use of a $p\mathrm{O}^{2-}$ indicator electrode, as described in Section 4.7. The main advantage of this technique is the ability to measure the activity of oxygen anions *in situ*. Employment of a $p\mathrm{O}^{2-}$ indicator electrode is possible for such measurements to be taken. Calibration of the device is essential, in order to ensure it's Nerstian response and to deduce the value E^0.

Because the potential $p\mathrm{O}^{2-}$ indicator electrode is affected solely by changes in the activity of oxygen anions, the Nernst equation for this electrode may be written as:

$$E = E^0 - \frac{2.303RT}{2F} log\left(a_{O^{2-}}\right) \tag{7.6}$$

Calibration of the $p\mathrm{O}^{2-}$ indicator electrode may, therefore, be achieved by changing the activity of oxygen anions and measuring the change in potential. E^0 may be deduced by saturating the molten salt with oxygen anions. For comparison, the theoretical slope of Equation 7.6 may be computed. At 400°C this value is calculated to be equal to 0.0667.

In order to calibrate the $p\mathrm{O}^{2-}$ indicator electrode experimentally, a $p\mathrm{O}^{2-}$ indicator electrode was inserted into the laboratory experimental set-up, as explained in Section 4.1. The potential of the $p\mathrm{O}^{2-}$ indicator electrode was left to stabilise *vs.*

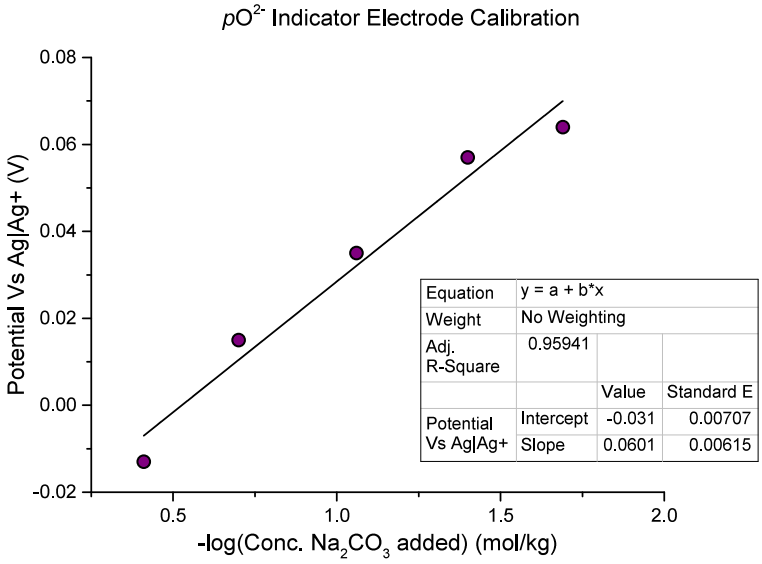

Fig. 7.7: A graph showing the potential of the pO^{2-} indicator electrode *vs.* the negative logarithm of the total concentration of Na_2CO_3 added to the molten salt.

the Ag|AgCl reference electrode for an hour before the addition of known quantities of sodium carbonate. Again, the potential of the pO^{2-} indicator electrode vs. Ag|AgCl was left to stabilize for an hour and the potential recorded. This procedure was repeated until saturation was achieved (reaching the saturation of Na_2CO_3 could be visibly seen using the optical access furnace) in order for the value of E^0 to be deduced.

A plot of potential difference *vs.* the negative logarithm of the added concentration of O^{2-} ions was then produced and is displayed in Figure 7.7. Observation of Figure 7.7 depicts the linear, Nerstian behaviour of the pO^{2-} indicator electrode, as expected. A line of best fit was added to the data points in order to deduce the gradient. Experimentally this gradient is calculated to be 0.0601 (see Figure 7.7), which is in good agreement with the thermodynamic prediction of 0.067.

The potential of the pO^{2-} indicator electrode was also measured during potential stabilization after saturation of oxygen anions was achieved. Figure 7.8 depicts the

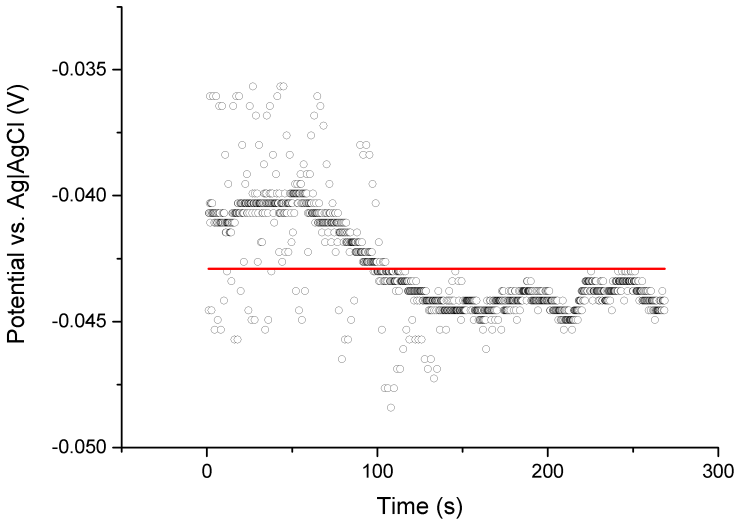

Fig. 7.8: A graph showing the potential of the pO^{2-} indicator electrode *vs.* time after saturation of the molten salt with oxygen anions.

last three minutes of this potential stabilization. Observation of this graph shows the potential oscillates around an average potential. This average potential was extracted to be -0.044 V by averaging data points taken in the last 20 minutes of potential stabilization.

One will notice that the E^0 value calculated from Figure 7.8 is different from the y-intercept calculated in Figure 7.7. This is due to the fact that the initial pO^{2-} of the salt is unknown. Therefore the y-intercept of this value is not equal to the standard cell potential of the pO^{2-} indicator electrode. However, because the pO^{2-} indicator electrode exhibits Nerstian behaviour, the gradient extracted from this study is still valid, provided the same temperature is adhered to.

To conclude, the pO^{2-} indicator electrode has been successfully calibrated and has been shown to exhibit Nernstian behaviour. The gradient of the response agrees with the theoretical value and the value of E^0 has been derived. Therefore, in order to deduce the pO^{2-} of the molten salt, Equation 7.7 may be used:

$$pO^{2-} = \frac{E + 0.044}{0.06} \tag{7.7}$$

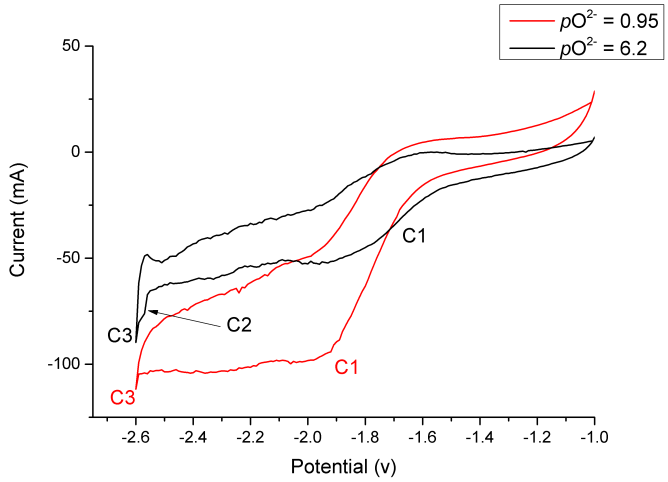

Fig. 7.9: Cyclic voltammograms of UO_2 MBEs in LKE at different value of pO^{2-}. A sweep rate of 100 mV s^{-1} was used.

7.3.3 Effect of pO^{2-} on the reduction

Due to the successful calibration of the pO^{2-} indicator electrode in Section 7.3.2, the pO^{2-} of a molten salt cell can be altered to investigate its effect on the electroreduction of UO_2 to metallic U. Referring back to Chapter 5, Figure 5.2 indicates the electroreduction may only occur at levels of pO^{2-} greater than 6. Therefore, this subsection investigates the behaviour of the electrochemical reduction peak C2, with a change in the activity of O^{2-} ions.

The laboratory set-up as explained in Section 4.1 was used for these studies. Both MCEs and MBEs were used as working electrodes. Sodium carbonate was also used as a source of O^{2-} ions. To begin with, the electrochemical cell was heated to the reaction temperature and a UO_2 working electrode was immersed into the molten salt. A cyclic voltammogram was performed, resulting in the voltammogram displayed in Figure 7.9

Figure 7.9 shows two cyclic voltammograms. These were taken at two different values of pO^{2-}. At a pO^{2-} value of 6.2, the cyclic voltammogram is very similar to the CV shown in Figure 7.1(b), including the reduction peak C2 which is attributed

to the electroreduction of UO_2 to metallic U. It should be noted that the anodic scan labels have been omitted from Figure 7.9. After this CV was performed, sodium carbonate was inserted into the molten salt. The melt was left to stabilise for an hour and the pO^{2-} was measured to be 0.95. After which, cyclic voltammograms of various MBEs and MCEs were performed. This resulted in no observable C2 reduction peak, as highlighted by the red CV in Figure 7.9.

The absence of peak C2 at a pO^{2-} value of 0.95 supports the thermodynamic predictions of the Littlewood diagram presented in Figure 5.2. Because the activity of oxygen anions has increased, the standard potential for the UO_2|U couple has become more negative. This can be seen in the form of the Nernst equation for the electrochemical reduction of Equation 7.1:

$$E = E^0 + \frac{RT}{nF} ln \left(\frac{a^{UO_2}}{a^U \, a^{O^{2-}}} \right) \tag{7.8}$$

As both UO_2 and U are insoluble in LKE, the activities are unity. The activity of O^{2-} ions is high after the addition of sodium carbonate and so the reduction potential becomes more negative than the cathodic decomposition of the molten salt electrolyte.

It should also be noted that the electrochemical wave seen in Figure 7.9 has been attributed to reduction and oxidation of the molybdenum current collector, as mentioned in Section 7.1.1.

7.4 Conclusion

This chapter of the thesis has investigated the electrochemical characterisation of the electroreduction of UO_2 to U in LKE at 400°C. Electrochemical sweep voltammetry techniques have all observed a single reduction peak suggesting that the electroreduction occurs via a single, 4-electron transfer, process. In theory, however, this could be the summation of two 2-electron processes, proceeding via the electro-

chemical reduction pathway:Constant potential electrolysis has also been used to reduce a number of MBE/MCE electrodes which have resulted in a coral-like structure to form, similar to that observed by Kurata *et al.*, which is likely to be due to the reduction in volume associated with the reduction from UO_2 to U.

The electrochemical reduction of UO_2 to metallic uranium has been shown to be very dependent on the activity of O^{2-} ions in the bulk salt. This is due to the fact that the reduction potential is a function of the activity of oxygen anions. By increasing the activity of oxygen anions to levels near saturation, the cell potential for the UO_2|U couple becomes less negative than the cathodic decomposition potential of the molten salt. This results in the inability to reduce UO_2 to U. This effect was thermodynamically predicted in Chapter 5, which showed the reduction potential become more negative than the cathodic decomposition potential. Although this study was performed in the bulk salt, the results suggest that this effect could also occur on a more local level; specifically, within the UO_2 microstructure. If the microstructure of the UO_2 electrode inhibits the diffusion of O^{2-} ions out of the microstructure, this could cause a local increase in the activity of O^{2-} ions. This would have negative consequences on the electroreduction, particularly if the reduction is being performed at a static reduction potential.

Chapter VIII. Advanced Material Characterisation

Sections of this work have been peer reviewed and published in the Journal of Nuclear Materials (L.D. Brown, R. Abdulaziz, R. Jervis, V. Bharath, R. Attwood, C. Reinhard, L.D. Connor, S.J.R. Simons, D. Inman, D.J.L. Brett, P.R. Shearing, *Following the electroreduction of uranium dioxide to uranium in LiCl-KCl eutectic in situ using synchrotron radiation.* Journal of Nuclear Materials (2015), *In press,* 10.1016/j.jnucmat.2015.04.037)

8 Advanced Material Characterisation

Following on from the electrochemical characterisation of the UO_2-U-LKE system in Chapter VII, this chapter focuses on material characterisation of the system. That is, advanced characterisation techniques have been utilized to provide strong evidence to support the electrochemical based analysis. To begin with, is an investigation on peak C2 on the cyclic voltammograms presented in Section 7.1.1 using *in situ* energy dispersive X-ray diffraction (EDXD). The main advantage of using such an *in situ* technique is the fact that it allows for the chemical characterisation of samples during chemical change. This, therefore, allows for one to investigate phenomena such as the reaction pathway.

Secondly, the effect of the microstructure on the electrochemical reduction of UO_2 is investigated. Because the microstructure of the electrodes are inherently a three-dimensional property, the microstructure is studied in three-dimensions to allow for true microstructural information to be extracted. The use of FIB tomography and X-ray computed tomography have both been utilized to provide an in-depth analysis of the microstructural evolution.

8.1 *In Situ* X-ray Diffraction

Littlewood diagrams serve as a useful tool for predicting metal-metal oxide-molten salt systems and have been widely applied for nuclear species in molten salt systems [33, 40, 42, 187]. The Littlewood diagrams predict the electroreduction of UO_2 to U to be a single, 4-electron-step, process, as shown in Figure 5.2. The electrochemical characterisation of peak C2 in Figure 7.1 also supports this. However, to date there is limited experimental evidence to support this – indeed experiments tracking the reaction mechanism for the molten salt electroreduction of TiO_2 to Ti (the FFC Cambridge process) show a departure from the theory [21]. Although the reduction of TiO_2 to Ti metal using molten salts has recently been extensively investigated (see Section 2.1), *ex situ* investigations led to much debate of the actual electrochemical reduction pathway, which seemed to differ from the thermodynamic predictions.

It was only after an *in situ* investigation, using white beam synchrotron radiation, that a detailed insight into the true electrochemical reduction pathway was obtained [21]. Within this subsection, an investigation to deduce the electrochemical reduction pathway of uranium dioxide to metallic uranium by combining electrochemical studies with *in situ* phase characterisation using synchrotron radiation is detailed.

8.1.1 UO_2 Sample Identification

The uranium dioxide precursor was first analysed using powder diffraction on a lab based X-ray diffractometer (STADI P, STOE & Cie GmbH). The powder X-ray diffraction pattern can be seen in Figure 8.1. A full Rietveld analysis of this data yielded a cubic lattice parameter of 5.465 Å. The error of this Rietveld analysis is displayed as a difference plot underneath Figure 8.1(a). This value for the lattice parameter is comparable to the cubic lattice parameter of 5.468 Å obtained by both Barrett *et al.* and Desgranges *et al.* [183, 184]. In order to obtain the energies

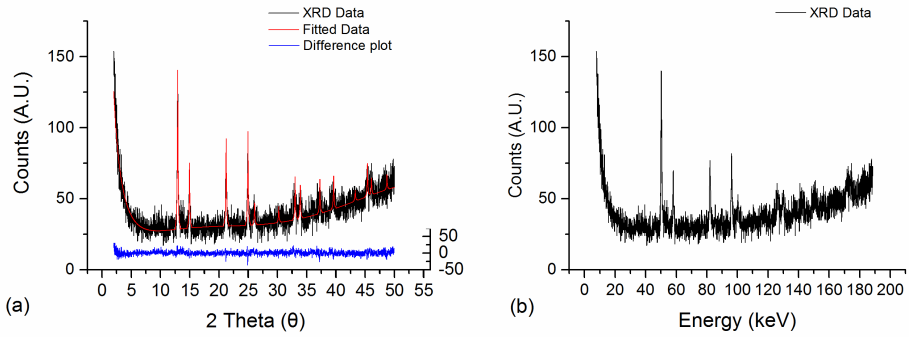

Fig. 8.1: X-ray diffractogram of UO_2 powder showing: (a) the measured powder diffraction pattern (black), the Rietveld fit (red) and the difference plot (blue). The difference plot is the difference between the fitted data points and the observed data points. (b) shows the raw data plot after conversion, as a function of energy.

Crystal Plane (h k l)	d-space (Å)	Diffraction angle (2 ϑ)	X-ray Energy (keV)
111	3.1	12.96	20.14
002	2.72	14.96	58.12
022	1.93	21.22	82.10
113	1.6	24.95	96.17

Tab. 8.1: UO_2 X-ray diffraction angles and the calculated X-ray energies for the crystal planes shown.

at which diffraction peaks for UO_2 would be expected in the EDXD diffractogram, the XRD data was converted from a function of 2-theta to a function of energy using Bragg's law with a fixed angle of 4.5°. The X-ray energies for the four most prominent peak intensities of uranium dioxide were extracted and are tabulated in Table 8.1. EDXD data of an empty MCE working electrode and one packed with UO_2 were measured using the same beam line set-up to validate the peak intensities calculated and to confirm the beam placement on the small MCE sample. Figure 8.2 shows EDXD diffractograms of an empty MCE (a) and one filled with UO_2 (b).

Referring back to Table 8.1, one can see that the expected peaks for UO_2 are missing from Figure 8.2(a), as expected. However, peaks are present at 49.61, 57.37, 81.05 and 95.05 keV when the MCE was loaded with UO_2 powder. The difference

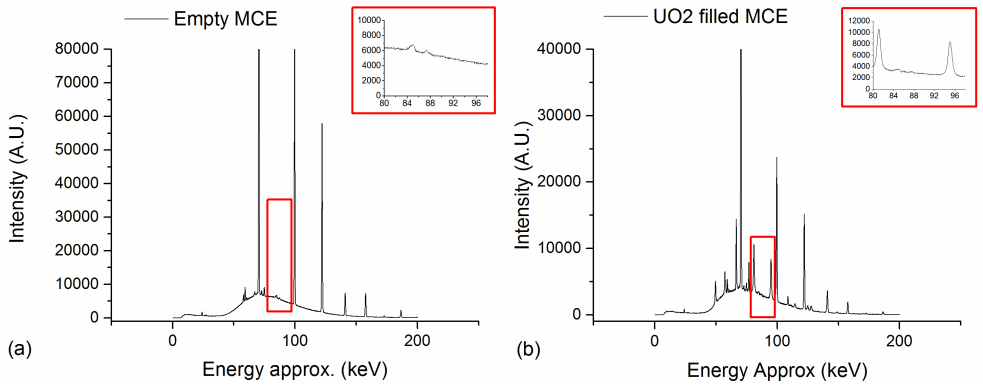

Fig. 8.2: EDXD diffractograms of (a) an empty MCE and (b) a UO_2 filled MCE. The insets in each figure show, in detail, the region between 80 and 98 keV at which peaks for UO_2 were expected.

between these values and those calculated in Table 8.1 are due to changes in the d-spacing caused by the difference in temperature in which both data sets were collected. It should be noted that there are tungsten fluorescence peaks at W Kα1 = 58.00, W Kα2 = 59.33 and W Kβ1 = 67.24 keV (due to tungsten instrument shielding) which overlap with the (0 0 2) UO_2 peak at 58.12 keV. Also, lead fluorescence peaks are present at Pb Kα1 = 74.98, Pb Kα2 = 72.81 and Pb Kβ1 = 84.87 keV which are, again, due to shielding of instruments. This phase identification allowed for rapid recognition of UO_2 powder during alignment in the Z direction.

8.1.2 Electrochemical Characterisation on the Beamline

Pre-electrolysis of the molten salt electrolyte was performed to remove contaminants: a potential 200 mV more positive than the cathodic electrolyte decomposition potential was maintained for 2 hours prior to all electrochemical measurements. Subsequently, the UO_2 MCE was inserted into the molten salt and was made the cathode. Cyclic voltammetry was performed between -1.9 V and -2.6 V, the onset potential of decomposition of the molten salt, with respect to the saturated Cl^- Ag|AgCl reference electrode. Figure 8.3 shows a cyclic voltammogram of the UO_2 MCE in LKE and contains four peaks labelled C2, C3, A2 and A2'. Peak C1, as

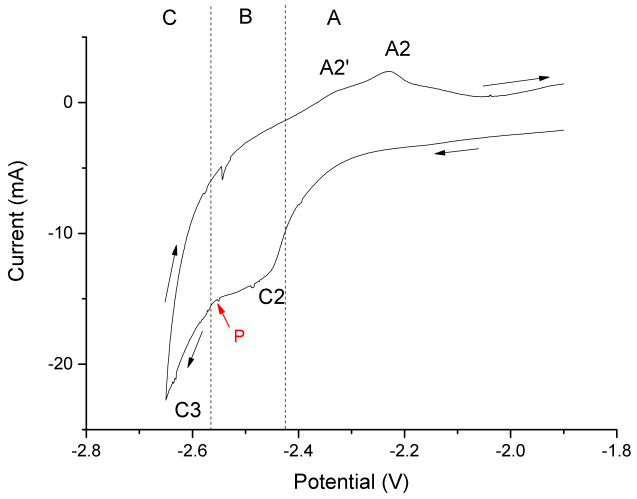

Fig. 8.3: Cyclic voltammogram of a UO_2 filled MCE working electrode at 10 mV/s. The CV has been divided into three regions, moving in the negative potential direction: Region A shows the current response before the electrochemical reduction; region B defines the potential range for the electrochemical reduction and Region C depicts potentials more negative of the cathodic decomposition potential of the molten salt. Point P defines the inflection current.

defined in Figure 7.1 in Section 7.1. The current has not been normalised to current density due to difficulties in efficiently assessing the immersed surface area in the cell for different electrodes. The electroreduction peak potential is close to the onset potential of lithium decomposition of the molten salt; therefore the inflection point (P) is taken as the point of maximum current. Peak C2 - on the cathodic sweep - shows the peak for the electrochemical reduction of uranium dioxide to metallic uranium, as shown in Section 7.1.

Peak A2' was previously not observed in cyclic voltammograms displayed in previous sections. It is thought that this peak could be due to the re-oxidation of uranium to an oxide of uranium. The charge passed at A2' is less than that at peak C2: 18.9 mC was passed on the cathodic sweep compared to 1.3 mC on the anodic sweep. This discrepancy is thought to be due to the fact that some of the oxygen anions that were liberated during the electroreduction reaction have diffused away from the electrode and are not readily available at the MCE again for oxidation on

the anodic sweep, resulting in a net reduction of the UO_2 electrode. Peak A2 is attributed to an oxidation of the molybdenum current collector. Again, the absence of peak A1 is due to the fact that the cathodic potential limit does not permit a large amount of lithium metal to plate onto the electrode and therefore the dissolution peak is unobservable.

8.1.3 *In situ* EDXD characterisation of Peak C2

Energy dispersive X-ray diffraction patterns were taken of the UO_2 working electrode before, during and after all electrochemical measurements at 450°C. Linear sweep voltammetry (LSV) was used for electrochemical reduction to allow for the electrochemical pathway to be deduced at multiple potentials. A LSV sweep rate of 0.1 mV s^{-1} was applied from a potential of -2.41 V to -2.57 V with respect to the Ag|AgCl reference. This slow sweep rate was utilized to help capture processes during the EDXD measurements. EDXD data were acquired during the entire LSV process with an integration time of 60 seconds per scan point. Analyses of the obtained diffraction patterns clearly show the electrochemical reduction of uranium dioxide to uranium in lithium chloride potassium chloride eutectic. This electroreduction appears to occur via a single, 4-electron, step and no intermediate products were observed. Uranium metal possesses three crystalline modifications; α, β and γ [188]. The α phase is stable up to a temperature of 660 °C, the β phase is stable from 660-760 °C whilst the γ phase is stable from 760 to 1312 °C - its melting point. Le Bail refinement proved that the uranium phase formed during the electroreduction was α-uranium, as expected.

Figure 8.4(a) shows the peak intensity of different crystal planes of the uranium dioxide phase. From -2.41 V to -2.43 V (region A in Figure 8.3), no electrochemical reaction occurs, as expected, and so there is no change in peak intensity. However, when the working electrode reaches a potential of -2.51 V (region B in Figure 8.3) a reduction in the peak intensity of uranium dioxide for all crystal planes is observed.

Concurrently, a signal for uranium metal is recorded (Figure 8.4(b)), in accordance with Equation 7.1. The reduction in peak intensity of UO_2 and sudden increase in U peak intensity can be easily observed in Figure 8.4(c). As the potential becomes more cathodic, the peak intensities for UO_2 continue to reduce and those for uranium – specifically the 002 plane – continue to increase. This is indicative of the electrochemical reduction as the potential is within the UO_2|U electroreduction regime, as shown by the Littlewood diagrams in Figure 5.2. The rate of decrease of the peak intensities seems to decrease from within the potential range of -2.53 to -2.56 V as compared to the potential range of -2.51 to -2.53 V. It is expected that the reduction is curtailed at this point due to an increase in the concentration of O^{2-} ions in the melt, formed as a by-product of the reduction of UO_2 . Due to the working electrode being positioned in the well of the aluminium cell, the transport of oxygen anions from cathode to anode would be more impeded compared to the laboratory set-up in which the anode and cathode are in close proximity. For example, assume that half (0.02 mg) of the UO_2 inside the MCE was electrochemically reduced; this would relate to a molality in the molten salt of 1E-04 mol kg^{-1} of O^{2-} ions liberated during electroreduction. If this concentration of oxygen anions was not consumed at the counter electrode (as no O^{2-} ions are available to react the potential of the counter electrode is adjusted by the potentiostat to evolve Cl_2 gas, ensuring two half-cell reactions occur) then this would result in a pO^{2-} value of 3.35. The electrochemical reduction is predicted to not be possible at this level of pO^{2-} (see Figure 5.2) and could explain the discontinuation of electrochemical reduction [187]. The geometry of the microstructure of the electrode could play an important role in this. If the microstructure contains a highly tortuous pore phase then this would impede the transport of O^{2-} ions from the cathode to the anode, affecting the local activity of oxide ions and, thus, the level of pO^{2-}.

Table 8.2 shows the calculated lattice parameters for both UO_2 (before electroreduction) and α-uranium deduced from the Le Bail refinement analysis of the EDXD

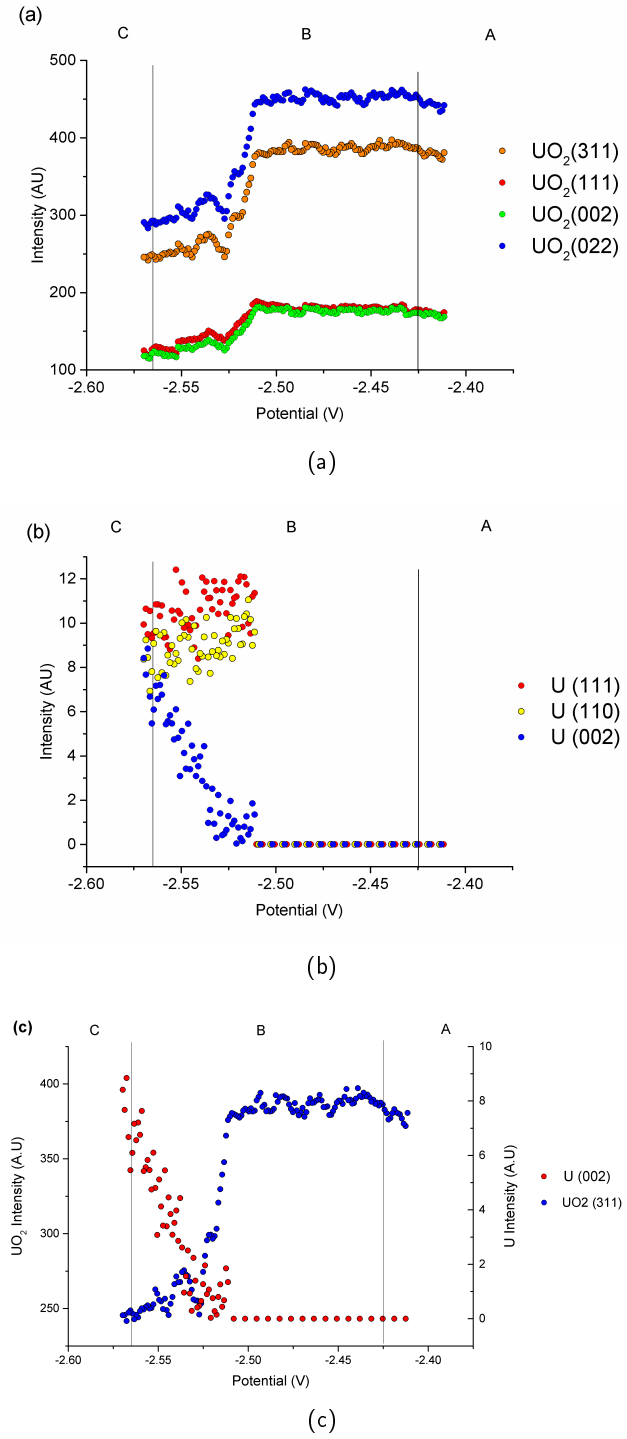

Fig. 8.4: (a) Peak intensities versus potential (0.1 mV s^{-1}) for uranium dioxide, (b) α-uranium and (c) U (002) and UO_2 (311) planes. Regions A, B and C (as defined on Fig. 8.3) are shown on all graphs.

	Calculated lattice parameter {abc} at 703k (Å)	Reference lattice parameter {abc} at 298K	Calculated cell volume at 703K (Å^3)	Reference cell volume at 398K (Å^3)
UO_2	5.488	5.568 [184]	165.32	163.49 [184]
α-U	{2.88 5.88 4.98}	{2.854 5.87 4.955} [183]	84.33	83.01 [183]

Tab. 8.2: Calculated and reference values for the lattice parameters and cell volumes for uranium dioxide and uranium

data. The difference in our calculated lattice parameters and derived cell volumes to those referenced in Table 8.2 are attributed to the difference in temperature at which these diffraction patterns were gathered: the thermal expansion of UO_2 may be described by the Equation 8.1 [189].

$$L = L_{273}\left(9.9734x10^{-1} + 1.179x10^{-6}(T) - 2.705x10^{-10}(T) + 4.391x10^{-13}(T)\right) \tag{8.1}$$

Equation 8.1 predicts a thermal expansion of 0.4% for UO_2 at 703 K compared to that at 273 K. This is comparable to the 0.36% change seen in Table 8.2 for the lattice parameter for UO_2.

To conclude, the electrochemical reduction of uranium dioxide to uranium metal has been studied in a lithium chloride-potassium chloride eutectic molten salt at 450°C. Both electrochemical and synchrotron X-ray techniques have been utilized to deduce the electrochemical reduction potential, mechanism and reduction pathway. The electrochemical reduction of uranium dioxide to uranium metal seems to occur in a single, 4-electron-step, process; indicated by a single reduction peak (C2) in the cyclic voltammograms presented in Section 7.1 and from the Littlewood diagrams presented in Section 5. Moreover, the the exclusion of any other phases in the EDXD data provides great evidence that the electroreduction is in fact a single, 4-electron step, process. Lastly, the electrochemical reduction potential of the UO_2|U couple

is seems to be dependent on the activity of oxide ion existing within the melt. This was indicated by the inhibition of the electrochemical reduction during electrolysis. Theoretically, if the $p\mathrm{O}^{2-}$ of the molten salt remained constant, the electroreduction of UO_2 should have been observed to continue. The microstructure of the electrode may have contributed to this phenomenon and is therefore investigated later in this chapter.

8.2 Direct Oxide Reduction

A fresh MCE was also exposed to potentials more negative than the decomposition potential of the LKE electrolyte. Due to this potential, Li^+ would be reduced to Li metal via Equation 8.2.

$$Li^+ + e^- \rightarrow Li \tag{8.2}$$

Lithium metal is known to chemically reduce uranium dioxide to uranium metal via the following equation:

$$UO_2 + 4Li \rightarrow U + 2Li_2O \tag{8.3}$$

EDXD measurements were obtained before and during lithium reduction. The peak intensities for uranium and uranium dioxide are presented in Figure 8.5.

Figure 8.5 shows that the peak intensities for the α-uranium phases start at zero while peaks for the uranium dioxide are all observable. After *ca.* 700 seconds, the cell is subjected to potentials more negative than the decomposition potential of the LKE electrolyte for ten seconds. At this point, Li metal would be electrochemically plated onto the UO_2 working electrode. The peak intensities for α-uranium all begin to increase simultaneously as the peak intensities for uranium dioxide begin to decrease after Li has been plated onto the electrode. This observation is due to Equation 8.3.

In addition, the peak intensity for each observable plane for uranium dioxide are all seen to fall to a value of zero. This is indicative of the chemical reaction

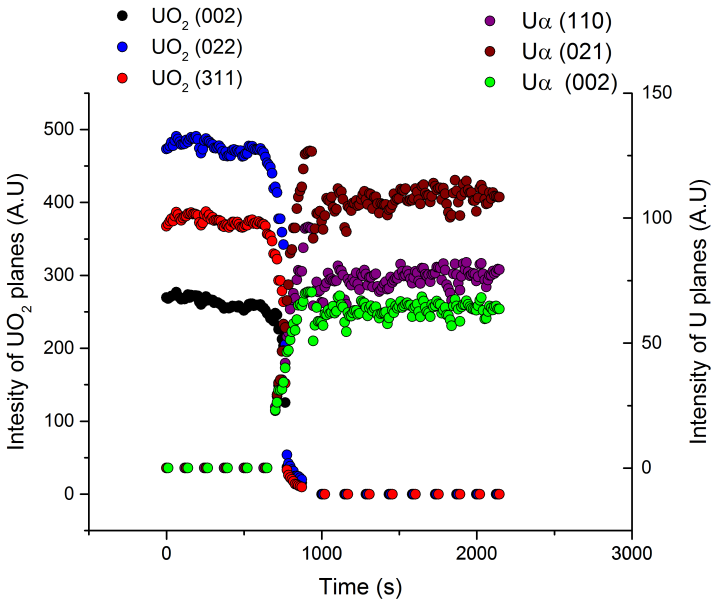

Fig. 8.5: Peak intensities for uranium dioxide and uranium before and during the Li^+ reduction process

proceeding to completion. The direct oxide reduction process is usually performed in a LiCl molten salt containing between 1-2% of Li_2O [63, 190]. However, the direct oxide reduction has been shown to be possible in a LiCl-KCl eutectic operating at 450°C. In the context of pyroprocessing, this oxide reduction process could potentially be performed inside the electrorefiner unit, negating the use of the direct oxide reduction unit.

8.3 *In Situ* Neutron Diffraction

An alternative *in situ* characterisation technique to X-ray diffraction is neutron scattering. Indeed, neutron diffraction has been used to investigate the structure of uranium-based compounds instead of X-ray diffraction [191-193]. Amongst others, these studies highlight the pros and cons of each diffraction technique and may be used to understand how each technique may compliment the other.

This subsection focuses on the *in situ* neutron diffraction characterisation of the

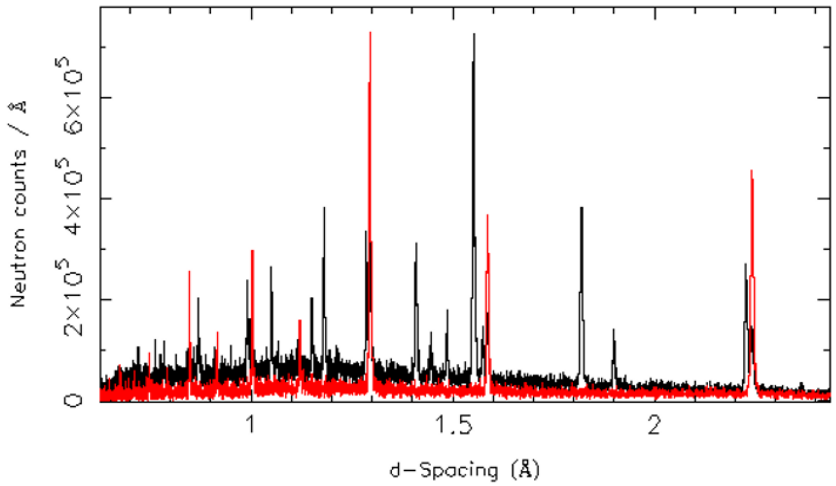

Fig. 8.6: Diffractogram of a tungsten rod inside the *in situ* cell, shown in red, and after the addition of LiCl and KCl powders, shown in black

electrochemical reduction of uranium dioxide to uranium metal in LKE.

8.3.1 Preliminary studies on the ENGIN-X beamline

Prior to the *in situ* X-ray diffraction investigation presented in Section 8.1 and the neutron diffraction study presented in this section, a preliminary neutron diffraction investigation was first undertaken on the ENGIN-X beam line at ISIS neutron source, UK. The aim of this experiment was to deduce the feasibility of the experimental set-up described in Section 4.2.6. Within the preliminary experimentation, a tungsten rod (acting as a surrogate to the working electrode) was placed inside the *in situ* cell at room temperature and a neutron diffractogram was taken. After which, a eutectic mixture of LiCl and KCl powders was poured into the cell and the experiment repeated. The results may be observed in Figure 8.6. From this, it is clear that there is no significant effect on the signal-to-noise ratio from the extra attenuation due to the addition of LiCl and KCl. Although there are peak shifts, all peaks present in the tungsten-only scan (red) are all present after the addition of the LiCl and KCl powders (red). The additional peaks observed in the second scan are attributed to the addition of LiCl and KCl.

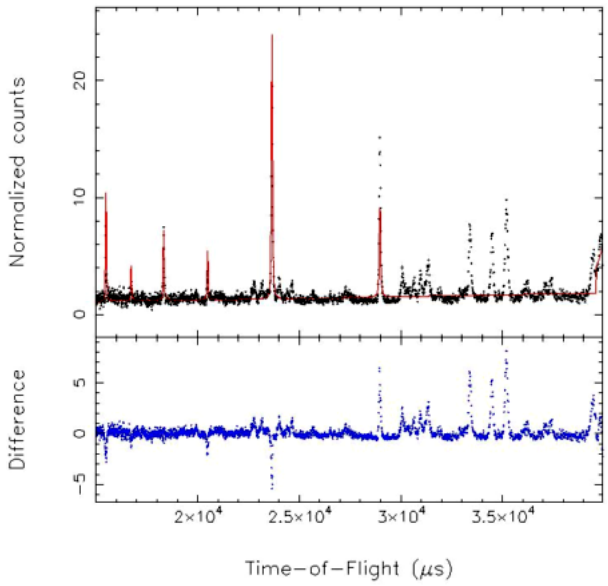

Fig. 8.7: Diffractogram of a 200 μm WO_3 thin film coated on a tungsten rod (black). The tungsten phase has been fitted to the tungsten metal phase (red). The oxide phase fitting has been omitted. A difference plot of the fitted data is also shown below the diffractogram (blue).

A second preliminary experiment was also concluded prior to the full investigation. This comprised of a tungsten current collector of which a 200 μm thin film of tungsten trioxide was grown onto the surface. The results of this experimentation may be observed in Figure 8.7. Rietveld refinement was conducted on the results and inspection of Figure 8.7 clearly shows a very good fit for the tungsten phase, as expected. The fit for the oxide phase has been omitted due to the fact that the fit from 2 reference patterns was not particularly good. This could be due to the fact that the thermally grown oxide film was a mixture of different oxidation states of tungsten and/or became contaminated during transportation to the neutron source. However, as the diffractogram clearly shows the addition of a second phase (with a good signal-to-noise ratio), the experimentation proved that this technique could be applied to a uranium|uranium oxide system.

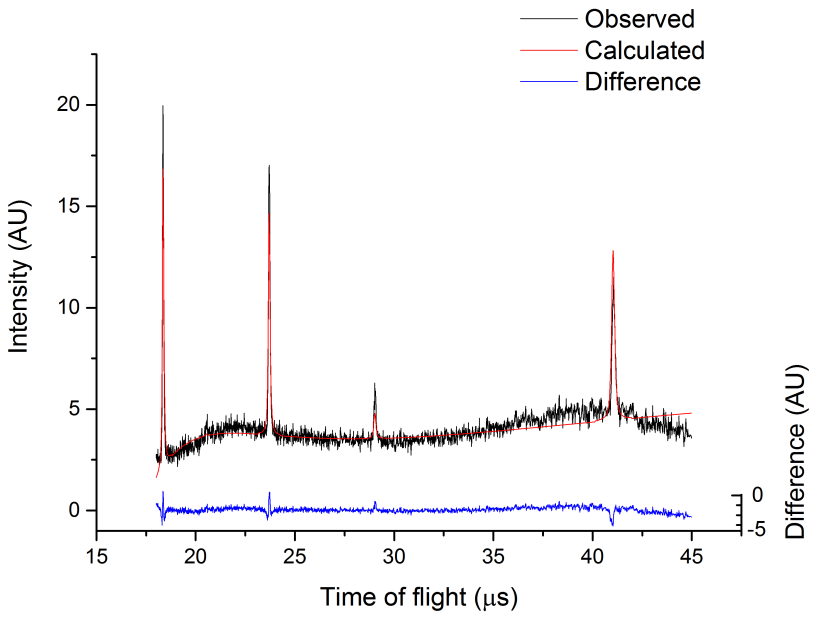

Fig. 8.8: Sample neutron diffractogram of a UO_2 filled MCE on the ENGIN-X beamline showing the observed data (black), the Rietveld refinement (red) and the difference plot (blue)

8.3.2 *In situ* Neutron diffraction of UO_2 MCEs

Following on from the preliminary studies conducted on the ENGIN-X beamline, the technique was deemed to be feasible to chemically characterise the electroreduction of UO_2 to U in LKE. For this experiment the *in situ* cell was used, as described in Section 4.2.6. Once the cell had become molten, UO_2 MCEs were inserted into the molten salt and connected to the potentiostat. During alignment, the working electrode was first coarsely aligned using the theodolite. Fine alignment was carried by systematically moving the stage in the X, Y and Z directions and measuring the intensity of the working electrode.

However, much difficulty arose from fine alignment; a signal for UO_2 was not observed during neutron irradiation. Figure 8.8 shows a dataset of an MCE *ex situ* that was irradiated for with thermal neutrons. The observable peaks in Figure 8.8 are all due to the molybdenum current collector of the MCE. Details of the peaks

Peak position	Miller index	D-spacing	Reference D-spacing [194]
18.335	3 1 0	0.997	0.995
23.679	2 1 1	1.286	1.285
29.004	2 0 0	1.575	1.573
41.011	1 1 0	2.228	2.225

Tab. 8.3: Showing calculated d-spacings of the molybdenum phase identified during neutron diffraction of a UO_2 filled MCE.

are tabulated in Table 8.3. From the collected data, no signal for UO_2 was observed. However, this is most likely attributed to experimental conditions rather than the technique itself. For example, it is likely that a larger sample is required to increase the signal to noise ratio for UO_2.

8.4 FIB Microstructural Characterisation

Following on from the advanced chemical characterisation presented in the previous subsection, this subsection focuses on the advanced microstructural characterisation of the electrode. The need to characterise the microstructure in three dimensions has previously been stated within this thesis (see Section 2.3.1) and so this section focuses, specifically, on the three dimensional characterisation. Although FIB tomography is a destructive tomography technique, it does permit high spatial resolution; voxel of sizes in the tens of nanometres are easily achieved.

The sample presented in this section is the same MBE that was exposed to the cyclic voltammogram presented in Figure 7.3. The resulting MBE from this voltammetry is presented in Figure 8.9(a) and (b). Figure 8.9(a) shows a "birds-eye view" of the MBE electrode and clearly shows two distinct regions; a dense phase towards the centre of the electrode and a more porous phase towards the outer edges. This can be more clearly seen in Figure 8.9(b). Because the MBE, in this case, was subjected to small reduction currents, the UO_2 is known to have only been partially reduced to U metal; a total of -0.22 mC were passed during the three reduction peaks, relating to a total mass of approximately 0.2 μg of UO_2

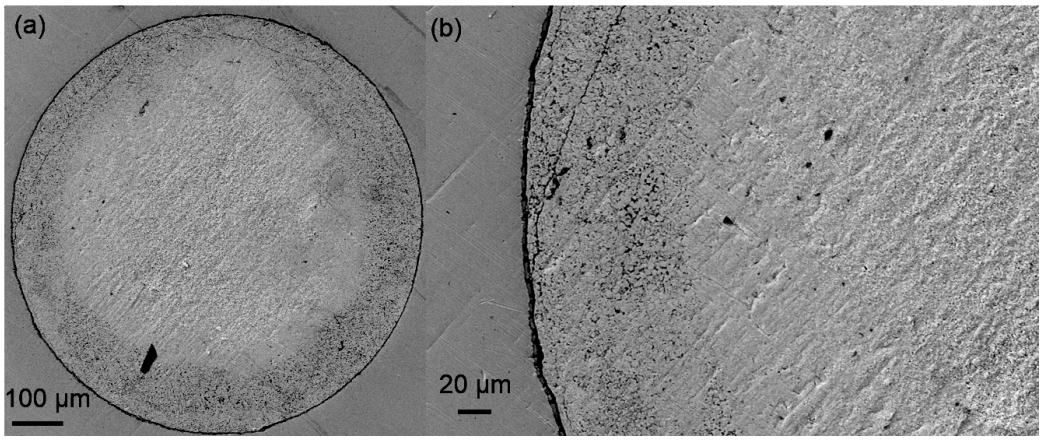

Fig. 8.9: (a) SEM micrograph of the MBE showing two phases. (b) shows these phases more clearly ans (c) is a reproduced micrograph of a partially reduced MOX pellet from Kurata *et al.*

being reduced. Because of the triple phase interline theory, the electrochemical reduction is predicted to propagate from the current collector to the centre of the MBE electrode and so a more porous phase is expected at the edge of a partially reduced MBE.

Energy dispersive X-ray spectroscopy (EDS) was performed on two regions of the MCE: around the outer edge of the MBE and towards the centre of the MBE, after the interface between the dense and coral-like phases. A schematic of the regions and resulting EDS data is shown in Figure 8.10. Although EDS is predominantly a surface quantification tool and is unable to provide information of the chemical composition below the surface of the MBE (EDS is limited to volumes of *ca.* 5-8 µm deep [195]), it is clear that there is a significant decrease in the observation of the O (Kα) peak on the spectra of the coral-like structure.

This, coupled with the known charged passed, provides more support to the partial reduction of the MBE electrode. It also supports the fact that the electroreduction appears to propagate from the edge of the electrode, towards the center, coinciding with the theory of TPIs. Therefore, microstructural characterisation was performed on the different regions of this MBE electrode in order to gain an insight

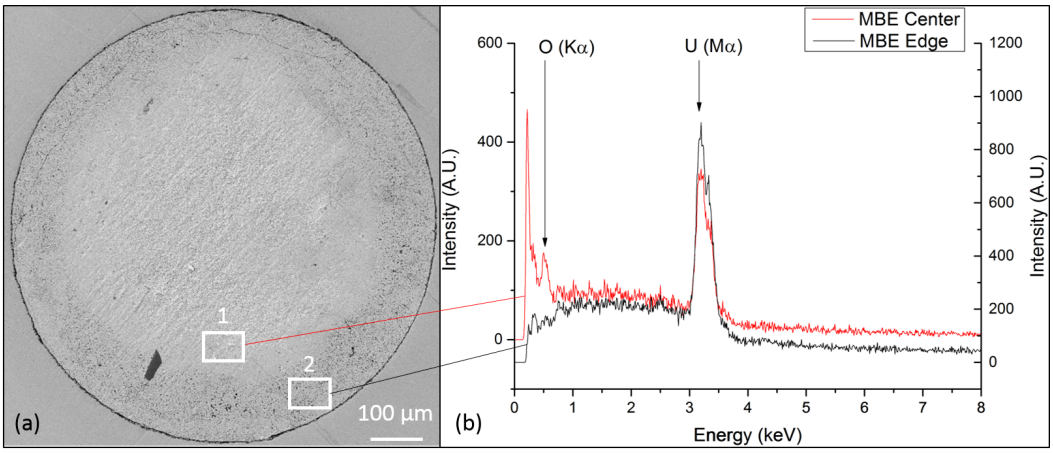

Fig. 8.10: Showing (a) the location of EDS collection and (b) the resulting EDS spectra taken at point 1 (red) and point 2 (black)

into the microstructure of both phases and to deduce any effects it may have on its performance during the electroreduction of UO_2 to U in LKE.

A 50 x 20 x 150 µm trench was cut using the FIB in order to allow for microstructural reconstruction from the edge of the sample to the centre. This resulted in 4 reconstructed regions to be produced with a voxel size of 90 nm^3. The first three regions were of the porous, coral-like structure, whilst the last reconstruction included the porous and dense phases. An SEM micrograph depicting the four reconstructed regions is displayed in Figure 8.11. As shown in Figure 8.11, approximately, the first one-third of the reconstruction is that of the porous, coral-like, structure. The remainder of the reconstruction is of the denser phase of the MBE.

8.4.1 Reconstructions

The image sequences produced during FIB slice and view were first aligned using the "StackReg" plug-in on the ImageJ software package, before being cropped using MATLAB and analysed using the Avizo Fire 8 software package. This resulted in a binary image of the solid phase and porous phase. Segmentation of these phases allowed for the full reconstruction of these phases and allowed for specific microstructural characterisation of these phases. Presented in the following subsections are the

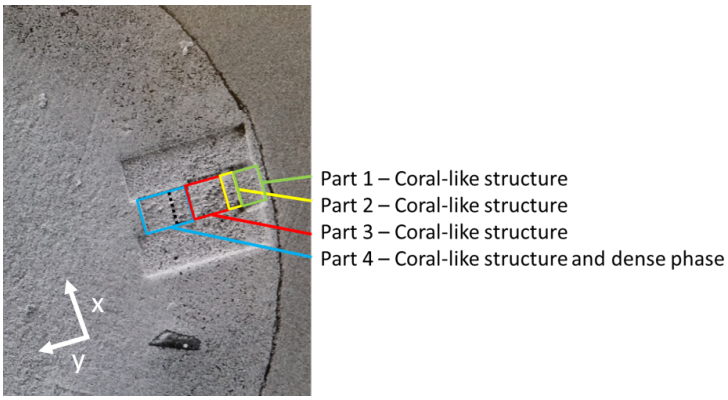

Fig. 8.11: SEM Micrograph depicting the four regions that were reconstructed using FIB tomography. The last section is a combination of the porous and dense phases. The x, y and z directions are also all defined here, where z is the direction into the page.

four sections as shown in Figure 8.11. A label analysis has been conducted on each sample. This label analysis deduces which pores are connected (based on a 24 voxel neighbourhood) and results in each connected pore being assigned a new colour, allowing for visual identification of the pore connectivity.

A reconstruction of part 1 is presented in Figure 8.12. Figure 8.12(a) shows the segmented porous phase of the sample and depicts a highly connected pore network, indicated by the bulk of the pores being a single colour. Figure 8.13(b) is presented in order for the reader to observe all three planes. Also presented in Figure 8.12(c) and (d) are skeletization projections of the pore phase. These projections visualise the centreline of interconnected pores as thinned filaments. That is, the centreline of the porous phase is displayed as a network of filaments which help to represent the centroid pathways of the pore network. A high density of these filaments is representative of a highly porous and well connected system, whereas a low density is indicative of a poorly connected network. The absence of these filaments represents the solid phase of the material.

Observation of Figure 8.12 shows that the microstructure contains a high pore connectivity, as indicated by large turquoise-coloured pore. The pore connectivity

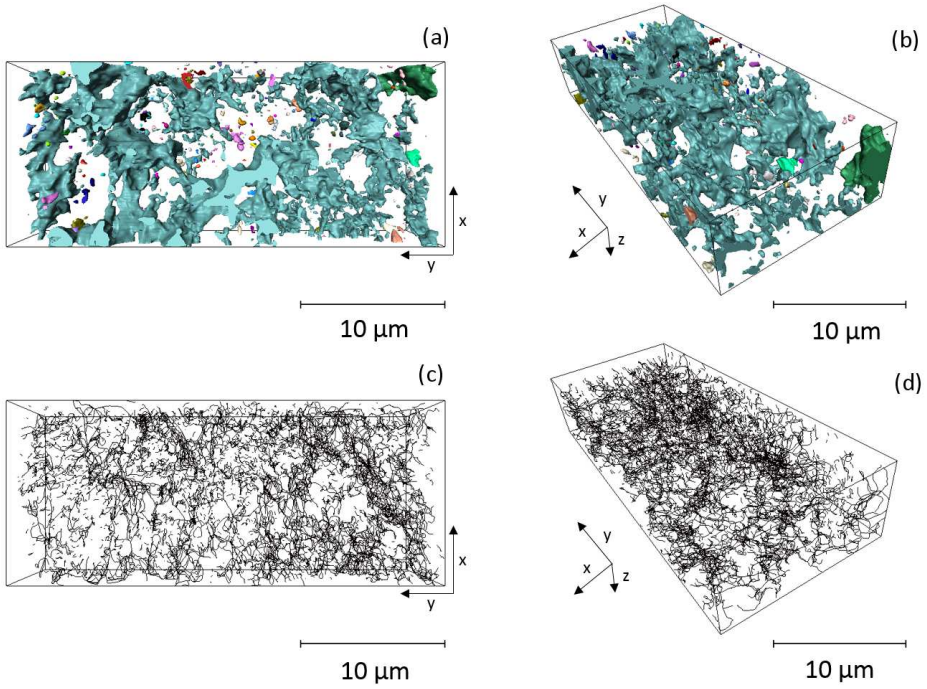

Fig. 8.12: Part 1 of the partially reduced MBE showing the the pore phase in (a) the XZ plane and (b) the XYZ plane. (c) shows a skeletization of the pore phase in the XZ plane and (d) in the XYZ plane.

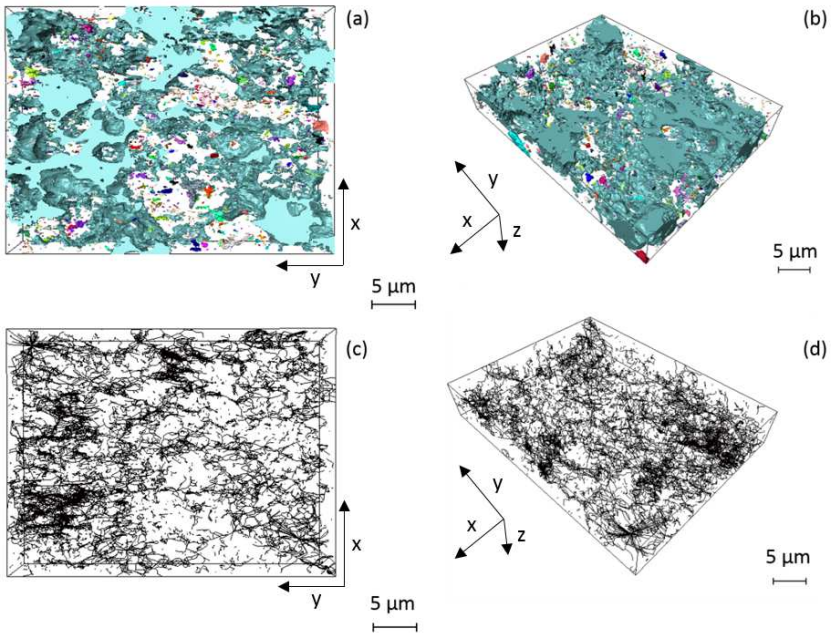

Fig. 8.13: Part 2 of the partially reduced MBE showing the the pore phase in (a) the XZ plane and (b) the XYZ plane. (c) shows a skeletization of the pore phase in the XZ plane and (d) in the XYZ plane.

was extracted and is equal to 88.32% which would permit good diffusion of species through the microstructure. This can also be seen by the high density of filaments in the skeletization show in Figure 8.12(c) and (d). The overall porosity was also extracted to be equal to 17.36%.

Figure 8.13 shows the sample reconstruction in part 2, with the skeletization projections also shown. By studying Figure 8.13, one is able to conclude, similarly to part 1, that the reconstructed volume for part two is also highly porous and is very well connected.

The porosity of this particular sample was extracted to be 17.62% with a total pore connectivity of 92.78%. This high pore connectivity would support the diffusion of O^{2-} ions away from the sample, indicating that the local build-up of the activity of oxygen anions would not be dramatically impeded by the microstructure. Figure 8.14 shows the sample reconstruction of part 3. Again, many similarities to the

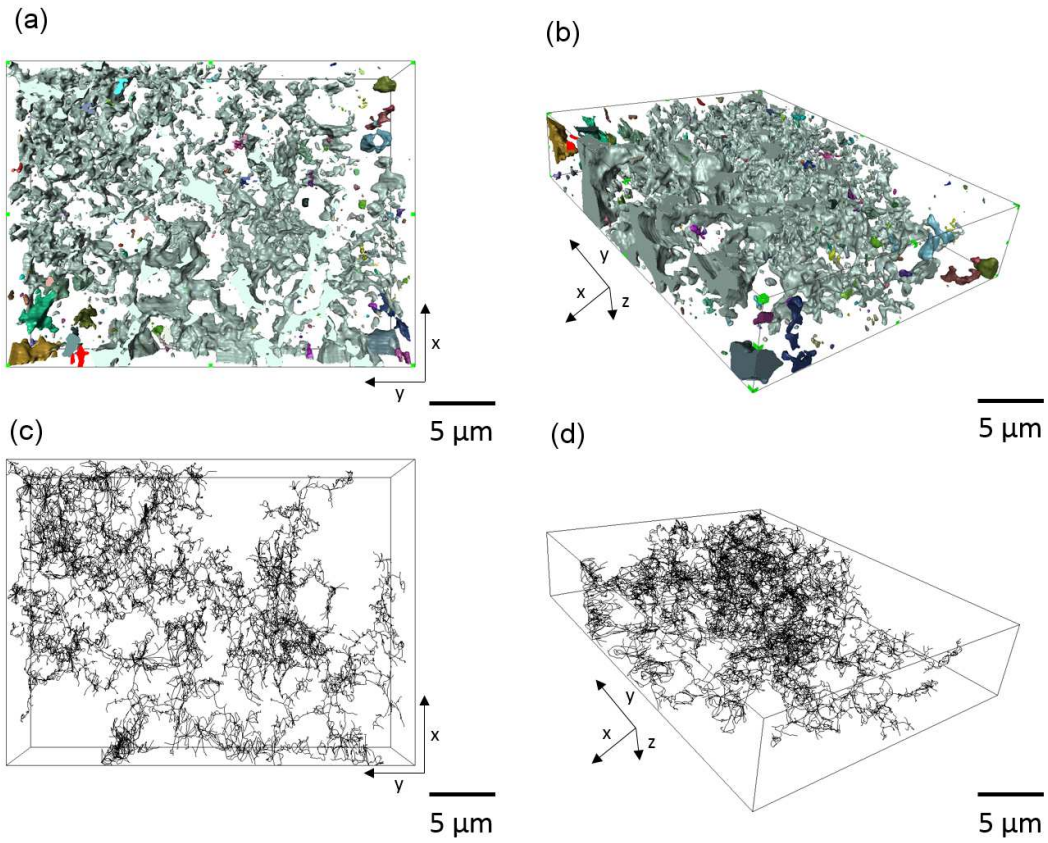

Fig. 8.14: Part 3 of the partially reduced MBE showing the the pore phase in (a) the XZ plane and (b) the XYZ plane. (c) shows a skeletization of the pore phase in the XZ plane and (d) in the XYZ plane.

previous two reconstructions may be drawn. However, the porosity of this region was extracted to be 12.27% which is significantly lower than the previous porosities extracted. In addition, the pore connectivity (87.96%) was also extracted to be lower than the previous two reconstructions.

Lastly, Figure 8.15 depicts similar reconstructions on part 4 of the MBE: XZ and XYZ planes of the pore phase and skeletization are displayed. Drastic microstructural changes compared to the previously presented reconstructions may be observed in Table 8.4. The overall porosity extracted is significantly less than that of the rest of the parts that were reconstructed. The porosity of part four - as a whole - was extracted to be 7.36% with a pore connectivity of 60.12%. This result is somewhat

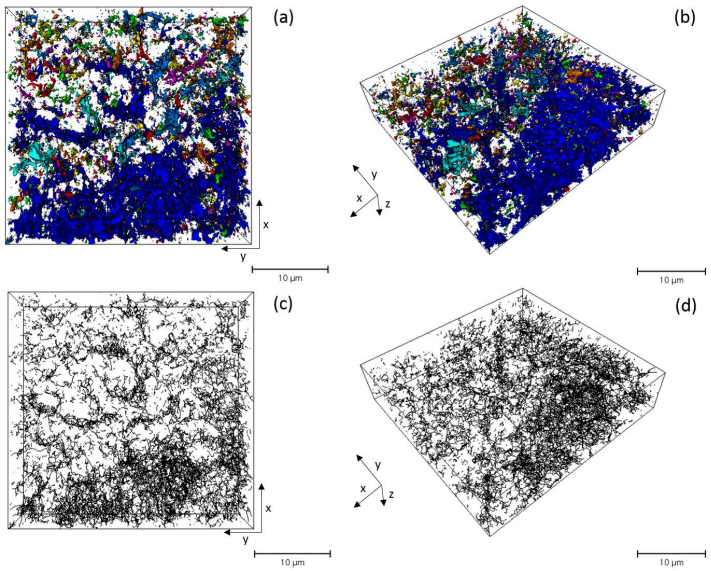

Fig. 8.15: Part 4 of the partially electroreduced MBE reconstructions showing the the pore phase in both (a) the XZ plane and (b) the XYZ plane. (c) shows a skeletization of the pore phase in the XZ plane and (d) a skeletization in the XYZ plane. The interface can be clearly shown as the porosity is significantly reduced.

expected as a dense phase was observed in Figure 8.9. However, the change in microstructure between the two phases strongly indicates that the diffusion of O^{2-} ions may be impeded at the interface: the point of the electroreduction reaction.

Figures 8.15(a) and (b) both show the drastic reduction in the connectivity of the pore phase. The porosity is reduced from 10.40 % between the coral-like structure and the interface to a value of 3.8% afterwards. The pore connectivity also drastically reduces from a value of 84.80% to a value of 17.86% after the interface. Although the porosity of the electrode will increase after O^{2-} ions have been liberated from the electrode due to the volume change associated with the electroreduction, the electrochemical reduction would be dependent on this volume change causing the isolated pores to become connected. However, if pores do not become connected due to the volume change, this would cause a local increase in the pO^{2-} and could potentially impede the electrochemical reduction.

Part #	Porosity (%)	Pore Connectivity (%)
1	17.36	88.32
2	17.62	92.78
3	12.27	87.96
4 (total)	7.36	60.12
4 (coral-like structure phase only)	10.40	84.80
4 (dense phase only)	3.91	17.86

Tab. 8.4: Showing the porosity and pore connectivity of all reconstructed parts of the MBE. Region 4 has also been split into its two corresponding regions.

This phenomena is also portrayed via the skeletization reconstructions in Figures 8.15(c) and (d). Regions corresponding to the highly porous and highly connected pore regions show a high filament density which is supportive of the diffusion of O^{2-} ions. However, when looking at the dense phase, the density of these skeletal filaments become significantly lower. The length of these filaments also appears to be smaller than that compared to the coral-like structure phase. This shows that the pores are smaller than those in the coral-like structure phase and, again, represents poor pore connectivity.

Table 8.4 shows some of the microstructural characteristics of each of the parts of the MBE. Parts one and two share very similar microstructural characteristics. However, part three shows a decrease in porosity and pore connectivity with part 4 showing an even more drastic decrease in porosity and pore connectivity as a whole. In addition, by splitting part four into the two sections relating to the porous phase and the dense phase, a general trend of decreasing porosity and pore connectivity may be observed from the outer edge towards the centre of the MBE. This trend is indicative of the electrochemical reduction propagating through the MBE electrode, from the edge to the centre. The porosity values in Table 8.4 portray a general trend of decreasing porosity from the outside of the electrode inwards. As this is the direction in which the electrochemical reduction is predicted to propagate in, the porosity change may be attributed to the volume change associated with the reduction of uranium dioxide. The decreased pore connectivity may have consequences

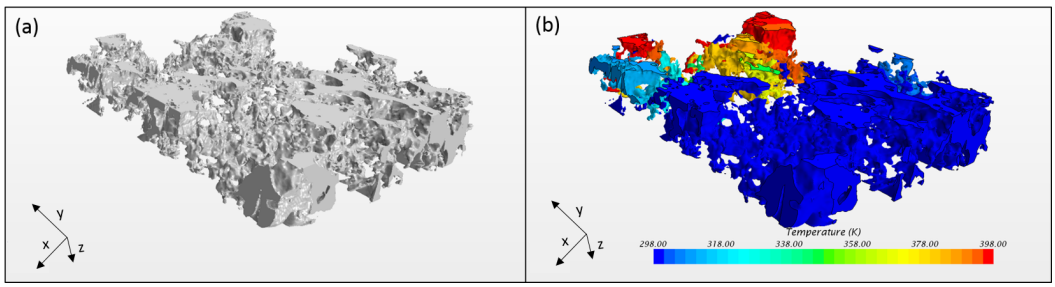

Fig. 8.16: Shows (a) the surface mesh reconstruction of the pore phase in StarCCM and (b) a representation of the Z-direction flux through the pore phase.

on the efficiency of the electroreduction process. This decrease in pore connectivity could impede the diffusion of O^{2-} out of the electrode and cause and increase in the level of pO^{2-}, which could cause the impediment of the electroreduction. This phenomena is expanded upon in the following subsection.

8.4.2 Tortuosity Simulations

Surface meshes were imported into the StarCCM+ software package in order to model the X,Y and Z direction heat fluxes, which is analogous to the mass flux through the pore phase. This was done to extract the tortuosities of each direction (see Section 3.2.3). After importing surfaces meshes, volume meshes were created and the flux was modelled through the pore phase and a solid control volume. For this, an arbitrary temperature of 100°C was chosen.

Figure 8.16(a) shows an example surface mesh reconstruction in the StarCCM+ software package (note that the triangle mesh interfaces are not shown) while Figure 8.16(b) shows a visual representation of the flux through the volume. Inspection of Figure 8.16(b) shows that the bulk of the microstructure is at a constant temperature of *ca.* 298 K. Towards the top left of the image there is a large change in the temperature which is indicative of an area of large flux. The reason is because, although there is a high pore connectivity, the pore pathway is concentrated in one small region, as shown in Figure 8.17.

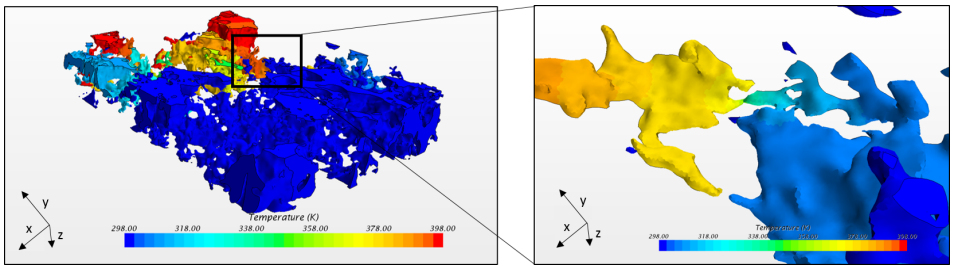

Fig. 8.17: Showing a zoomed in region of the Z-direction flux simulation. This shows that, although the pore phase is connected, there is only a small region of connectivity resulting in a high tortuosity.

Because the microstructure has only a small region of connectivity, this results in a poor flux throughout the bulk of the pore phase and, in turn, causes an increased tortuosity of the microstructure. Ultimately, what this would mean is that would be a higher probability of the microstructure of the electrode inhibiting the diffusion of O^{2-} ions out of the electrode and into the bulk salt to be consumed at the counter electrode.

These simulations were carried out for all parts of the MBE electrode that were reconstructed in Section 8.4 (for information of how the tortuousity in each axis is calculated, please refer to Section 3.2.3). The results of these simulations are displayed in Table 8.5. It should be noted that only the biggest pore of these reconstructions were extracted and modelled. This is because the unconnected pores would not have contributed to the flux and could have caused the heat flux to not converge. Also, on part four, only the pore phase before the interface to the dense phase was modelled. This is because of the very low pore connectivity would have resulted in an infinite tortuosity to be calculated.

From Table 8.5 it is clear that all of sample volumes that were reconstructed all possess a high tortuosity. Interestingly, this reveals that the bulk microstructure of the electrode is highly tortuous throughout. This, combined with the pore connectivity data presented in Table 8.4, shows that the pores phase throughout the bulk sample would provide a highly tortuous pathway for molten salt penetration.

Part #	τ_X	τ_Y	τ_Z
1	1.46	4.42	12.41
2	18.85	3.68	12.93
3	15.02	7.22	∞
4	∞	∞	∞

Tab. 8.5: Table showing the tortuosities of each reconstructed part in the X, Y and Z directions.

This could result in significant inhibition of the diffusion of O^{2-} ions away from the electrode. In turn, this could lead to the local level of the pO^{2-} to become less, resulting in a change in the potential for electrochemical reduction. In fact, this could explain the incomplete electroreduction of the UO_2 MBE presented in Section 7.2.1.

The TPI theory predicts that the electrochemical reduction would propagate radially from the current collector edge, to the centre of the MBE/MCE. This would be along the y-direction defined in Figure 8.11. Observation of the tortuosity in this direction, τ_Y, for all reconstructed volumes it is seen to first reduce from a value of 4.42 in part one to a value of 3.68 in part two. This follows the trend of increased porosity and pore connectivity between the two regions. However, the value increases significantly from 3.68 in region two to a value of 7.22 in region three. This, again following the decrease in porosity and pore connectivity, reveals a much more tortuous route for the diffusion of O^{2-} ions.

In addition, the tortuosity of the entire part four reconstruction, and τ_Z of part three, are infinite. This phenomenon occurs in regions where the pore connectivity is low. Because of this, the pore phase is not well connected causing the flux calculations to be unable to converge. This, coupled with the low porosity towards the centre of the electrode, is indicative of the fact that the microstructure within this region would impede the penetration of molten salt and, ultimately, the diffusion of O^{2-} ions. The pore connectivity seems to be a function of the volume change associated with the electrochemical reduction. This is a dynamic variable which would

change as the electroreduction propagates throughout the bulk electrode. Because of this, it is suggested that the diffusion of O^{2-} ions away from the electrode would be dependent on the probability of the volume change during electroreduction causing the isolated pores to become connected. This would inherently be a function of the initial microstructure that would require full characterisation and possibly optimising during industrial processing.

8.5 X-ray Computed Tomography

Following on from the FIB tomography microstructural characterisation presented in Section 8.4, this subsection uses the non-destructive nature of the X-ray computed tomography technique to investigate MCE electrodes. MCE electrodes, rather than MBE electrodes, were chosen for this reconstruction due to the fact that they offer less attenuation to X-rays. Two MCE electrodes were investigated using X-ray CT: The first was a freshly prepared UO_2 filled MCE (5 holes) and the second was a fully reduced MCE (3 holes remained after electroreduction). This investigation forms a proof-of-concept for four dimensional studies.

In order to fulfil health and safety criteria during scanning, the electrodes were required to be fully encapsulated in epoxy. An image of one of the sample in the X-ray CT machine may be seen in Figure 8.18. An X-ray generation voltage of 120 kV was used to acquire all radiographs. Reconstructions provided a voxel size of 3.37 μm^3 which is noted to be much larger than the 90 nm^3 acquired from the FIB tomography reconstructions presented in Section 8.4. As a result, the data sets presented here are unable to capture the some of the small porosity associated with these electrodes. However, it is able to provide a field of view greater than the sample, allowing for potential *in situ* microstructural characterisation.

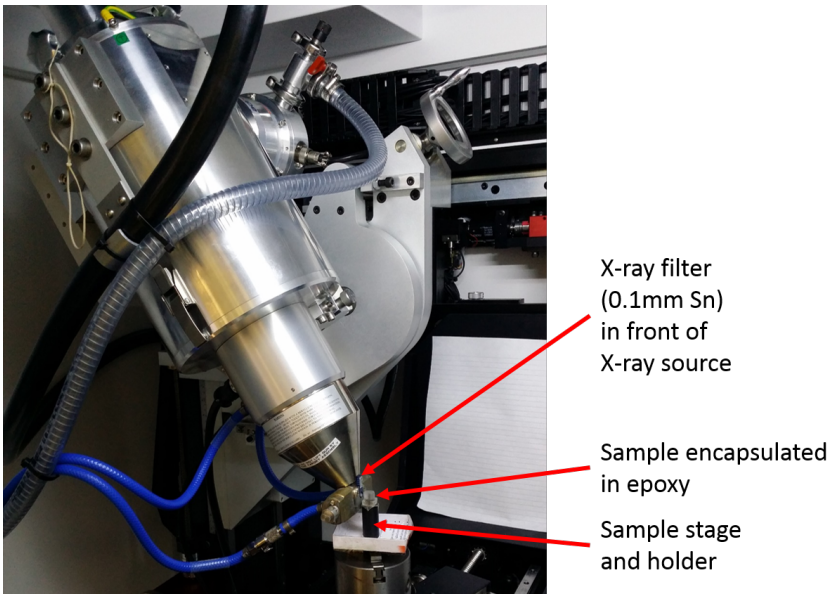

Fig. 8.18: A photograph of one of the sample inside the Nikon XTH225 ST X-ray CT scanner

8.5.1 X-ray Reconstruction of the Microstructure

For each scan a total of *ca.* 3200 projections were acquired for each MCE which resulted in a total of, approximately, 1500 orthoslices of the MCE to be reconstructed, per scan. A sample radiograph of the surface of a UO_2 filled MCE and a resulting orthoslice inside of the middle hole is presented in Figure 8.19.

From the orthoslice depicted in Figure 8.19, it is possible to see the metal current collector phase, large void space (porosity) and solid powder particles. Segmentation for all MCE holes was performed in the Avizo Fire 8 software suite allowing for three dimensional reconstruction of each phase.

Presented in Figure 8.20 are reconstructions of the solid phase (UO_2) inside the MCE. Labels (a) - (e) correspond with holes 1-5, as defined in Figure 8.19. The reconstructions all show that the MCEs are all relatively well packed, apart from hole number three (Figure 8.20(c)). A large void is present in hole three which is likely due to the initial packing of the electrode. This void is also visible in the radiograph in Figure 8.19. It should also be noted that the holes are not completely

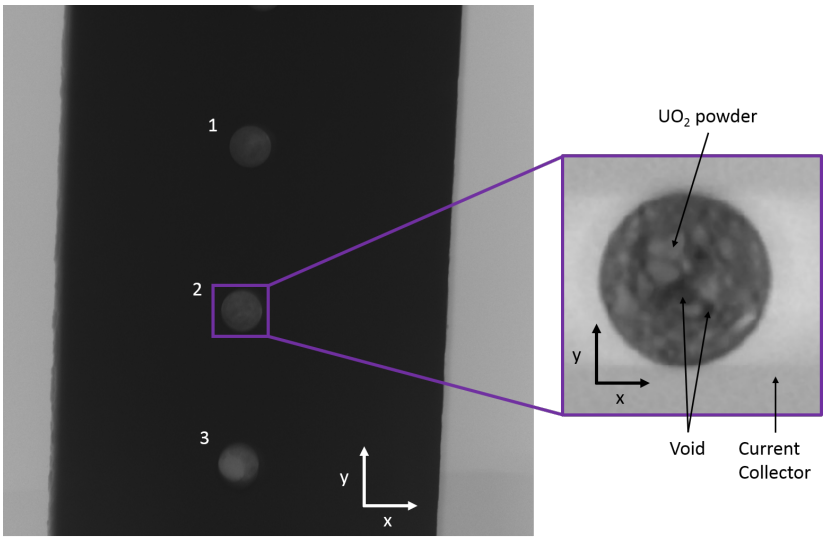

Fig. 8.19: showing a sample radiograph of a UO_2 filled MCE acquired on the Nikon XTH225 ST and a resulting orthoslice of a hole in the same plane. The numbers 1-3 are used to identify the holes in the MCE. Holes 4 and 5 are not shown in this radiograph.

filled as the solid powder typically only occupies between 27-55% of the total volume of the MCE hole. This porosity is quantified in Table 8.6. The void fraction, or porosity, is significantly higher compared to the values calculated using the FIB tomography technique. The reason for this is likely due to powder being ejected from the MCE during epoxy impregnation.

It should be noted that because the solid phase has been reconstructed (as opposed to the porous phase in the FIB tomography) the pellets appear to be completely dense, although they are in fact very porous. The solid phase was reconstructed in this study due to the low volume fraction of the solid.

The feature of low solid volume fraction was found to be much more significant in the reduced samples which may be observed in Figure 8.21. From this, it is clear that the powder has been mostly ejected from the MCE. This is expected more in the reduced samples because of a number of reasons: the first is that due to the large volume change associated with the electroreduction, the structural integrity of the electrode may be compromised after electroreduction. Moreover, after the electrodes

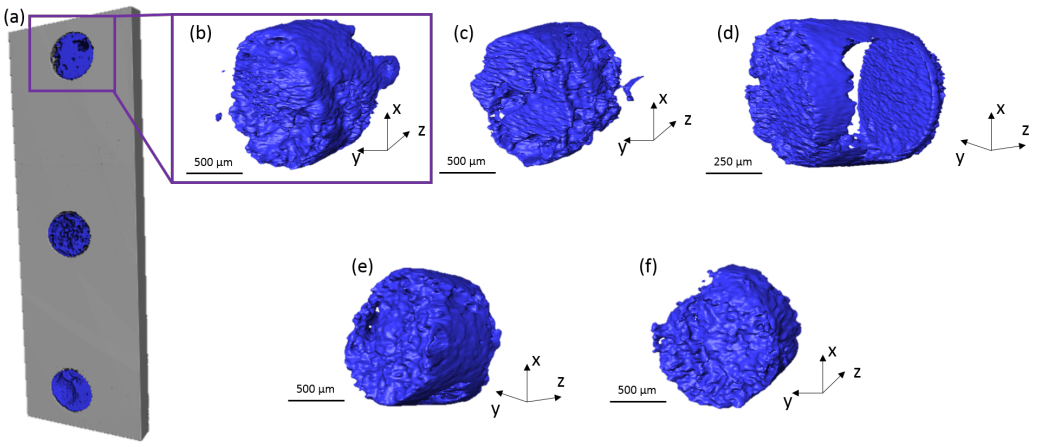

Fig. 8.20: Microstructural reconstruction of the UO_2 filled MCE showing (a) the first three holes of the MCE and (b)-(f) shows the five reconstructed holes (labelled as hole 1-5 respectively).

UO_2 filled MCE hole number	Calculated solid volume fraction (%)
1	32.22
2	54.94
3	27.83
4	41.27
5	47.13

Tab. 8.6: Tabulated values of the solid volume fraction of the UO_2 powder within each hole of the MCE

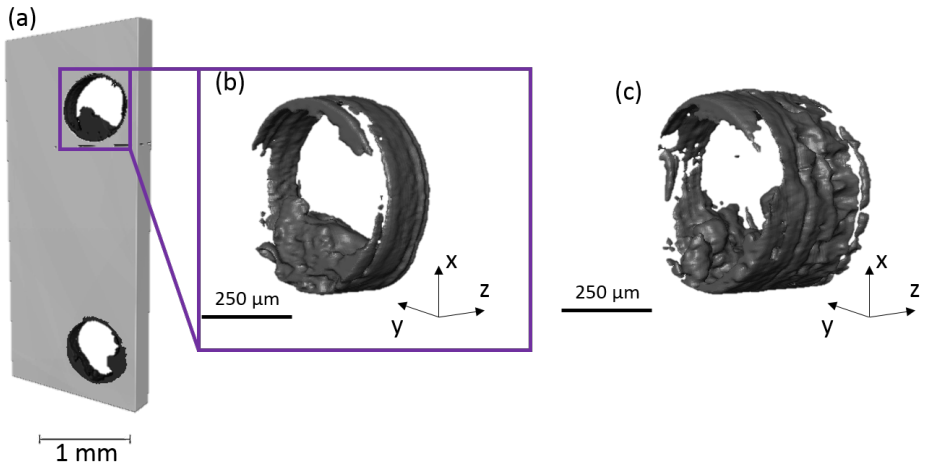

Fig. 8.21: Showing the microstructural reconstructions of the electrochemically reduced MCE showing (a) hole one and (b) hole two. Hole three was completely empty after epoxy impregnation.

have been immersed in the molten salt, a thin layer of salt becomes frozen over the electrodes. In order to remove this salt (which is highly hygroscopic) the electrode is immersed in methanol for 72 hours to remove the residual salt. This process could further compromise the structural integrity of the electrode. After these two processes have occurred, the electrode is then impregnated in epoxy which would penetrate the pellet more than the UO_2 electrodes, due to the higher void space created during electroreduction. The flow of epoxy into this larger void space could further increase the probability of the powder to be ejected from the electrode. This theory is supported by the fact that solid powder is observed around the edge of the MCE - a region which would be affected less.

Two particles are observable towards to bottom of Figure 8.21(b). These particles inherently show the suitability of this tomography technique to study the microstructure of these electrodes. It is believed that improvements in the electrode structure would permit full microstructural characterisation of this system as well as higher resolution X-ray CT. This would also permit a step-wise scanning of the same sample during the electrochemical reduction process.

In conclusion, X-ray CT has been utilized as a technique to study the microstructure of a UO_2 MCE and an MCE which had been electrochemically reduced to U. The investigations provided an insight into the overall structure of the MCEs and demonstrated proof of concept that this technique may be used to study this system. The structural integrity of the MCE electrodes seem to be compromised during epoxy impregnation as pore volume fractions as high as 72.17% have been calculated for the UO_2 electrodes. It is anticipated that a more rigorous electrode structure (such as MBEs) would help to negate this effect and with some optimisation could lead to the acquisition of high quality data that would compliment the FIB tomography data presented in Section 8.4.

8.6 Conclusion

This section has investigated material characterisation of the electrochemical reduction process using advanced characterisation techniques. Firstly, the use of synchrotron radiation has been utilized to follow the electrochemical reduction pathway *in situ*. The results show that the electrochemical reduction does, indeed, occur via a single, 4-electron transfer, process as electrochemically characterised in Chapter VII.

Additionally, the microstructure of both MBE and MCE electrodes have been studied. A partially reduced MBE was studied using FIB tomography resulting in four volume reconstructions. The porosity along the axis of the propagation of the electrochemical reduction was seen to reduce drastically from 17.62% in the coral-like structure phase to a value of 3.91% in the dense phase. Moreover, the tortuosity in this plane was also seen to increase from a value of 4.42 to an infinite tortuosity in the dense phase. This microstructural phenomena would impede the diffusion of O^{2-} ions from the bulk electrode which would decrease the local value of pO^{2-}. Referring to the Littlewood diagram presented in Figure 5.2, this could result in the potential for electroreduction to be more negative than the cathodic decomposition

potential of the LKE electrolyte. If this were to occur then this would cause the electrochemical reduction in LKE to not be possible.

Chapter IX. Conclusions and Future Work

9 Conclusions and Future work

9.1 Conclusions

The work of this thesis has combined thermodynamic predictions with electrochemical and material characterisation techniques in order to demonstrate the feasibility of electrochemically reducing uranium dioxide to uranium in lithium chloride-potassium chloride eutectic and to elucidate the electrochemical reduction mechanism.

The following subsections draw the main conclusions associated with the thermodynamic predictions (Chapter V), the electrochemical characterisation (Chapter VII) and material characterisation (Chapter VIII).

9.1.1 Thermodynamic predictions

The Littlewood diagrams constructed and presented in Chapter V allowed for a visual representation of the thermodynamically predicted K-Li-U-O-Cl molten salt system. Although these Littlewood diagrams are inherently limited by the thermodynamic data used to construct them, they are a very useful tool to allow for a rapid prediction of molten salt systems. The diagrams presented in LKE assume that the Gibbs free energy of the formation of O^{2-} ion is a weighted average of its dissociation from Li_2O and K_2O. This is due to the O^{2-} ions being a minority in the melt with it's nearest neighbour shells being Li^+, K^+ and Cl^-. This assumption is validated due to the melt having a quasi-crystalline structure.

Perhaps the most significant conclusion to be drawn from the Littlewood diagrams presented for uranium species in LKE is the predicted dependence upon the pO^{2-} of the molten salt. The diagrams predict that the electroreduction may only occur above a pO^{2-} value of approximately 6, at 773 K. Higher activities of O^{2-}

(lower values of pO^{2-}) would see the potential for electroreduction of UO_2 to be more negative than the decomposition potential of the molten salt.

The flexibility of these diagrams was also presented by superimposition of the diagrams for both plutonium and uranium species in LKE at 773 K onto one another. This provides a thermodynamic prediction of the system which could be applied to, for example, the selective electroreduction of uranium dioxide in a MOX fuel.

The thermodynamic representation of this system was used as a basis for the experimentation and provided an insight into the dependence of the electroreduction on the pO^{2-}. In fact, this dependence has been shown to be valid with the experimentation presented in Section 7.3.

9.1.2 Electrochemical Characterisation

During the electrochemical characterisation presented in Chapter VII, MBE and MCE electrodes were electrochemically reduced using sweep voltammetry and chronoamperometry. Using cyclic voltammetry, a single electrochemical reduction peak was observed compared to unfilled MBE/MCE electrodes. This electrochemical reduction peak was seen to be close the cathodic decomposition potential of the molten salt. The Littlewood diagram for uranium species (Figure 5.2) predicts the level of pO^{2-} to be *ca.* 6.5 at this point.

Multiple scan cyclic voltammetry was also performed, resulting in the decrease in the electrochemical reduction peak current for UO_2 to U (peak C2) after each sweep. In addition, there was no observable re-oxidation peak associated with peak C2. This is highly supportive of the theory that the liberated O^{2-} ions are diffusing away from the working electrode (and likely being consumed at the counter electrode). This results in the O^{2-} ions not being available for re-oxidation. This reduction of the peak current at C2, therefore, may be attributed to less material being available for electrochemical reduction.

Chronoamperometry studies also showed the ability to electrochemically reduce

UO_2 to U via a constant potential electrolysis technique. During chronoamperometry, the current was seen to initially increase before steadily reducing to a value close to zero. SEM micrographs of the resulting electrodes showed the microstructure to be highly porous with a coral-like structure, similar to that observed by Kurata *et al.* [64]. The total current passed during the chronoamperometry performed in Figure 7.5 was calculated to be 420% more than the theoretical value required. Although the current efficiency of this electroreduction was not possible to be performed (due to difficulties in ensuring the powder remained inside the electrode during cleaning) this is indicative of a low current efficiency being associated with the electroreduction.

In addition, the effect of the bulk value of pO^{2-} was investigated on the electrochemical reduction peak C2. Firstly, a pO^{2-} indicator electrode was built and calibrated. This electrode allowed the direct measurement of the pO^{2-} value to be deduced without having to remove a sample of the salt and potentially compromising the cell's environment. Figure 7.9 showed that the electrochemical reduction peak C2 was observable at a pO^{2-} value of 6.2, as expected. However, this reduction peak was then unobservable after the pO^{2-} value was decreased to a value close to zero. This result provides significant support to the thermodynamic predictions of the molten salt system and also confirms the susceptibility of this electroreduction to the activity of O^{2-} ions.

9.1.3 Material Characterisation

Chapter VIII focused on the development and application of advanced material characterisation techniques to study the effects of the electrochemical reduction on the electrodes. Firstly, synchrotron radiation was utilized to follow the electrochemical reduction pathway of the electroreduction *in situ*. Throughout the *in situ* EDXD experimentation, all phases of the system were identified and characterised. The direct observation of the reduction in peak intensity of UO_2 and the simultaneous increase

in peak intensity for U provides strong evidence that the electrochemical reduction does, indeed, occur via a single, 4-electron transfer, process. The the exclusion of any other phases in the EDXD data also supports this. The electrochemical reduction potential of the UO_2|U appeared to be dependent on the activity of oxide ion existing within the melt. This was indicated by the inhibition of the electrochemical reduction during electrolysis. Theoretically, if the pO^{2-} of the molten salt remained constant, the electroreduction of UO_2 should have been observed to continue. The neutron diffraction technique was also utilized and was demonstrated to be a useful technique for following electrochemical processes *in situ*.

Secondly, the microstructural evolution was also studied using a combination of unreduced UO_2 electrodes, partially reduced electrodes and fully reduced electrodes. FIB tomography on the partially reduced electrode resulted in four sample volume reconstructions of which one included both coral-like and dense microstructures. The coral-like structure is attributed to the volume change associated with the electrochemical reduction of UO_2 to U. By studying the sub-volumes along the y-plane (the plane in which the electrochemical reduction is believed to propagate along) the microstructure was seen to drastically evolve. The total porosity of the and the pore connectivities of the sample volumes were all seen to drastically reduce, especially in the dense region. Moreover, the tortuosity of these sub-volumes were all seen to drastically increase. A combination of the decrease in porosity, pore connectivity and increases in the pore phase tortuosities all suggest that the microstructure of the electrodes may impede the diffusion of O^{2-} ions from the electrode. This may, in turn, cause an increase in the local activity of O^{2-} ions and cause the inability to electrochemically reduce UO_2 to U. Therefore, the microstructure of the initial UO_2 electrode is an extremely important factor in the overall efficiency of the electrochemical reduction process. A highly porous microstructure which promotes a high pore connectivity and low tortuosity would be beneficial in ensuring that the electrochemical reduction in not impeded by a build up of oxygen anions within the

electrode.

9.2 Future Work

The following subsections briefly describe possible future topics in which this work may be expanded into.

9.2.1 Selective Electroreduction of Mixed Oxide Fuel

Although the work of this thesis elucidates the electrochemical reduction of uranium dioxide to uranium in the lithium chloride-potassium chloride eutectic, one may wish to consider expanding this study into UO_2 electrodes that contain 1-2% of PuO_2. The motivation behind this work is due to the fact that, in reality, spent fuel pellets contain 1-2% of PuO_2. The selective electrochemical reduction of uranium dioxide would be the head end process before the electrorefiner in the pyroprocessing process, as opposed to the oxide reduction unit [190, 196, 197]. The Littlewood diagrams presented in Chapter V predict the selective electrochemical reduction of UO_2 to be close to that of the reduction potential of Pu_2O_3 (a predicted intermediate between PuO_2 and Pu). Therefore, experimentation would be required to deduce the feasibility of this selective electrochemical reduction.

9.2.2 X-ray Computed Tomography Studies

The work presented in Section 8.5 provided an insight into the bulk microstructural characterisation of MBE/MCE electrodes. However, due to health and safety regulations, the electrodes were required to be impregnated in epoxy which, in turn, lead to artificial changes to the electrode microstructure. The work presented in Section 8.5 provides a proof-of-concept of the advantages of using X-ray CT to study these electrodes in their entirety. It is suggested that the electrode structure is optimised in order for these experiments to be carried out. One suggestion is the use of MBE which have a much smaller outer diameter compared to the ones presented in this thesis (Section 4.3.2). For example, 0.8 mm holes may be drilled into the cross

section of 1 mm diameter rods (as opposed to 3 mm rods used in this thesis) would significantly decrease the attenuation of the X-rays. This would also permit the microstructure to be characterised both before and after electrochemical reduction. There is also scope to use higher resolution X-ray CT.

9.2.3 *In Situ* Microstructural Characterisation

In Chapter VIII, microstructural characterisation showed that the inherent microstructure of the electrode may directly impede the diffusion of O^{2-} ions which could result in the impediment of the electroreduction. However, the microstructure of these electrodes were studied *ex situ*. *In situ* microstructural analysis would offer a unique insight into the microstructural changes occurring within the molten salt environment.

9.2.4 Electrochemical Reduction Studies on Spent LWR Pellets

The microstructure of nuclear light water reactor (LWR) pellets is currently well understood. Studying actual spent fuel pellets has obvious advantages and would offer a true ability to optimise the electrochemical reduction procedure and would highlight any changes in the structure of the electrodes required to increase the efficiency of the electrochemical reduction process.

9.2.5 Pulsed Chronoamperometry for Uranium Electrodeposition

The electrodeposition of uranium metal is the overall end product of the pyroprocessing process [190]. However, many studies highlight the dendritic deposition of uranium metal via electrodeposition (see Section 2.2.3.1). Process costs could be eliminated if the electrorefining unit were able to prepare metallic fuel pellets during electrodeposition. In order to prepare uniform and homogeneous deposition of uranium metal, a pulsed chronoamperometry technique could be implemented. Vargas and Inman were able to control the nucleation and growth of chromium deposits

by employing a pulsed chronoamperometry technique in the LiCl-KCl eutectic [60]. The authors were able to produce adherent and coherent films of chromium by utilizing this technique. It is suggested that this would prove advantageous to the electrodeposition of uranium metal in LKE.

Dissemination

Peer Reviewed Publications

The following are first-authored peer reviewed publications in which disseminate the work of this thesis.

- Brown, L. D., Abdulaziz, R., Simons, S., Inman, D., Brett, D. J. L., & Shearing, P. R. (2013). *Predominance diagrams of uranium and plutonum species in both lithium chloride–potassium chloride eutectic and calcium chloride.* Journal of Applied Electrochemistry, 43(12), 1235-1241.

- Brown, L.D., Abdulaziz, R., Simons, S., Inman, D., Brett, D., Shearing, P.R. (2013) *Electrochemical Reduction Of Uranium (IV) Oxide And Its Analogues In Molten Lithium Chloride-Potassium Chloride Eutectic.* (Proceedings) 2nd International Symposium on Sustainable Molten Salt and Ionic Liquid Processing, Shectman Symposium.

- Brown, L. D., Abdulaziz, R., Jervis, R., Bharath, V., Attwood, R., Reinhard, C., Connor, L.D., Simons, S.J.R., Inman, D., Brett, D.J.L. & Shearing, P. R. (2015). *Following the electroreduction of uranium dioxide to uranium in LiCl-KCl eutectic in situ using synchrotron radiation.* Journal of Nuclear Materials. *In Press.*

Co-Authored Peer Reviewed Publications

The following are works in have been co-authored. It is noted that these publications abide by the scope of this thesis.

- Abdulaziz, R., Brown, L. D., Inman, D., Simons, S., Shearing, P. R., & Brett, D. J. (2014). *Novel fluidised cathode approach for the electrochemical reduction*

of tungsten oxide in molten LiCl–KCl eutectic. Electrochemistry Communications, 41, 44-46.

- Abdulaziz, R., Brown, L. D., Inman, D., Simons, S. J., Shearing, P. R., & Brett, D. J. (2014). *Effects of Process Conditions on the Fluidised Cathode Electrochemical Reduction of Tungsten Oxide in Molten LiCl-KCl Eutectic.* ECS Transactions, 64(4), 323-331.

- Abdulaziz, R., Brown, L. D., Inman, D., Simons, S. J., Shearing, P. R., & Brett, D. J. (2014). *A Fluidised Cathode Process for the Electrochemical Reduction of Tungsten Oxide in A Molten LiCl-KCl Eutectic.* ECS Transactions, 58(19), 65-74.

- Robinson, J. B., Brown, L. D., Jervis, R., Taiwo, O. O., Millichamp, J., Mason, T. J., Neville, T. P., Eastwood, D. S., Reinhard, C., Lee, P. D., Brett, D. J. L., & Shearing, P. R. (2014). *A novel high-temperature furnace for combined in situ synchrotron X-ray diffraction and infrared thermal imaging to investigate the effects of thermal gradients upon the structure of ceramic materials.* Synchrotron Radiation, 21(5).

- Robinson, J. B., Brown, L. D., Jervis, R., Taiwo, O. O., Heenan, T. M. M., Millichamp, J., Mason, T. J., Neville, T. P., Clague, R., Eastwood, D. S., Reinhard, C., Lee, P. D., Brett, D. J. L., & Shearing, P. R. (2015). *Investigating the effect of thermal gradients on stress in solid oxide fuel cell anodes using combined synchrotron radiation and thermal imaging.* Journal of Power Sources. *In press.*

Conference Presentations (Oral)

The following is a list of oral presentations given to disseminate the work of this thesis.

- *Uranium electroplating in molten lithium chloride-potassium chloride eutectic*, The Molten Salts Discussion Group, Christmas Meeting, 2013.

- *Electrochemical Reduction Of Uranium (IV) Oxide And Its Analogues In Molten Lithium Chloride-Potassium Chloride Eutectic*; 2nd International Symposium on Sustainable Molten Salt and Ionic Liquid Processing, Shectman Symposium, 2014

Conference Presentations (Poster)

The following is a list of poster presentations given to disseminate the work of this thesis.

- *Following The Electrochemical Reduction Of UO_2 To U In Lithium Chloride-Potassium Chloride Eutectic In-Situ Using White Beam EDXD,* Diamond SR User Meeting, Diamond Light Source, 2014

- *Following The Electrochemical Reduction Of UO_2 To U In Lithium Chloride-Potassium Chloride Eutectic In-Situ Using White Beam EDXD*, Molten Salt Discussion Group, Christmas Meeting, 2014

- *Understanding the Thermal Behaviour of SOFC by Crystallographic Strain Mapping*, Diamond SR User Meeting, Diamond Light Source, 2012

Appendices

Appendix A - Uranium Species Littlewood Diagram Equations

The following are equations used to construct the uranium species Littlewood diagrams in Chapter V.

$$UO_2 + 4e^- \leftrightarrow U + 2O^{2-} \tag{9.1}$$

$$\varepsilon_{9.1} = \frac{-\Delta G_{9.1}}{nF} + \frac{\eta RT ln10}{nF} \cdot pO^{2-}$$

$$U + 3Cl^- \leftrightarrow UCl_3 + 3e^- \tag{9.2}$$

$$\varepsilon_{9.2} = \frac{-\Delta G_{9.2}}{nF}$$

$$UO_2 + 3Cl^- + e^- \leftrightarrow UCl_3 + 2O^{2-} \tag{9.3}$$

$$\varepsilon_{9.3} = \frac{-\Delta G_{9.3}}{nF} + \frac{\eta RT ln10}{nF} \cdot pO^{2-}$$

$$UCl_3 + 2O^{2-} \leftrightarrow UO_2Cl_2 + Cl^- + 3e^- \tag{9.4}$$

$$\varepsilon_{9.4} = \frac{-\Delta G_{9.4}}{nF} + \frac{\eta RT ln10}{nF} \cdot pO^{2-}$$

$$3UO_2 + 2O^{2-} \leftrightarrow U_3O_8 + 4e^- \tag{9.5}$$

$$\varepsilon_{9.5} = \frac{-\Delta G_{9.5}}{nF} + \frac{\eta RTln10}{nF} \cdot pO^{2-}$$

$$3UO_2Cl_2 + 2O^{2-} \leftrightarrow U_3O_8 + 6Cl^- \tag{9.6}$$

$$\varepsilon_{9.6} = \frac{-\Delta G_{9.6}}{nF} + \frac{\eta RTln10}{nF} \cdot pO^{2-}$$

$$UO_2Cl_2 + 2Cl^- + 2e^- \leftrightarrow UCl_4 + 2O^{2-} \tag{9.7}$$

$$\varepsilon_{9.7} = \frac{-\Delta G_{9.7}}{nF} + \frac{\eta RTln10}{nF} \cdot pO^{2-}$$

$$UCl_3 + Cl^- \leftrightarrow UCl_4 + e^- \tag{9.8}$$

$$\varepsilon_{9.8} = \frac{-\Delta G_{9.8}}{nF}$$

$$Li_2UO_4 + 2e^- \leftrightarrow UO_2 + 2O^{2-} + 2Li^+ \tag{9.9}$$

$$\varepsilon_{9.9} = \frac{-\Delta G_{9.9}}{nF} + \frac{\eta RTln10}{nF} \cdot pO^{2-}$$

$$3Li_2UO_4 + 2e^- \leftrightarrow U_3O_8 + 4O^{2-} + 6Li^+ \tag{9.10}$$

$$\varepsilon_{9.10} = \frac{-\Delta G_{9.10}}{nF} + \frac{\eta RTln10}{nF} \cdot pO^{2-}$$

$$Li_2UO_4 \leftrightarrow UO_3 + O^{2-} + 2Li^+ \tag{9.11}$$

$$pO^{2-} = \frac{\Delta G_{9.11}}{RTln10}$$

Appendix B - Plutonium Species Littlewood Diagram Equations

The following are equations used to construct the uranium species Littlewood diagrams in Chapter V.

$$2PuO_2 + 2e^- \leftrightarrow Pu_2O_3 + O^{2-} \tag{9.12}$$

$$\varepsilon_{9.12} = \frac{-\Delta G_{9.12}}{nF} + \frac{\eta RTln10}{nF} \cdot pO^{2-}$$

$$2PuO_2 + 2e^- + Cl^- \leftrightarrow PuOCl + O^{2-} \tag{9.13}$$

$$\varepsilon_{9.13} = \frac{-\Delta G_{9.13}}{nF} + \frac{\eta RTln10}{nF} \cdot pO^{2-}$$

$$PuO_2 + e^- + 3Cl^- \leftrightarrow PuCl_3 + 2O^{2-} \tag{9.14}$$

$$\varepsilon_{9.14} = \frac{-\Delta G_{9.14}}{nF} + \frac{\eta RTln10}{nF} \cdot pO^{2-}$$

$$Pu_2O_3 + 2Cl^- \leftrightarrow 2PuOCl + O^{2-} \tag{9.15}$$

$$pO^{2-} = \frac{\Delta G_{9.15}}{RTln10}$$

$$PuCl_3 + O^{2-} \leftrightarrow PuOCl + 2Cl^- \tag{9.16}$$

$$pO^{2-} = \frac{\Delta G_{9.16}}{RTln10}$$

$$PuCl_3 + 3e^- \leftrightarrow Pu + 3Cl^- \tag{9.17}$$

$$\varepsilon_{9.17=\frac{-\Delta G_{9.17}}{nF}}$$

$$Pu_2O_3 + 6e^- \leftrightarrow 2Pu + 3O^{2-} \tag{9.18}$$

$$\varepsilon_{9.18=\frac{-\Delta G_{9.18}}{nF}+\frac{\eta RTln10}{nF}\cdot pO^{2-}}$$

$$PuOCl + 3e^- \leftrightarrow Pu + O^{2-} + Cl^- \tag{9.19}$$

$$\varepsilon_{9.19=\frac{-\Delta G_{9.19}}{nF}+\frac{\eta RTln10}{nF}\cdot pO^{2-}}$$

Bibliography

References

[1] Department of Energy and Climate Change . The carbon plan: Delivering our low carbon future, 2011.

[2] A. M. Stoneham. Nuclear fission: the interplay of science and technology. *Philosophical Transactions of the Royal Society A: Mathematical, Physical and Engineering Sciences*, 368(1923):3295–3313, 2010.

[3] J. G. Marques. Evolution of nuclear fission reactors: Third generation and beyond. *Energy Conversion and Management*, 51(9):1774–1780, 2010.

[4] M. Lenzen. Life cycle energy and greenhouse gas emissions of nuclear energy: A review. *Energy Conversion and Management*, 49(8):2178–2199, 2008.

[5] P.D Wilson. *The Nuclear Fuel Cycle: From Ore To Waste*. Oxford Science Publications, 1996.

[6] D. D. Sood and S. K. Patil. Chemistry of nuclear fuel reprocessing: Current status. *Journal of radioanalytical and nuclear chemistry*, 203(2):547–573, 1996.

[7] J. Fisher. Energy density of coal. *The Physics Factbook*, 2003.

[8] W.H. Hannum, D. Wade, and G. Stanford. Self-protection in dry recycle technologies. *International Conference on Evaluation of Engineering Nuclear Fuel Cycle Systems, Global '95, Versailles, France*, 1995.

[9] W. Loveland, D. Morrissey, and G. Seaborg. *Modern nuclear chemistry*. John Wiley & Sons, 2005.

[10] R. Benedict, C. Solbrig, B. Westphal, T. Johnson, S. Li, K. Marsden, and K. Goff. Pyroprocessing progress at Idaho National Laboratory. pages 741–747. American Nuclear Society, 2007.

[11] T. Inoue, T. Koyama, M. Myochin, and Y. Arai. Pyroprocessing technology development in Japan. In *GLOBAL 2007: Advanced Nuclear Fuel Cycles and Systems, September 9, 2007 - September 13, 2007*, GLOBAL 2007: Advanced Nuclear Fuel Cycles and Systems, pages 728–737, Boise, ID, United states, 2007. American Nuclear Society.

[12] T. Inoue, T. Koyama, and Y. Arai. State of the art of pyroprocessing technology in Japan. In *2nd International Conference on Asian Nuclear Prospects, ANUP 2010, October 10, 2010 - October 13, 2010*, volume 7 of *Energy Procedia*, pages 405–413, Mamallapuram, India, 2011. Elsevier Ltd.

[13] S. Lee, K. Thomas, J. Marlow, H. Menlove, W. Ko, M. Yang, and S. Park. A preliminary study on the safeguardability of a Korean advanced pyroprocessing facility (KAPF). Technical report, American Nuclear Society, 555 North Kensington Avenue, La Grange Park, IL 60526 (United States), 2007.

[14] F. Gao, W. Ko, C. Park, and H. Lee. Criticality safety evaluation of materials concerning pyroprocessing. *Journal of Nuclear Science and Technology*, 48(6): 919–928, 2011.

[15] J.L. Bates, C.A. Hinman, and T. Kawada. Electrical conductivity of uranium dioxide. *Journal of the American Ceramic Society*, 50(12):652 – 656, 1967.

[16] N.J. Dudney, R.L. Coble, and H.L. Tuller. Electrical conductivity of pure and yttria-doped uranium dioxide. *Journal of the American Ceramic Society*, 64 (11):627 – 631, 1981.

[17] G. Z. Chen, D.J. Fray, and T. W. Farthing. Direct electrochemical reduction of titanium dioxide to titanium in molten calcium chloride. *Nature*, 407(6802): 361–364, 2000.

[18] F. S. Wartman, Don H. Baker, J. R. Nettle, and V. E. Homme. Some ob-

servations on the Kroll process for titanium. *Journal of The Electrochemical Society*, 101(10):507–513, 1954.

[19] K. Dring, R. Dashwood, and D. Inman. Voltammetry of titanium dioxide in molten calcium chloride at 900°C. *Journal of The Electrochemical Society*, 152 (3):E104–E113, 2005.

[20] C. Schwandt and D. J. Fray. Determination of the kinetic pathway in the electrochemical reduction of titanium dioxide in molten calcium chloride. *Electrochimica Acta*, 51(1):66–76, 2005.

[21] R. Bhagat, D. Dye, S. Raghunathan, R. Talling, D. Inman, B. Jackson, K. Rao, and R. Dashwood. In situ synchrotron diffraction of the electrochemical reduction pathway of TiO_2. *Acta Materialia*, 58(15):5057–5062, 2010.

[22] D.T.L. Alexander, C. Schwandt, and D.J. Fray. Microstructural kinetics of phase transformations during electrochemical reduction of titanium dioxide in molten calcium chloride. *Acta Materialia*, 54(11):2933–2944, 2006.

[23] J. S. Wilkes. A short history of ionic liquids–from molten salts to neoteric solvents. *Green Chemistry*, 4(2):73–80, 2002.

[24] M. Hirao, K. Ito, and H. Ohno. Preparation and polymerization of new organic molten salts; N-alkylimidazolium salt derivatives. *Electrochimica Acta*, 45(8–9):1291 – 1294, 2000.

[25] B. Tremillon. Reactions in molten salts. In *Reactions In Solution An Applied Analytical Approach*. Wiley, 1997.

[26] Y. Castrillejo, A.M. MartÃnez, G.M. Haarberg, B. Borresen, K.S. Osen, and R. Tunold. Oxoacidity reactions in equimolar molten $CaCl_2$-NaCl mixture at 575° C. *Electrochimica Acta*, 42(10):1489 – 1494, 1997.

[27] R. Combest, M.N. Levelut, and B. Tremillon. Oxo-acidity and its influence on the electrochemical properties in molten mixtures of $CeCl_3$ and equimolar NaCl–KCl at 1000 k. *Electrochimica Acta*, 23(12):1291 – 1295, 1978.

[28] R. Littlewood. Diagrammatic representation of the thermodynamics of metal fused chloride systems. *Journal of The Electrochemical Society*, 109(6):525, 1962.

[29] R. Molina. Propriétés chimiques de quelques éléments dans l'eutectique chlorure de lithium-chlorure de potassium fondu. *Bull. Soc. Chim. Fr*, 6: 1184–1190, 1961.

[30] M.D. Adams, D.A. Wenz, and R.K. Steunenberg. Observation of a uranium (v) species in molten chloride salt solutions[1a]. *The Journal of Physical Chemistry*, 67(9):1939–1941, 1963.

[31] J. Katz and E. Rabinowitch. *The Chemistry of Uranium. Part I: The element, its binary and related compounds.* McGraw-Hill Book Co., 1951.

[32] V. Komorov and N. Nekrasova. *Elektrokhimiya*, 17:448, 1981.

[33] G. Landresse and G. Duyckaerts. Diagramme potential pO^{2-} de l'uranium dans l'eutectique LiCl-KCl fondu. *Analytica Chimica Acta*, 65(1):245–247, 1973.

[34] T. Ishno. *J. Electrochem. Soc. Jap.*, 34:133, 1966.

[35] I. Uchida, J. Niikura, and S. Toshima. Electrochemical study of UO_2^{2+}-UO_2^{+}-UO_2 system in molten LiCl-KCl eutectic. *Journal of Electroanalytical Chemistry and Interfacial Electrochemistry*, 124(1-2):165–177, 1981.

[36] I. Uchida, J. Niikura, and S. Toshima. Pulse polarography of uranyl (VI) in molten LiCl-KCl eutectic. *Journal of Inorganic and Nuclear Chemistry*, 43 (3):549–552, 1981.

[37] D. Hill, J. Perano, and R. Osteryoung. An electrochemical study of uranium in fused chlorides. *J. Electrochem. Soc.*, 107:698, 1960.

[38] O. Knacke, J. Krahe, and R. Weber. *Z. Physik. Chem. N. F.*, 67:194, 1969.

[39] L. Martinot and J. Fuger. Determination of solubility products of various actinide oxides in the (Na-K)Cl and (Li-K)Cl eutectics and calculation of new Potential-pO^{2-} diagrams. *Journal of the Less-Common Metals*, 120(2):255–266, 1986.

[40] L. Martinot and G. Duyckaerts. Diagrammes potentiel/pO^{2-} du neptunium et du plutonium dans l'eutectique LiCl-KCl. *Analytica Chimica Acta*, 66(3): 474–476, 1973.

[41] G. Landresse and G. Duyckaerts. Étude par spectrophotométrie d'absorption des propriétés chimiques du plutonium dans l'eutectique LiCl-KCl fondu. *Analytica Chimica Acta*, 73(1):121–127, 1974.

[42] C. Caravaca, A. Laplace, J. Vermeulen, and J. Lacquement. Determination of the E–pO^{2-} stability diagram of plutonium in the molten LiCl–KCl eutectic at 450° C. *Journal of Nuclear Materials*, 377(2):340–347, 2008.

[43] S. P. Ong. Thermal stabilities of delithiated olivine MPO_4 (M= Fe, Mn) cathodes investigated using first principles calculations. *Electrochemistry communications*, 12(3):427, 2010.

[44] F. Kobayashi, T. Ogawa, M. Akabori, and Y. Kato. Anodic dissolution of uranium mononitride in lithium chloride-potassium chloride eutectic melt. *Journal of the American Ceramic Society*, 78(8):2279–2281, 1995.

[45] S.X. Li and M.F. Simpson. Anodic process of electrorefining spent nuclear fuel in molten LiCl–KCl–UCl_3/Cd system. In *Proceedings of the 201st meeting of*

the Electrochemical Society, 13th International Symposium on Molten Salts, Philadelphia, 2002.

[46] D. Inman, G. J. Hills, L. Young, and J. O'M Bockris. Electrode reactions in molten salts: the uranium + uranium trichloride system. *Transactions of the Faraday Society*, 55:1904–1914, 1959.

[47] L. R. Morss, N. M. Edelstein, J. Fuger, and J. J. Katz. *The Chemistry of the Actinide and Transactinide Elements (Volumes 1-5): Vol. 1.* Springer, 2007.

[48] Y. Sakamura, O. Shirai, T. Iwai, and Y. Suzuki. Distribution behavior of plutonium and americium in LiCl–KCl eutectic/liquid cadmium systems. *Journal of alloys and compounds*, 321(1):76–83, 2001.

[49] O. Shirai, T. Iwai, K. Shiozawa, Y. Suzuki, Y. Sakamura, and T. Inoue. Electrolysis of plutonium nitride in LiCl-KCl eutectic melts. *Journal of nuclear materials*, 277(2):226–230, 2000.

[50] T. Ogawa and K. Minato. Dissolution and formation of nuclear materials in molten media. *Pure and Applied Chemistry*, 73(5):799 – 806, 2001.

[51] S. A. Kuznetsov, H. Hayashi, K. Minato, and M. Gaune-Escard. Electrochemical behavior and some thermodynamic properties of UCl_4 and UCl_3 dissolved in a LiCl-KCl eutectic melt. *Journal of The Electrochemical Society*, 152(4): C203 – C212, 2005.

[52] Y. Sakamura, T. Hijikata, K. Kinoshita, T. Inoue, T.S. Storvick, C.L. Krueger, J.J. Roy, D.L. Grimmett, S.P. Fusselman, and R.L. Gay. Measurement of standard potentials of actinides (U, Np, Pu, Am) in LiCl-KCl eutectic salt and separation of actinides from rare earths by electrorefining. *Journal of Alloys and Compounds*, 271:592–596, 1998.

[53] B. Prabhakara Reddy, S. Vandarkuzhali, T. Subramanian, and P. Venkatesh. Electrochemical studies on the redox mechanism of uranium chloride in molten LiCl-KCl eutectic. *Electrochimica Acta*, 49(15):2471–2478, 2004.

[54] F. H. Driggs. Preparation of metal powders by electrolysis of fused salts 1 – ductile uranium. *Industrial and engineering chemistry*, 22(5):516, 1930.

[55] P. Masset, D. Bottomley, R. Konings, R. Malmbeck, A. Rodrigues, J. Serp, and J. P. Glatz. Electrochemistry of uranium in molten LiCl-KCl eutectic. *Journal of The Electrochemical Society*, 152(6):A1109–A1115, 2005.

[56] T.i Koyama, M. Iizuka, Y. Shoji, R. Fujita, H. Tanaka, T. Kobayashi, and M. Tokiwai. An experimental study of molten salt electrorefining of uranium using solid iron cathode and liquid cadmium cathode for development of pyrometallurgical reprocessing. *Journal of nuclear science and technology*, 34(4): 384–393, 1997.

[57] A. Osipenko, A. Mayershin, V. Smolenski, A. Novoselova, and M. Kormilitsyn. Electrochemistry of curium in molten chlorides. *Recent Trends in Electrochemical Science and Technology, InTech*, 2012.

[58] J. Serp, R. Konings, R. Malmbeck, J. Rebizant, C. Scheppler, and J. Glatz. Electrochemical behaviour of plutonium ion in LiCl-KCl eutectic melts. *Journal of Electroanalytical Chemistry*, 561:143–148, 2004.

[59] J. J. Roy, L. F. Grantham, D. L. Grimmett, S. P. Fusselman, C. L. Krueger, T. S. Storvick, T. Inoue, Y. Sakamura, and N. Takahashi. Thermodynamic properties of U, Np, Pu, and Am in molten LiCl-KCl eutectic and liquid cadmium. 143(8):2487–2492, 1996.

[60] T. Vargas and D. Inman. Controlled nucleation and growth in chromium

electroplating from molten LiCl-KCl. *Journal of Applied Electrochemistry*, 17 (2):270–282, 1987.

[61] J. Hur, C. Seo, S. Hong, D. Kang, and S. Park. Metallization of U_3O_8 via catalytic electrochemical reduction with Li_2O in LiCl molten salt. *Reaction kinetics and catalysis letters*, 80(2):217–222, 2003.

[62] C.S. Seo, S.B. Park, B.H. Park, K.J. Jung, S.W. Park, and S.H. Kim. Electrochemical study on the reduction mechanism of uranium oxide in a LiCl-Li_2O molten salt. *Journal of nuclear science and technology*, 43(5):587–595, 2006.

[63] S. Jeong, H. Shin, S. Hong, J. Hur, J. Do, and H. Lee. Electrochemical reduction behavior of U_3O_8 powder in a LiCl molten salt. *Electrochimica Acta*, 55(5):1749–1755, 2010.

[64] M. Kurata, T. Inoue, J. Serp, M. Ougier, and J. Glatz. Electro-chemical reduction of MOX in LiCl. *Journal of nuclear materials*, 328(2):97–102, 2004.

[65] J. Hauck. Uranates(VI) and tungstates(VI) within the system Li_2O-UO_3-WO_3. *Journal of Inorganic and Nuclear Chemistry*, 36(10):2291 – 2298, 1974.

[66] Y. Sakamura, M. Kurata, and T. Inoue. Electrochemical reduction of UO_2 in molten $CaCl_2$ or LiCl. *Journal of the Electrochemical Society*, 153(3):D31–D39, 2006.

[67] Masatoshi Iizuka, Tadashi Inoue, Michel Ougier, and Jean-Paul Glatz. Electrochemical reduction of (U, Pu) O_2 in molten LiCl and $CaCl_2$ electrolytes. *Journal of nuclear science and technology*, 44(5):801 – 813, 2007.

[68] R. D. Pierce. Progress in the pyrochemical processing of spent nuclear fuels. *JOM*, 45(2):40, 1993.

[69] J. Laidler. Pyrochemical recovery of actinides. *Proceedings of the American Power Conference*, 55(2):1074–1078, 1993.

[70] J. J. Laidler, J. E. Battles, W. E. Miller, J. P. Ackerman, and E. L. Carls. Development of pyroprocessing technology. *Progress in Nuclear Energy*, 31 (1-2):131–140, 1997.

[71] B. Park, J. Hur, C. Seo, and S. Park. A study on the electrochemical reduction of uranium oxide in a LiCl-Li_2O molten salt. 2003.

[72] C. J. Brabec, M. Heeney, I. McCulloch, and J. Nelson. Influence of blend microstructure on bulk heterojunction organic photovoltaic performance. *Chem. Soc. Rev.*, 40:1185–1199, 2011.

[73] MJ Jørgensen, S Primdahl, C Bagger, and M Mogensen. Effect of sintering temperature on microstructure and performance of LSM-YSZ composite cathodes. *Solid State Ionics*, 139(1):1–11, 2001.

[74] M. Uchida, Y. Fukuoka, Y. Sugawara, N. Eda, and A. Ohta. Effects of microstructure of carbon support in the catalyst layer on the performance of polymer electrolyte fuel cells. *Journal of The Electrochemical Society*, 143(7): 2245–2252, 1996.

[75] E. A. Holm. Three-dimensional materials science. *Scripta materialia*, 54(6): 1035, 2006.

[76] M. D. Uchic, L. Holzer, B. J. Inkson, E. L. Principe, and P. Munroe. Three-dimensional microstructural characterization using focused ion beam tomography. *MRS bulletin*, 32(05):408–416, 2007.

[77] H. W. Chan, J. G. Duh, and S. R. Sheen. Microstructure and electrochemical properties of LBO-coated Li-excess $Li_{1+x}Mn_2O_4$ cathode material at elevated temperature for Li-ion battery. *Electrochimica Acta*, 51(18):3645–3651, 2006.

[78] P. R. Shearing, L. E. Howard, P. S. Jorgensen, N. P. Brandon, and S. J. Harris. Characterization of the 3-dimensional microstructure of a graphite

negative electrode from a Li-ion battery. *Electrochemistry Communications*, 12(3):374–377, 2010.

[79] J. R. Wilson. Three-dimensional reconstruction of a solid-oxide fuel-cell anode. *Nature Materials*, 5(7):541, 2006.

[80] J. R. Wilson, A. T. Duong, M. Gameiro, H. Chen, K. Thornton, D.L. R. Mumm, and S. A. Barnett. Quantitative three-dimensional microstructure of a solid oxide fuel cell cathode. *Electrochemistry Communications*, 11(5): 1052–1056, 2009.

[81] J. R. Wilson, J. S. Cronin, S. A. Barnett, and S. J. Harris. Measurement of three-dimensional microstructure in a $LiCoO_2$ positive electrode. *Journal of Power Sources*, 196(7):3443–3447, 2011.

[82] Y. Deng. Electrochemistry at conductor/insulator/electrolyte three-phase interlines: a thin layer model. *The journal of physical chemistry. B*, 109(29): 14043, 2005.

[83] W. Xiao, X. Jin, Y. Deng, D. Wang, X. Hu, and G.Z. Chen. Electrochemically driven three-phase interlines into insulator compounds: Electroreduction of solid SiO_2 in molten $CaCl_2$. *ChemPhysChem*, 7(8):1750–1758, 2006.

[84] W. Xiao, X. Jin, Y. Deng, D. Wang, and G. Z. Chen. Three-phase interlines electrochemically driven into insulator compounds: A penetration model and its verification by electroreduction of solid AgCl. *Chemistry-A European Journal*, 13(2):604–612, 2007.

[85] F. Zhao, Y. Jiang, G. Y. Lin, and A. V. Virkar. *Solid Oxide Fuel Cell VII (ed. Singhal, S. C.)*. 2001.

[86] D. Natarajan. A two-dimensional, two-phase, multicomponent, transient model for the cathode of a proton exchange membrane fuel cell using con-

ventional gas distributors. *Journal of The Electrochemical Society*, 148(12): A1324, 2001.

[87] L. You. A two-phase flow and transport model for the cathode of PEM fuel cells. *International journal of heat and mass transfer*, 45(11):2277, 2002.

[88] P. R. Shearing, J. Golbert, R. J. Chater, and N. P. Brandon. 3D reconstruction of SOFC anodes using a focused ion beam lift-out technique. *Chemical Engineering Science*, 64(17):3928–3933, 2009.

[89] P. R. Shearing, Q. Cai, J. I. Golbert, V. Yufit, C. S. Adjiman, and N. P. Brandon. Microstructural analysis of a solid oxide fuel cell anode using focused ion beam techniques coupled with electrochemical simulation. *Journal of Power Sources*, 195(15):4804–4810, 2010.

[90] R. Clague, P. R. Shearing, P. D. Lee, Z. Zhang, D. J. L. Brett, A. J. Marquis, and N. P. Brandon. Stress analysis of solid oxide fuel cell anode microstructure reconstructed from focused ion beam tomography. *Journal of Power Sources*, 196(21):9018–9021, 2011.

[91] P. R. Shearing, J. Gelb, and N. P. Brandon. X-ray nano computerised tomography of SOFC electrodes using a focused ion beam sample-preparation technique. *Journal of the European Ceramic Society*, 30(8):1809–1814, 2010.

[92] P. R. Shearing, J. Gelb, J. Yi, W. K. Lee, M. Drakopolous, and N. P. Brandon. Analysis of triple phase contact in Ni-YSZ microstructures using non-destructive x-ray tomography with synchrotron radiation. *Electrochemistry Communications*, 12(8):1021–1024, 2010.

[93] P. R. Shearing, R. S. Bradley, J. Gelb, F. Tariq, P. J. Withers, and N. P. Brandon. Exploring microstructural changes associated with oxidation in Ni-

YSZ SOFC electrodes using high resolution x-ray computed tomography. *Solid State Ionics*, 216(0):69–72, 2012.

[94] F. Tariq, P.D. Lee, R. Haswell, and D.W. McComb. The influence of nanoscale microstructural variations on the pellet scale flow properties of hierarchical porous catalytic structures using multiscale 3D imaging. *Chemical Engineering Science*, 66(23):5804–5812, 2011.

[95] R. Singh, P.D. Lee, T.C. Lindley, C. Kohlhauser, C. Hellmich, M. Bram, T. Imwinkelried, and R.J. Dashwood. Characterization of the deformation behavior of intermediate porosity interconnected Ti foams using micro-computed tomography and direct finite element modeling. *Acta Biomaterialia*, 6(6):2342 – 2351, 2010.

[96] T.J. Marrow, J.-Y. Buffiere, P.J. Withers, G. Johnson, and D. Engelberg. High resolution x-ray tomography of short fatigue crack nucleation in austempered ductile cast iron. *International Journal of Fatigue*, 26(7):717 – 725, 2004.

[97] Paulo A.Z. Suarez, Vania M. Selbach, Jeane E.L. Dullius, Sandra Einloft, Clarisse M.S. Piatnicki, Denise S. Azambuja, Roberto F. de Souza, and Jairton Dupont. Enlarged electrochemical window in dialkyl-imidazolium cation based room-temperature air and water-stable molten salts. *Electrochimica Acta*, 42 (16):2533 – 2535, 1997.

[98] D. Inman, G. J. Hills, L. Young, and J.O'M. Bockris. Some thermodynamic aspects of molten salts: Halides of uranium, zirconium, thorium, and cerium in alkali halide eutectics*. *Annals of the New York Academy of Sciences*, 79 (11):803–829, 1960.

[99] R Parsons. *Modern Aspects of Electrochemistry*, 1:103, 1954.

[100] A. Lasia. Electrochemical impedance spectroscopy and its applications. *Modern Aspects of Electrochemistry*, 32:143–248, 1999.

[101] J. A. Edminister. *Theory and Problems of Electric Circuits*. McGRAW-HILL, 1972.

[102] B. P. Reddy, S. Vandarkuzhali, T. Subramanian, and P. Venkatesh. Electrochemical studies on the redox mechanism of uranium chloride in molten LiCl-KCl eutectic. *Electrochimica Acta*, 49(15):2471 – 2478, 2004.

[103] T. Nishina, S. Ohuchi, K. Yamada, and I. Uchida. Water effect on oxygen reduction in molten (Li + K)CO_3 eutectic. *Journal of Electroanalytical Chemistry*, 408(1-2):181 – 187, 1996.

[104] G. Kim, D. Yoon, S. Paek, S. Kim, T. Kim, and D. Ahn. A study on the electrochemical deposition behavior of uranium ion in a LiCl–KCl molten salt on solid and liquid electrode. *Journal of Electroanalytical Chemistry*, 682:128 – 135, 2012.

[105] S. Koch, M. Mogensen, P. V. Hendriksen, N. Dekker, and B. Rietveld. Electrode activation and passivation of solid oxide fuel cell electrodes. *Fuel Cells*, 6(2):117–122, 2006.

[106] M. Sahibzada, B. C. H. Steele, D. Barth, R. A. Rudkin, and I. S. Metcalfe. Operation of solid oxide fuel cells at reduced temperatures. *Fuel*, 78(6):639–643, 1999.

[107] M. J. Jorgensen and M. Mogensen. Impedance of solid oxide fuel cell LSM/YSZ composite cathodes. *Journal of The Electrochemical Society*, 148(5):A433–A442, 2001.

[108] C. Huang, K. Huang, H. Wang, S. Liu, and Y. Zeng. The effect of solid

electrolyte interface formation conditions on the aging performance of Li-ion cells. *Journal of Solid State Electrochemistry*, 15(9):1987–1995, 2011.

[109] B. V. Ratnakumar, M. C. Smart, and S. Surampudi. Electrochemical impedance spectroscopy and its applications to lithium ion cells. In *Battery Conference on Applications and Advances, 2002. The Seventeenth Annual*, pages 273–277, 2002.

[110] R.T. DeHoff. Quantitative serial sectioning analysis: preview. *Journal of Microscopy*, 131(3):259–263, 1983.

[111] M.A. Groeber, B.K. Haley, M.D. Uchic, D.M. Dimiduk, and S. Ghosh. 3D reconstruction and characterization of polycrystalline microstructures using a FIB–SEM system. *Materials Characterization*, 57(4):259–273, 2006.

[112] Nan Yao. Focused ion beam systems. Cambridge University Press, 2007.

[113] A. Cecen, E.A. Wargo, A.C. Hanna, D.M. Turner, S.R. Kalidindi, and E.C. Kumbur. 3-D microstructure analysis of fuel cell materials: spatial distributions of tortuosity, void size and diffusivity. *Journal of The Electrochemical Society*, 159(3):B299–B307, 2012.

[114] S. Cooper, D.S. Eastwood, J. Gelb, G. Damblanc, D.J.L. Brett, R. Bradley, P.J. Withers, P.D. Lee, A.J. Marquis, and N.P. Brandon. Image based based modelling modelling of tortuosity in Li-ion battery electrodes: A study of microstructural heterogeneity in $LiFePO_4$ electrodes for Li-ion batteries. *Journal of Power Sources*, 247:1033–1039, 2013.

[115] B. J. Buck, A. L. Brock, W. H. Johnson, and A. L. Ulery. Corrosion of depleted uranium in an arid environment: Soil-geomorphology, SEM/EDS, XRD, and electron microprobe analyses. *Soil and Sediment Contamination: An International Journal*, 13(6):545–561, 2004.

[116] R. J. Hemley, H. Mao, G. Shen, J. Badro, P. Gillet, M. Hanfland, and D. Hausermann. X-ray imaging of stress and strain of diamond, iron, and tungsten at megabar pressures. *Science*, 276(5316):1242–1245, 1997.

[117] T. Nanba. X-ray diffraction study of microstructure of amorphous tungsten trioxide films prepared by electron beam vacuum evaporation. *Journal of Solid State Chemistry*, 83(2):304, 1989.

[118] Y. Waseda, K. Hirata, and M. Ohtani. High-temperature thermal expansion of platinum, tantalum, molybdenum, and tungsten measured by x-ray diffraction. *High Temp. - High Pressures*, 7(2):221–226, 1975.

[119] B. Yous, S. Robin, A. Donnadieu, G. Dufour, C. Maillot, H. Roulet, and C. Senemaud. Chemical vapor deposition of tungsten oxides: A comparative study by x-ray photoelectron spectroscopy, x-ray diffraction and reflection high energy electron diffraction. *Materials Research Bulletin*, 19(10):1349–1354, 1984.

[120] H. M. Rietveld. A profile refinement method for nuclear and magnetic structures. *Journal of Applied Crystallography*, 2(2):65–71, Jun 1969.

[121] H.E. Swanson, E. Tatge, and R.K. Fuyat. Standard x-ray diffraction powder patterns. *US Department of Commerce, National Bureau of Standards*, 1953.

[122] V.T. Deshpande and R. Pawar. X-ray determination of thermal expansion of tungsten. *CURRENT SCIENCE*, 31(12):497, 1962.

[123] B.L. Henke, E.M. Gullikson, and J.C. Davis. X-ray interactions: photoabsorption, scattering, transmission, and reflection at E=50-30000 eV, Z=1-92. *Atomic Data and Nuclear Data Tables*, 54:181–342, 1993.

[124] V.F. Sears. Neutron news. 3:29–37, 1992.

[125] R.E. White. *Electrochemical Cell Design.* Plenum Press, 1984.

[126] C.L Zeng, W Wang, and W.T Wu. Electrochemical impedance models for molten salt corrosion. *Corrosion Science*, 43(4):787 – 801, 2001.

[127] G. Gao, F.H. Stott, J.L. Dawson, and D.M. Farrell. Electrochemical monitoring of high-temperature molten-salt corrosion. *Oxidation of Metals*, 33(1-2): 79–94, 1990.

[128] A. B. Moradi, J. W. Hopmans, S. E. Oswald, M. Menon, A. Carminati, and E. Lehmann. Applications of neutron imaging in soil-water-root systems. In Stephen H. Anderson and Jan W. Hopmans, editors, *Soil-Water-Root Processes: Advances in Tomography and Imaging*, SSSA Special Publication, pages 113–136. The Soil Science Society of America, Inc., 2013.

[129] B. Kämpfe, F. Luczak, and B. Michel. Energy dispersive x-ray diffraction. *Particle & Particle Systems Characterization*, 22(6):391–396, 2005.

[130] R. Bhagat, M. Jackson, D. Inman, and R. Dashwood. Production of Ti-W alloys from mixed oxide precursors via the FFC Cambridge Process. *Journal of The Electrochemical Society*, 156(1):E1, 2009.

[131] R. Bhagat, M. Jackson, D. Inman, and R. Dashwood. The production of Ti-Mo alloys from mixed oxide precursors via the FFC Cambridge process. *Journal of The Electrochemical Society*, 155(6):E63–E69, 2008.

[132] B. K. Jackson. Characterization of the FFC Cambridge Process for NiTi production using in situ x-ray synchrotron diffraction. *Journal of The Electrochemical Society*, 157(4):E57, 2010.

[133] G. Qiu. Metallic cavity electrodes for investigation of powders. *Journal of the Electrochemical Society*, 152(10):E328, 2005.

[134] G. Z. Chen and D.J. Fray. A morphological study of the FFC chromium

and titanium powders. *Transactions - Institution of Mining and Metallurgy. Section C. Mineral processing & extractive metallurgy*, 115(1):49, 2006.

[135] J. Peng, G. Li, H. Chen, D. Wang, X. Jin, and G. Z. Chen. Cyclic voltammetry of ZrO_2 powder in the metallic cavity electrode in molten $CaCl_2$. *Journal of the Electrochemical Society*, 157(1):F1, 2010.

[136] G. Qiu, D. Wang, M. Ma, X. Jin, and G. Z. Chen. Electrolytic synthesis of $TbFe_2$ from Tb_4O_7 and Fe_2O_3 powders in molten $CaCl_2$. *Journal of Electroanalytical Chemistry*, 589(1):139–147, 2006.

[137] G. Qiu. Investigation on electrochemical reduction process of Nb_2O_5 powder in molten $CaCl_2$ with metallic cavity electrode. *Electrochimica Acta*, 53(12): 4074, 2008.

[138] K. Rao, D. Brett, D. Inman, and R.J. Dashwood. Investigation of the reduction electrochemistry of titanium oxides in molten calcium chloride using cavity electrode. *Titanium-2007*, 2007.

[139] H. A. Laitinen. Preparation of pure fused lithium chloride-potassium chloride eutectic solvent. *Journal of The Electrochemical Society*, 104(8):516, 1957.

[140] P.J. Masset. Thermogravimetric study of the dehydration reaction of $LiCl.H_20$. *Journal of Thermal Analysis and Calorimetry*, 96(2):439–441, 2009.

[141] P. Cortona. Direct determination of self-consistent total energies and and charge densities of solids: a study of the cohesive properties of the alkali halides. *Physical Review, Serie 3. B - Condensed*, 46, 1992.

[142] A.V. Larin, A.N. Kislov, A.E. Nikiforov, and S.E. Popov. The ab-initio calculation of crystal structure and lattice dynamics of perfect and defective MeX (Me^+ = Rb^+, K^+, Na^+; X^-= F^-, Cl^-). *Journal of Physics: Conference Series 92*, 2007.

[143] E. Eriksurd and E. Heitz. Reference electrodes. In *Guidelines on Electrochemical Corrosion Measurements: (EFC 4)*. Maney Publishing, 1990.

[144] G.J. Janz and A. Conte. Potentiostatic polarization studies in fused carbonates-i. the noble metals, silver and nickel. *Electrochimica Acta*, 9(10): 1269 – 1278, 1964.

[145] M.D. Ingram, B. Baron, and G.J. Janz. The electrolytic deposition of carbon from fused carbonates. *Electrochimica Acta*, 11(11):1629 – 1639, 1966.

[146] P.K. Lorenz and G.J. Janz. Electrolysis of molten carbonates: anodic and cathodic gas-evolving reactions. *Electrochimica Acta*, 15(6):1025 – 1035, 1970.

[147] H.E. Bartlett and K.E. Johnson. Electrochemical studies in molten Li_2 CO_3-Na_2 CO_3. *Journal of The Electrochemical Society*, 114(5):457–461, 1967.

[148] P.K. Lorenz and G.J. Janz. The carbon monoxide, carbon dioxide and carbon monoxide electrodes in molten alkali carbonates. *Journal of The Electrochemical Society*, 116(8):1061–1065, 1969.

[149] J. Bockris, G. J. Bockris, D. Hills, L. Inman, and Young. An all-glass reference electrode for molten salt systems. *Journal of Scientific Instruments (1950)*, 33(11):438–439, 1956.

[150] A. Eichler. Tetragonal Y-doped zirconia: Structure and ion conductivity. *Phys. Rev. B*, 64:174103, Oct 2001.

[151] J. B. Goodenough and Y.i Huang. Alternative anode materials for solid oxide fuel cells. *Journal of Power Sources*, 173(1):1 – 10, 2007.

[152] R. Pornprasertsuk, P. Ramanarayanan, C. B. Musgrave, and F. B. Prinz. Predicting ionic conductivity of solid oxide fuel cell electrolyte from first principles. *Journal of Applied Physics*, 98(10):103513, 2005.

[153] V. Danek. *Physico-chemical analysis of molten electrolytes.* Elsevier, 2006.

[154] G. J. Janz. Physical properties and structure of molten salts. *Journal of Chemical Education*, 39(2):59, 1962.

[155] M. Shimoji. Interaction in molten salt mixtures. *Discuss. Faraday Soc.*, 32: 128–137, 1961.

[156] V.P. Glushko. Thermocenter of the russian academy of sciences. *IVTAN Association, Izhorskaya*, 13(19):127412, 1994.

[157] H. Landolt and R. Börnstein. *Thermodynamic Properties of Inorganic Materials.* Springer, 1999.

[158] D.G. Archer. Thermodynamic properties of the KCl+ H_2O system. *Journal of Physical and Chemical Reference Data*, 28(1):1–17, 1999.

[159] I. Barin, F. Sauert, E. Schultze-Rhonhof, and W.S. Sheng. *Thermochemical data of pure substances*, volume 6940. VCH Weinheim, 1993.

[160] M.W. Chase Jr., C.A. Davies, J.R. Downey Jr., D.J. Frurip, R.A. McDonald, and A.N. Syverud. Tables, janaf thermochemical. *J. Phys. Chem. Ref. Data*, 14(Suppl 1), 1985.

[161] I. Barin. *Thermodynamical Data of Pure Substances.* (VCH Verlags Gesellschaft), Weinheim, 1977.

[162] I. Barin. *Thermodynamical Data of Pure Substances.* VCH Verlags Gesellschaft, Weinheim, 1989.

[163] I. Barin. *Thermodynamical Data of Pure Substances.* VCH Verlags Gesellschaft, Weinheim, 1995.

[164] M. Binnewies and E. Milke. *Thermochemical data of elements and compounds.* Wiley-VCH, 2002.

[165] M.W. Chase. *NIST-JANAF thermochemical tables*. New York, 1998.

[166] O. Knacke, O. Kubaschewski, and K. Hesselmann. Thermodynamic properties of inorganic substances. *Springer Verlag, DÃŒsseldorf, Germany*, page 1, 1991.

[167] Landolt-Bornstein. *Thermodynamic Properties of Inorganic Materials*. Springer-Verlag, Berlin-Heidelberg, 2000.

[168] Landolt-Bornstein. *Thermodynamic Properties of Inorganic Materials*. Springer-Verlag, Berlin-Heidelberg, 2001.

[169] J. Hur, S. Seo, C.and Hong, D. Kang, and S. Park. Metallization of U_3O_8 via catalytic electrochemical reduction with Li_2O in LiCl molten salt. *Reaction Kinetics and Catalysis Letters*, 80(2):217–222, 2003.

[170] D. Hall, A.D. Rae, and T.N. Waters. The crystal structure of bisnitratodiaquodioxo-uranium (VI) tetrahydrate (uranyl nitrate hexahydrate). *Acta Crystallographica*, 19(3):389–395, 1965.

[171] J.R. Bridge, C.W. Melton, C.M. Schwartz, and D.A. Vaughan. *THERMAL DECOMPOSITION OF URANYL NITRATE HEXAHYDRATE*. 1956.

[172] S. Dash, M. Kamruddin, Santanu Bera, P.K. Ajikumar, A.K. Tyagi, S.V. Narasimhan, and Baldev Raj. Temperature programmed decomposition of uranyl nitrate hexahydrate. *Journal of Nuclear Materials*, 264(3):271–282, 1999.

[173] P.A Haas. A comparison of processes for the conversion of uranyl nitrate into ceramic-grade UO_2. *Nuclear Technology*, 81(3):393–406, 1988.

[174] S. Hartland and R.J. Nesbitt. Thermal decomposition of uranyl nitrate hexahydrate. *Journal of Applied Chemistry*, 14(9):406–412, 1964.

[175] W. Lodding and L. Ojamaa. Dehydration and thermal decomposition of uranyl nitrates in the presence of steam. *Journal of Inorganic and Nuclear Chemistry*, 27(6):1261 – 1268, 1965.

[176] R. S. Ondrejcin and T. P. Garrett. The thermal decomposition of anhydrous uranyl nitrate and uranyl nitrate dihydrate. *The Journal of Physical Chemistry*, 65(3):470–473, 1961. doi: 10.1021/j100821a020.

[177] K. V. Rajagopalan, P. V. Rajagopalan, T. P. Ravindran, and Radhakrishnan. Thermal decomposition of uranyl nitrate hexahydrate. *Journal of thermal analysis*, 44(1):89–96, 1995.

[178] W. H. Smith. Thermal dehydration of uranyl nitrate hydrates. *Journal of Inorganic and Nuclear Chemistry*, 30(7):1761 – 1768, 1968.

[179] R. De Forcrand. *Annuli Di Chimica*, 34(3), 1915.

[180] S. Siegel and H.R. Hoekstra. Bond lengths in gamma-uranium trioxide. *Inorganic and Nuclear Chemistry Letters*, 7(5):455–459, 1971.

[181] W. Lodding and L. Ojamaa. Dehydration and thermal decomposition of uranyl nitrates in the presence of steam. *Journal of Inorganic and Nuclear Chemistry*, 27(6):1261–1268, 1965.

[182] A.H. Le Page and A.G. Fane. The kinetics of hydrogen reduction of UO_3 and U_3O_8 derived from ammonium diuranate. *Journal of Inorganic and Nuclear Chemistry*, 36(1):87–92, 1974.

[183] S.A. Barrett, A.J. Jacobson, B.C. Tofield, and B.E.F. Fender. The preparation and structure of barium uranium oxide $BaUO_3$+ x. *Acta Crystallographica Section B: Structural Crystallography and Crystal Chemistry*, 38(11):2775–2781, 1982.

[184] L. Desgranges, G. Baldinozzi, G. Rousseau, J. Niepce, and G. Calvarin. Neutron diffraction study of the in situ oxidation of UO_2. *Inorganic chemistry*, 48 (16):7585–7592, 2009.

[185] D. S. Fox and N.S. Jacobson. Molten-salt corrosion of silicon nitride: I, sodium carbonate. *Journal of the American Ceramic Society*, 71(2):128–138, 1988.

[186] G.B. Dunks and D. Stelman. Electrochemical studies of molten sodium carbonate. *Inorganic Chemistry*, 22(15):2168–2177, 1983.

[187] L.D. Brown, R. Abdulaziz, S. Simons, D. Inman, D.J.L. Brett, and P.R. Shearing. Predominance diagrams of uranium and plutonum species in both lithium chloride–potassium chloride eutectic and calcium chloride. *Journal of Applied Electrochemistry*, 43(12):1235–1241, 2013.

[188] C.W. Tucker. The crystal structure of the phase of uranium. *Acta Crystallographica*, 4(5):425–431, 1951.

[189] DG Martin. The thermal expansion of solid UO_2 and (U, Pu) mixed oxides – a review and recommendations. *Journal of Nuclear Materials*, 152(2):94–101, 1988.

[190] R.W. Benedict, C. Solbrig, B. Westphal, T.A. Johnson, S.X. Li, K. Marsden, and K.M. Goff. Pyroprocessing progress at Idaho national Laboratory. *Advanced Nuclear Fuel Cycles and Systems (GLOBAL 2007)*, 2007.

[191] BTM Willis. Neutron diffraction studies of the actinide oxides. i. uranium dioxide and thorium dioxide at room temperature. *Proceedings of the Royal Society of London. Series A. Mathematical and Physical Sciences*, 274(1356): 122–133, 1963.

[192] BTM Willis. Neutron diffraction studies of the actinide oxides. ii. thermal motions of the atoms in uranium dioxide and thorium dioxide between room

temperature and 1100°C. *Proceedings of the Royal Society of London. Series A. Mathematical and Physical Sciences*, 274(1356):134–144, 1963.

[193] NA Curry. An investigation of the magnetic structure of uranium nitride by neutron diffraction. *Proceedings of the Physical Society*, 86(6):1193, 1965.

[194] E. R. Jette and F. Foote. Precision determination of lattice constants. *The Journal of Chemical Physics*, 3(10):605–616, 1935.

[195] R. J. Ross. *Microelectronics Failure Analysis Desk Reference (6th Edition)*. ASM International, 2011.

[196] K.M. Goff, R.W. Benedict, K.L. Howden, G.M. Teske, and T.A. Johnson. Pyrochemical treatment of spent nuclear fuel. In *Proceedings of GLOBAL*, 2005.

[197] S.X. Li, S.D. Herrmann, K.M. Goff, M.F. Simpson, and R.W. Benedict. Actinide recovery experiments with bench-scale liquid cadmium cathode in real fission product-laden molten salt. *Nuclear technology*, 165(2):190–199, 2009.